Quantum measurement protocols for many-qubit states

Inaugural-Dissertation

zur Erlangung des Doktorgrades
der Mathematisch-Naturwissenschaftlichen Fakultät
der Heinrich-Heine-Universität Düsseldorf

vorgelegt von

Samuel Morales
aus Mainz

Düsseldorf, April 2025

aus dem Institut für Theoretische Physik, Lehrstuhl IV
der Heinrich-Heine Universität Düsseldorf

Gedruckt mit der Genehmigung der
Mathematisch-Naturwissenschaftlichen Fakultät der
Heinrich-Heine Universität Düsseldorf

Berichterstatter:

1. Prof. Dr. Reinhold Egger

2. PD Dr. Hermann Kampermann

3. Prof. Dr. Johann Kroha

Tag der mündlichen Prüfung: 16. Oktober 2025

Abstract

Recent advances in the development of highly controllable quantum systems in the form of noisy-intermediate scale quantum devices have opened the path for new descriptions of quantum dynamics. One major task in the operation of such systems is the preparation of (entangled) states in a controlled fashion.

This work addresses this research question by using measurement-induced back-action together with unitary dynamics. In these measurement-steering protocols, the system of interest is repeatedly coupled to a reinitialized detector, whose projective measurement steers the system towards the pre-chosen target state. How to harness these measurement outcomes for active decision making, promising a speedup and higher final state fidelity over passive protocols, is a highly non-trivial question.

In this thesis, a new cost function-based steering scheme is introduced, where Bell detector measurements induce entanglement in the system without a direct coupling of system qubits. By including local terms into the cost function, many-body entangled states can be prepared, going beyond previously established bounds for blind steering protocols, where the measurement outcomes are discarded. The classical calculation of the cost function before each coupling time step allows for guided decision making for a suitable coupling between system and detector.

When introducing environmentally induced errors into the system, a threshold transition appears, showing successful state preparation for weak coupling to the environment. For stronger errors, the final state is dominated by the environmentally induced dynamics, closing the purity gap of the system state at the threshold between both regimes.

Additionally, in order to overcome previous scalability issues, the cost function can be modified, such that using the Quantum Fisher Information as a cost function allows targeting genuinely entangled states in many-qubit systems.

These results constitute significant advancements in the area of active measurement-steering protocols and offer new routes for future improvements in this field of research. In particular, the experimental implementation of these protocols will pose an interesting and demanding challenge in the future.

Zusammenfassung

Jüngste Fortschritte in der Entwicklung hoch-präziser Quantensysteme, insbesondere in der Form von *Noisy Intermediate-scale Quantum* Geräten, haben neuen Beschreibungen der zugrundeliegenden Quantendynamiken den Weg eröffnet. Ein Hauptaugenmerk im Betrieb solcher liegt hierbei in der kontrollierten Präparierung (verschränkter) Zustände.

Diese Arbeit untersucht diese Aufgabe durch Ausnutzen messinduzierter Rückkopplung im Zusammenspiel mit unitärer Dynamik. In solchen Messsteuerungsprotokollen wird das Zielsystem wiederholt an einen stets reinitialisierten Detektor gekoppelt, dessen projektive Messung das System in Richtung des vorgewählten Zielzustandes lenkt. Wie hierbei die entsprechenden Messergebnisse für eine aktive Entscheidungsfindung genutzt werden können, um eine Beschleunigung und höhere Fidelität gegenüber passiven Protokollen zu erreichen, ist eine höchst nicht-triviale Forschungsfrage.

In dieser Dissertation wird ein neues Kostenfunktion-basiertes Protokoll eingeführt, welches sogenannte Bell Detektormessungen zur Verschränkungserzeugung im System ausnutzt und somit eine direkte Kopplung der System-Qubits vermeidet. Durch die Hinzunahme von lokalen Kostenfunktionstermen, ist es hierbei möglich, Vielteilchenzustände zu präparieren, welche nicht durch sogenannte blinde Protokolle, in welchen die Messergebnisse nicht ausgelesen werden, erreichbar sind. Die klassische Berechnung der Kostenfunktion vor jedem Kopplungsschritt erlaubt eine zielgerichtete Entscheidungsfindung der geeigneten Kopplung zwischen System und Detektor.

Das Einführen von Fehlern, welche durch die Umgebung induziert werden, führt zu einer Übergangsschwelle, bei der die Zustandspräparierung für schwache Kopplung an die Umgebung erfolgreich bleibt. Bei starker Fehlerrate ist der Endzustand jedoch durch die von der Umgebung induzierte Dynamik dominiert, begleitet von einer Schließung der Reinheitslücke des Zustandes an der Schwelle zwischen beiden Regimen.

Zusätzlich kann die Kostenfunktion modifiziert werden, um vorherige Skalierungsprobleme zu überwinden, sodass die Benutzung der Quanten-Fisher-Information als Kostenfunktion die Präparierung von generisch verschränkten Zuständen in Mehr-Qubit Systemen erlaubt.

Diese Ergebnisse stellen einen signifikanten Fortschritt im Gebiet der aktiven Messsteuerungsprotokolle dar und ebnen den Weg für zukünftige Fortschritte in diesem Forschungsfeld. Insbesondere die experimentelle Implementierung dieser Protokolle wird in Zukunft eine interessante und signifikante Herausforderung darstellen.

Contents

Chapter 1

Introduction

With the advent of highly controllable quantum devices in the form of *noisy intermediate-scale quantum devices* (NISQ), the demand for theoretical descriptions of the evolution of such systems has steadily increased in recent years. The interplay of unitary dynamics, measurements and the coupling to an environment can lead to a plethora of different effects and phenomena, like measurement-induced phase transitions [1–5].

These devices are suited to perform first algorithms, often using classical computations to determine a suitable quantum circuit. Notable candidates are so-called variational quantum algorithms (VQA) like the quantum approximate optimization algorithm or the variational quantum eigensolver, where the optimization of a parametrized unitary circuit targets the ground state of a problem Hamiltonian [6].

Beyond computational tasks, one line of research is interested in the general preparation of specific states, in particular highly entangled non-local many-body states. These states can be used for various applications, e.g., as resource states for measurement-based quantum computers or quantum metrology [7]. Also, quantum error correction (QEC), where a logical qubit is encoded by using multiple physical qubits, needs state initialization, which can be done by measuring the corresponding stabilizers [8]. Notably, QEC below the surface code threshold has been recently reported, leading to an error suppression when scaling to bigger code distances [9].

There are different approaches for the preparation of such states beyond projective measurements. Cooling protocols have been formulated to prepare low-energy states of arbitrary Hamiltonians [10]. Also, drive-and-dissipation protocols have been proposed, where the coupling of the system to the environment and an applied drive are harnessed to reach the target state [11, 12]. Most approaches are, however, often limited to small system sizes due to their scaling properties or are only suitable for the preparation of a restricted set of states [13, 14].

In this thesis, we will dive into the topic of target state preparation using (weak) measurements. Here, this goal is reached by an interplay of proper unitary dynamics and the measurement of parts of the system denoted as detector. This detector can correspond to a certain region of a quantum chip, which is measured, similar to QEC codes [9], or to a different qubit platform that

is coupled to the qubits used for computations. In particular, different types of qubits offer diverse advantages in terms of measurement times and fidelity [15–17], making hybrid devices possibly advantageous for an experimental implementation. Dissipation and decoherence due to the environment are treated as detrimental to the steering process as opposed to drive-and-dissipation protocols.

Recently, a general protocol for the preparation of many-body states using the back-action created by partly measuring entangled systems has been proposed [14]. This approach promises less fine-tuning and better scalability with increasing system size by only using local couplings. In a first version of such protocols, an average over measurement outcomes *steers* the state towards a pre-chosen target by using suitable couplings between system and detector. Going beyond these *blind* measurements where the measurement outcome is effectively discarded, another work proposed different routes to improve existing blind steering protocols by including the measurement outcome into an active decision making process [18]. One route is based on so-called quantum state machines, mapping out the Hilbert space to a graph, such that the target state preparation corresponds to finding a proper path in Hilbert space [18].

A different approach uses cost functions to encode the distance to the target, and the state preparation is achieved by a proper minimization procedure. This is reminiscent of some VQAs, and also (quantum) machine learning techniques, where a proper function is minimized as part of the learning procedure [19]. Similar policies have also been proposed for Quantum control theory [20].

This work presents recent results obtained for measurement-steered systems. Chapter 2 will summarize the general tools of quantum master equations and stochastic equations used throughout this thesis to describe open quantum systems subject to measurements. The description of the environment is restricted to the Lindblad theory. A simple example system is presented, where stochastic equations arise naturally when describing the projective measurement of a detector qubit, coupled to a system qubit [21]. Moreover, as preparation for the protocols presented in this work, the quantum phenomenon of entanglement swapping is presented, where measurements are used to induce entanglement in spatially separated systems. Additionally, weak values are introduced as another example of effects appearing in weakly measured systems.

As further background, the aforementioned measurement steering procedure is summarized in Chapter 3. The basic protocol is presented, starting with *blind* and *passive* steering, where the measurement outcomes are not used during the protocol. As an extension, previous results for *active* steering protocols are summarized, focusing on the peculiarities which come with reading out the measurement outcomes and the corresponding decision making during the protocol. Simple examples are given, highlighting the differences between possible ways of navigating towards the target state in the system Hilbert space. A focus is set on where the limitations of these results lie, motivating the definition of new protocols.

Next, in Chapter 4 we will present the results of Ref. [22] as the main part of this work. Here, a new type of active steering protocol based on a *local* cost function is presented. In contrast to

previous results, highly entangled states of multiple qubits are prepared using only local couplings. This is possible by actively reading out the detector measurements in order to track the system state. This overcomes a known no-go theorem for the blind preparation of maximally entangled target states, which also applies to drive-and-dissipation protocols when only employing local couplings [13]. This work introduces so-called *weak* entanglement swapping, where entanglement is induced in the system by suitable detector measurements, going beyond previous measurement steering protocols. By using a *local* cost function, encoding all locally reduced states inside the system, a directed decision is made to *steer* the system towards the chosen target state. Measurement outcomes are used to keep track of the system, which is necessary for the process of decision making. Numerical results for $N \leq 6$ qubits are presented, showing a proof of principle for such measurement protocols.

Building on this protocol, Chapter 5 reports an appearing threshold transition when introducing environmentally induced errors into the system. The results of Ref. [23] are summarized, where environmentally induced amplitude damping and dephasing spoil the system state. The active steering protocol is able to tolerate certain levels of noise, showing similarities to the known phase transition present in QEC systems [8].

The following Chapter 6 is devoted to a modification of the protocol presented before, by replacing the cost function with the Quantum Fisher Information. After an introduction to the concept of the Quantum Fisher Information known from metrology, Ref. [24] is reproduced. The modified cost function allows for a scalable protocol with numerical results up to $N = 22$ qubits, overcoming previous scalability limitations. In this case, the single target state is replaced by a manifold of states, maximizing the Quantum Fisher Information.

Lastly, a summary of the main results of this work is given, along with an outlook on the next steps for possible future extensions in this field of research. The appendix shows additional calculations and results, useful in understanding the full details of the protocols presented in the main text, as well as extensions and new results.

Chapter 2

Open monitored quantum systems

This chapter introduces the analytical tools and basic equations that we will use to describe open monitored quantum systems. To this end, we first introduce the Lindblad equation used to describe Markovian systems weakly coupled to an environment. Next, monitoring is added by discussing measurements on parts of the quantum system, denoted as the detector. These measurements can be described by the Kraus representation and in the weak-coupling or short-time limit by stochastic equations.

The units are chosen such that Planck's constant $\hbar$ is set to 1 throughout.

2.1 Open quantum systems

When quantum mechanics is introduced, one usually only thinks in terms of closed quantum systems in which information is preserved. These systems are described by unitary time evolution, namely the Schrödinger equation for the wave function $|\Psi\rangle$ [25] or the von Neumann equation of motion (EOM) when generalizing to mixed states ρ [25–27]. The latter is given by

$$\frac{\mathrm{d}}{\mathrm{d}t}\rho(t) = -i[H(t), \rho(t)], \tag{2.1}$$

where H is the generally time-dependent Hamiltonian describing the system at hand and $[A, B] = AB - BA$ denotes the commutator.

A more realistic description of quantum systems, however, needs to go beyond the scope of closed systems by introducing an environment[1] coupled to the system of interest, see Fig. 2.1 for a schematic. The environment is usually assumed to be much larger than the system of interest, with many more degrees of freedom.

The combination of system and environment is now described by the tensor product space $\mathcal{H}_{s\text{-}e} = \mathcal{H}_s \otimes \mathcal{H}_e$ and is assumed to be closed, i.e., the time evolution of the total density matrix ρ_{se} is of course again given by the von Neumann equation (2.1). It can be solved by using

[1]The environment is also sometimes referred to as reservoir for an infinite number of degrees of freedom or as (heat) bath for a reservoir in thermal equilibrium [25].

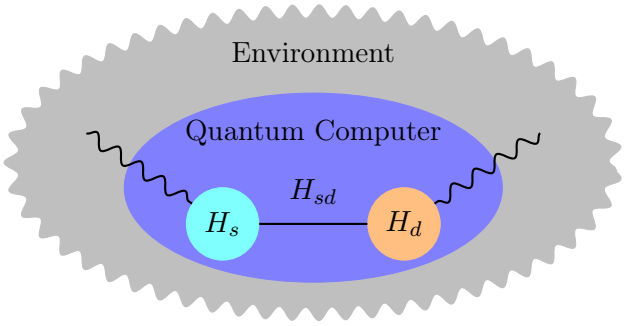

Figure 2.1: Schematic picture of an open quantum system consisting of a quantum computer and its environment e. The quantum computer is split into a relevant system s and a measured detector d as in the subsequent sections. The environment can induce dissipation in system and detector.

the time evolution operator $U(t)$, which for a time-independent Hamiltonian H takes the form $U(t) = e^{-itH}$ [25].

The total Hamiltonian of the composite system can be written as

$$H = H_s + H_e + H_{se}, \tag{2.2}$$

where H_s and H_e are the system- and environment-only Hamiltonians and H_{se} encodes the interaction. We omitted the unit matrix and tensor products for clarity and will do so throughout.

In Fig. 2.1, the system is further split into a *system* and *detector*, so that $H_s \to H_s + H_d + H_{sd}$, which will be of interest when discussing measurements in the next section but is ignored for now.

The following results are usually derived in the interaction picture with respect to the free Hamiltonian $H_0 = H_s + H_e$, however, we will stick to the Schrödinger picture. See Ref. [25] and [26] for a more detailed discussion.

Now, to recover the system density matrix, a partial trace over the environmental degrees of freedom has to be performed, so that $\rho_s = \mathrm{Tr}_e(\rho_{se})$. Our goal is to obtain an EOM describing the evolution of ρ_s, called *master equation* [26].

For this purpose, we use the so-called Born approximation, where the environment is only weakly affected by the system, corresponding to the weak-coupling limit. Then, the total density matrix can be approximated by $\rho(t) \approx \rho_s(t) \otimes \rho_e(0)$ [25, 26]. Secondly, we assume that the system couples to many environmental degrees of freedom at the same time, motivating the definition of a local-in-time EOM which does not depend on the initial configuration [25]. It holds when the environmental correlation functions decay much faster than any time scale of the system dynamics, therefore neglecting memory effects. Because these short time scales are not resolved, this EOM describes the evolution on a coarse-grained time axis [25]. This is the so-called Markov approximation; for a more detailed derivation, see Ref. [25]. In addition to these approximations, one has to apply the rotating wave approximation by averaging over fast oscillating terms in the EOM [25].

This leads to the time evolution being described by a completely positive[2] and trace-preserving (CPTP) map, where the time evolution of ρ_s is described by the generator $\mathcal{L}$ of a quantum dynamical semigroup, called Lindbladian, such that [25]

$$\frac{\mathrm{d}}{\mathrm{d}t}\rho_s = \mathcal{L}\rho_s = -i[H_L, \rho_s] + \sum_i \Gamma_i \left(c_i \rho_s c_i^\dagger - \frac{1}{2}\{c_i^\dagger c_i, \rho_s\} \right) \tag{2.3a}$$

$$= -i[H_L, \rho_s] + \sum_i \Gamma_i \mathcal{D}[c_i]\rho_s. \tag{2.3b}$$

Here, we introduced the Lindblad dissipator $\mathcal{D}[c]$ defined by an operator c and acting on a density matrix according to $\mathcal{D}[c]\rho = c\rho c^\dagger - \frac{1}{2}\{c^\dagger c, \rho\}$ where $\{A, B\} = AB + BA$ is the anticommutator. The relaxation rates Γ_i are non-negative and depend on environmental correlation functions, see Ref. [25] for a full derivation. The (Lindblad) jump operators c_i therefore describe the effect of the environment on the system through emission and absorption processes, leading to the dissipation dynamics of the system [27]. The appearing Hamiltonian term H_L usually contains the Lamb shift Hamiltonian, which we will not further discuss in the following, see Ref. [25] for more details. In the Schrödinger picture, also the system Hamiltonian H_s appears as part of H_L [25].

Eq. (2.3) is the most general form for a generator of a CPTP quantum dynamical semigroup after proper diagonalization [25–27]. In particular, the dynamical map of this semigroup that is represented by its generator $\mathcal{L}$ can be written in exponential form. The time evolution of the density matrix is therefore given by [25, 26, 28]

$$\rho_s(t) = \mathrm{e}^{\mathcal{L}t}(\rho_s(0)) \tag{2.4}$$

using the exponential of the superoperator $\mathcal{L}$.

As with the Hamiltonian being the generator of unitary dynamics, the eigenvalue spectrum of $\mathcal{L}$ can be examined. The spectrum lies in the non-positive part of the real axis on the complex plane, since the dynamics in general describe dissipation. It can give us information about the steady states corresponding to an eigenstate to the eigenvalue 0 at infinite time and how they are approached. States corresponding to negative real eigenvalues are associated with an (exponentially) decaying trajectory. Complex eigenvalues with non-positive real part come in complex conjugate pairs, where imaginary eigenvalues correspond to oscillating coherences, describing phases between multiple steady states [28]. These are induced by the Hamiltonian part of the Lindbladian in Eq. (2.3) and can always be eliminated by going to the rotating frame [28]. Correspondingly, complex eigenvalues with negative real part are said to define spiraling dynamics [28].

The maximal convergence time needed to reach a steady state is then given by the smallest absolute value of the real part of the eigenvalues of $\mathcal{L}$ [14, 28]. If multiple steady states are

[2]Meaning that the positivity of the densitiy matrix (even when the Lindbladian only acts on an entangled subsystem) is preserved, see Ref. [26].

present, they can form a steady state subspace [28], also called dark space, which can be used to define a protected qubit in state preparation protocols by drive-and-dissipation [11, 12]. When demanding locality of the corresponding Lindblad operators c_i, restrictions are placed on the structure of the possible steady states. In particular, some entangled states cannot be reached by local couplings, including the GHZ and the W state [13], see Chapter 4 for a further discussion.

Here, we will only consider Lindbladian dynamics as stemming from an error-inducing environment and therefore being detrimental for our state preparation protocols. The precise form of such errors depends on the considered system, however, we will restrict ourselves to single-qubit errors. Namely, we consider *amplitude damping* corresponding to a Lindblad operator $c_{\mathrm{AD}} = \sigma^-$ [29] where $\sigma^{\pm} = \frac{1}{2}(\sigma^x \pm i\sigma^y) = \sigma^{\mp\dagger}$ are the Pauli jump operators, see below. It describes the dissipation of energy in the system, e.g., by the emission of a photon [29]. We will also discuss dephasing errors (alternatively called phase flip or phase damping) with $c_{\mathrm{PD}} = \sigma^z$, giving a loss of quantum information without losing energy [29].

Such CPTP maps can also be written using the Kraus representation, more evident when talking about generalized measurements, as will be seen in the next section.

2.2 Measurements

2.2.1 POVMs and the Kraus representation

Again, when first introducing measurements in quantum mechanics, one usually thinks in terms of projective measurements, where a Hermitian operator is measured, with its eigenvalues i as possible measurement outcomes and the state being projected onto the corresponding eigenstate $|\Psi(i)\rangle$ after the measurement. The projective measurement is performed by applying projection operators $\mathcal{P}_i = |\Psi(i)\rangle\langle\Psi(i)|$ [3], so that for a measurement outcome i the state after the measurement is given by [21, 26, 29]

$$|\Psi(i)\rangle = \frac{\mathcal{P}_i|\Psi\rangle}{\sqrt{P_i}}, \quad \rho(i) = \frac{\mathcal{P}_i\rho\mathcal{P}_i}{P_i}, \tag{2.5}$$

for pure and mixed states respectively. The measurement probabilities are defined as $P_i = \mathrm{tr}(\rho\mathcal{P}_i) = \langle\Psi|\mathcal{P}_i|\Psi\rangle = \langle\mathcal{P}_i\rangle$ and the pure state is as usual only defined up to a global phase factor.[4]

This notion of measurement can, however, be generalized by introducing so-called positive operator valued measure (POVM) measurements where the projection operator $\mathcal{P}_i = \mathcal{P}_i^\dagger = \mathcal{P}_i^2$ is replaced by a non-Hermitian *Kraus operator* A_i. The states after this generalized measurement are then given by [21, 29]

$$|\Psi(i)\rangle = \frac{A_i|\Psi\rangle}{\sqrt{P_i}}, \quad \rho(i) = \frac{A_i\rho A_i^\dagger}{P_i}, \quad P_i = \mathrm{Tr}(\rho A_i^\dagger A_i), \tag{2.6}$$

where the corresponding measurement probabilities P_i need to obey $\sum_i P_i = 1$, implying the

[3] For simplicity, we restrict ourselves here to non-degenerate eigenspaces.

[4] Here and in the following we often drop the explicit time-dependence of the states for ease of notation.

completeness relation $\sum_i A_i^\dagger A_i = \mathbb{1}$ [5].

Interestingly, however, this *generalization* of measurements can again be understood as a projective measurement by adding additional degrees of freedom to our system and performing a projection only on this added part of the system which we denote as detector, see also Fig. 2.1 [21, 29]. We consider the state of our global system consisting of system s and detector d to be ρ_{sd} [6]. If the detector is measured projectively in the basis $\{|\Phi(i)\rangle_d\}$, the remaining system state after the measurement with outcome i is given by

$$\rho_s(i) = \frac{{}_d\langle\Phi(i)|\rho_{sd}|\Phi(i)\rangle_d}{P_i}, \tag{2.7}$$

where the probability to obtain measurement outcome i is given by $P_i = \mathrm{Tr}_s\left({}_d\langle\Phi(i)|\rho_{sd}|\Phi(i)\rangle_d\right)$, renormalizing the system state.

The connection to the POVM above becomes clearer if we assume that the detector has been initialized at time t in a state ρ_d, decoupled from the system state ρ_s. Now, both system and detector should be coupled by some time-independent Hamiltonian H_{sd} during a time-step of length δt, creating entanglement between system and detector. The combined state after the unitary time evolution is given as

$$\rho_{sd}(t+\delta t) = e^{-i\delta t H_{sd}}\rho_s(t)\rho_d e^{i\delta t H_{sd}}. \tag{2.8}$$

After the coupling time, the detector measurement is performed so that the detector gets effectively decoupled from the system. Assuming that the detector was prepared in a pure state $|\Phi_0\rangle_d$ before the time evolution, the Kraus operators defined above are given by

$$A_i = {}_d\langle\Phi(i)|e^{-i\delta t H_{sd}}|\Phi_0\rangle_d, \tag{2.9}$$

defining the measurement evolution of the system according to Eq. (2.6).

In this case, the evolution depends on the measurement outcome i. However, if we consider the limit of averaging over different measurement outcomes, effectively *discarding* them, the evolution of the system is described by a trace over all detector degrees of freedom. In the Kraus representation, we obtain

$$\langle\rho_s(t+\delta t)\rangle_{\mathrm{ms}} = \sum_i P_i\rho_s(i) = \sum_i A_i\rho_s(t)A_i^\dagger \tag{2.10}$$

with the usual probabilities $P_i = \mathrm{Tr}_s\left(A_i\rho_s A_i^\dagger\right)$. This average over measurement outcomes is denoted by $\langle\ldots\rangle_{\mathrm{ms}}$.

We see that Eq. (2.10) is trace-preserving due to the normalization of the measurement

[5] Again, we restrict ourselves to the case where each measurement outcome is associated with a single operator A_i. In general, POVMs $\{\Pi_i \geq 0\}$ can go beyond this simplification [21, 29].

[6] We now discard the environment e.

probabilities. We note that different measurement bases $|\Phi(i)\rangle$ give different representations of the Kraus operators but an equivalent average evolution since the trace is independent of the detector basis choice. In this way, we obtain the Kraus representation of a CPTP map, which in the weak-coupling limit is again described by a Lindblad equation as discussed in the previous section. Generally, measurements in the weak limit are also denoted as *weak measurements*.

2.2.2 Stochastic Schrödinger Equation

Now, we want to again look at the evolution when the measurement outcomes are kept track of, as in Eq. (2.6). In the weak measurement limit, a new tool for the description arises in the form of stochastic equations. Originally formulated in the quantum optics community [30, 31], we will see that such stochastic equations arise naturally when considering measurements in continuously monitored systems. We will show a simple derivation following Ref. [21], where two limits allow the simple definition of different types of stochastic equations. For a discussion of general detector measurements beyond these two examples, see Appendix A.

We consider the case where the detector d is comprised of a single qubit with the remaining system s being arbitrary. We can therefore write the coupling Hamiltonian as

$$\begin{aligned} H_{sd} =& \begin{pmatrix} H_s^{(0,0)} & H_s^{(0,1)} \\ H_s^{(1,0)} & H_s^{(1,1)} \end{pmatrix} \\ =& \frac{1}{2}\left(H_s^{(0,0)} + H_s^{(1,1)}\right)\tau^0 + \frac{1}{2}\left(H_s^{(0,0)} - H_s^{(1,1)}\right)\tau^z \\ &+ \frac{1}{2}\left(H_s^{(0,1)} + H_s^{(1,0)}\right)\tau^x + \frac{i}{2}\left(H_s^{(0,1)} - H_s^{(1,0)}\right)\tau^y, \end{aligned} \tag{2.11}$$

where the detector qubit Hilbert space is described by the Pauli matrices $\tau^\beta, \beta = 0, x, y, z$, defined as

$$\tau^x = \begin{pmatrix} 0 & 1 \\ 1 & 0 \end{pmatrix}, \quad \tau^y = \begin{pmatrix} 0 & -i \\ i & 0 \end{pmatrix}, \quad \tau^z = \begin{pmatrix} 1 & 0 \\ 0 & -1 \end{pmatrix}, \tag{2.12}$$

with $\tau^0 = \mathbb{1}_2$. We use both σ and τ for the Pauli matrices depending on whether they act in the system or detector Hilbert space.

The matrix elements are given by $H_s^{(\xi,\xi')} = {}_d\langle\xi|H_{sd}|\xi'\rangle_d$ for $\xi, \xi' = 0, 1$, with the qubit states $|0\rangle_d$ and $|1\rangle_d$ being the eigenstates of τ^z to the eigenvalues $+1$ and -1, respectively.

We now want to describe the evolution of the system during one time step, where the detector is initialized in a specific pure state and measured in a certain basis. W.l.o.g., we assume that the detector is always initialized in the state $|0\rangle_d$.

In the weak-measurement limit, where $\delta t\|H_{sd}\| \ll 1$ for an operator norm $\|\ldots\|$, the time-evolution operator can be expanded by $e^{-i\delta t H_{sd}} = 1 - i\delta t H_{sd} - \frac{1}{2}\delta t^2 H_{sd}^2 + \mathcal{O}(\delta t^3)$ and inserted

into Eq. (2.8), so that the combined state is given by

$$\rho_{sd}(t+\delta t) = \rho_{sd}(t) - i\delta t\,[H_{sd}, \rho_{sd}(t)] + \delta t^2 \mathcal{D}[H_{sd}]\rho_{sd}(t) + \mathcal{O}(\delta t^3), \tag{2.13}$$

where we note that $H_{sd}^\dagger = H_{sd}$ and $\rho_{sd}(t) = \rho_s(t) \otimes |0\rangle_{dd}\langle 0|$.

We now want to discuss different choices for the subsequent detector measurement basis $\{|\Phi(i)\rangle_d\}$ and the consequences for the system evolution.

Jump type

The first case considered is where the measurement basis is the same as the initialization basis, namely the computational basis $\{|0\rangle_d, |1\rangle_d\}$. In this case, the Kraus operators corresponding to the two possible measurement outcomes are given by

$$A_0 = {}_d\langle 0|e^{-i\delta t H_{sd}}|0\rangle_d, \quad A_1 = {}_d\langle 1|e^{-i\delta t H_{sd}}|0\rangle_d. \tag{2.14}$$

Before obtaining their explicit form in the weak-measurement limit, a renormalization of the off-diagonal matrix elements needs to be performed, where we define

$$H_L = H_s^{(0,0)}, \quad c = -i\sqrt{\delta t} H_s^{(1,0)}, \tag{2.15}$$

and we assume that $\delta t \left\| H_s^{(1,0)} \right\|^2 = \text{const.}$ for $\delta t \to 0$. This renormalization is necessary to correctly obtain the relevant terms of the evolution, depending on the measurement outcomes [21, 32], as the calculations below will show.

With this, the relevant terms for the weak-measurement form of our Kraus operators are

$$A_0 = 1 - i\delta t H_L - \frac{1}{2}\delta t c^\dagger c + \mathcal{O}\left(\delta t^2\right), \quad A_1 = \sqrt{\delta t} c + \mathcal{O}\left(\delta t^{3/2}\right). \tag{2.16}$$

The measurement probabilities can be written as

$$P_1 = \delta t \langle c^\dagger c\rangle + \mathcal{O}\left(\delta t^2\right), \quad P_0 = 1 - P_1. \tag{2.17}$$

Using these probabilities, we can now define a stochastic variable $\xi = 0, 1$, encoding the measurement outcome. This variable takes on the two corresponding values with probabilities P_0 and P_1, respectively, so that the average over different measurement outcomes is given by

$$\langle \xi \rangle_{\text{ms}} = P_1 = \delta t \langle c^\dagger c\rangle, \tag{2.18}$$

where we now drop the higher-order terms. All following equalities will hold within order δt.

With this, we can define a stochastic master equation (SME) dependent on ξ which models the evolution of our system state ρ_s according to the detector measurement. We compute the change in the system state as $\delta\rho_s(\xi) = \rho_s(\xi) - \rho_s = (1-\xi)\frac{A_0\rho_s A_0^\dagger}{P_0} + \xi\frac{A_1\rho_s A_1^\dagger}{P_1} - \rho_s$ with the probabilities

from Eq. (2.17). Since we are operating in the weak-measurement limit, we can expand the renormalization probability according to $\frac{1}{1-P_1} \approx 1 + P_1$, so that the SME then takes the form

$$\begin{aligned}\delta\rho_s(\xi) &= -i\delta t[H_L, \rho_s] - \frac{1}{2}\delta t\left\{c^\dagger c - \langle c^\dagger c\rangle, \rho_s\right\} + \xi\left(\frac{c\rho_s c^\dagger}{\langle c^\dagger c\rangle} - \rho_s\right) \\ &= \delta t\mathcal{L}\rho_s + \left(\xi - \delta t\langle c^\dagger c\rangle\right)\left(\frac{c\rho_s c^\dagger}{\langle c^\dagger c\rangle} - \rho_s\right). \end{aligned} \tag{2.19}$$

As noted, in this stochastic equation orders up to δt have been included, while ξ is treated as being of order δt according to Eq. (2.18). Thus, the factor $1-\xi$ in front of the term corresponding to the measurement outcome $\xi = 0$ does not matter within order δt and can be dropped [21, 26].

Similarly, for pure states, a stochastic Schrödinger equation (SSE) can be obtained from the Kraus operators (2.16). Here, we use the expansion $\frac{1}{\sqrt{1-P_1}} \approx 1 + \frac{P_1}{2}$, so that the SSE is obtained as

$$|\delta\Psi_s(\xi)\rangle = -i\delta t H_L|\Psi_s\rangle - \frac{1}{2}\delta t\left(c^\dagger c - \langle c^\dagger c\rangle\right)|\Psi_s\rangle + \xi\left(\frac{c|\Psi_s\rangle}{\sqrt{\langle c^\dagger c\rangle}} - |\Psi_s\rangle\right). \tag{2.20}$$

The SME (2.19) can be recovered from this SSE by noting that $\delta\rho_s(\xi) = |\delta\Psi_s(\xi)\rangle\langle\Psi_s(\xi)| + |\Psi_s(\xi)\rangle\langle\delta\Psi_s(\xi)| + |\delta\Psi_s(\xi)\rangle\langle\delta\Psi_s(\xi)|$ and using $\xi^2 = \xi$. Again, terms proportional to $\xi\delta t$ are neglected, since they are of higher order.

When considering the SME, it is possible to take the average over measurement outcomes, leading to, in general, a mixed state. The average can be simply performed by inserting the average over the stochastic variable ξ. From Eq. (2.20) it can be directly seen that

$$\langle\delta\rho_s\rangle_{\mathrm{ms}} = \delta t\mathcal{L}\rho_s = -i\delta t[H_L, \rho_s] + \delta t\mathcal{D}[c]\rho_s, \tag{2.21}$$

recovering a Lindblad EOM, as expected. We saw before that an average over measurement outcomes corresponds to tracing out the detector.

The derived stochastic equations are known as jump-type equations since measurement outcomes with $\xi = 1$ only happen rarely but come with a big, discontinuous state change. These outcomes are also known as *"clicks"*.

In the above derivation, δt has been assumed to be small but finite, in order to perform the renormalization in Eq. (2.15), with the measurement being instantaneous [21]. In particular, if δt becomes too small, the system evolution gets frozen if $H_L = 0$, which is known as the quantum Zeno effect [21]. Under the renormalization, the proper description in the limit of $\delta t \to \mathrm{d}t$ is obtained. Here, the stochastic variable ξ turns into a *differential* stochastic variable, often denoted dN, describing a *Poisson process*. As we saw above, it obeys the Itô calculus rules which we used implicitly, namely $\xi^2 = \xi$ and $\langle\xi\rangle_{\mathrm{ms}} \propto \delta t$. For more details on differential stochastic equations, see Ref. [31].

A second form of stochastic equations besides the description by jump equations is often discussed in the literature, which will appear naturally in the following by simply changing our

measurement basis.

Diffusion type

The second case that we want to discuss, measures the qubit along one of the orthogonal directions on the Bloch sphere, specifically along the x-axis, with measurement states defined as $|\pm\rangle_d = \frac{1}{\sqrt{2}}(|0\rangle_d \pm |1\rangle_d)$, corresponding to the eigenvalues ± 1 of τ^x. The τ^y-measurement follows in analogous fashion.

The corresponding new Kraus operators $A_\pm = {}_d\langle\pm|e^{-i\delta t H_{sd}}|0\rangle_d$ can be obtained from the operators A_ξ from Eq. (2.16) through a unitary transformation. For a more general description of how this transformation is defined for a general measurement basis, including the τ^y-measurement, see Appendix A.

We see that $A_\pm = \frac{1}{\sqrt{2}}(A_0 \pm A_1)$ holds. Thus, the new probabilities for the two measurement outcomes for weak coupling are given by

$$P_\pm = \frac{1}{2}\left(1 \pm \sqrt{\delta t}\langle c + c^\dagger\rangle\right), \tag{2.22}$$

after performing the rescaling of Eq. (2.15) and dropping terms of higher order. We can therefore define a new stochastic variable $\eta = \pm\sqrt{\delta t}$ for this type of measurement. The average over measurement outcomes is then given by

$$\langle\eta\rangle_{\text{ms}} = \sqrt{\delta t}(P_+ - P_-) = \delta t\langle c + c^\dagger\rangle, \tag{2.23}$$

so that it is again of order δt as in the jump-type case. However, in contrast to before, it now holds that $\eta^2 = \delta t$ without any stochasticity.

This new stochastic variable allows the definition of an alternative SME, leading to

$$\delta\rho_s(\eta) = \delta t\mathcal{L}\rho_s + \left(\eta - \delta t\langle c + c^\dagger\rangle\right)\left(c\rho_s + \rho_s c^\dagger - \langle c + c^\dagger\rangle\rho_s\right), \tag{2.24}$$

where we used the expansion $\frac{1}{1+\epsilon} \approx 1 - \epsilon + \epsilon^2$, with ϵ in this case being of order $\sqrt{\delta t}$, dropping terms proportional to $\eta\delta t \propto \delta t^{3/2}$.

For pure states, the dynamics can be again equivalently represented by the SSE

$$\begin{aligned}\delta|\Psi_s(\eta)\rangle = &\left(-i\delta t H_L - \frac{1}{2}\delta t c^\dagger c + \delta t\langle c^\dagger\rangle c - \frac{1}{2}\delta t\langle c\rangle\langle c^\dagger\rangle\right)|\Psi_s\rangle \\ &+ \left(\eta - \delta t\langle c + c^\dagger\rangle\right)(c - \langle c\rangle)\,|\Psi_s\rangle,\end{aligned} \tag{2.25}$$

which is only defined up to a global phase factor. In particular, this phase factor can depend on the stochastic variable η, giving different possible forms of the SSE corresponding to the same SME, which is known as the gauge-invariance of SMEs, see Ref. [26].

Note that this measurement corresponds to a detector measurement in the computational

basis where a unitary transformation has been performed on the detector *after* the combined evolution of system and detector. The unitary evolution of the detector after being entangled with the system, together with the measurement, influences the measurement-resolved dynamics of the system. However, an average over the measurement outcomes again corresponds to tracing out the detector space, eliminating the effect of the unitary transformation. As seen from Eq. (2.24), this average leads to the same Lindblad EOM (2.21) as for an average over the jump-type SME (2.19).

These new stochastic equations are known as being diffusive. In this case, the evolution corresponds to a random walk in the system Hilbert space since both measurement outcomes happen with almost equal probability, giving only slight deviations from the averaged evolution with a characteristic width of $\sqrt{\delta t}$ [31]. In particular, the stochastic variable η can be recentered by defining $\delta W = \eta - \langle\eta\rangle_{\mathrm{ms}}$, so that within order δt it still holds that $\delta W^2 = \delta t$ [21]. In the differential limit, it is described by a so-called Wiener process W, where dW is the infinitesimal Wiener increment, again obeying the corresponding Itô calculus rules and used to represent white noise [26, 31].

Diffusion equations are also known for describing so-called Homodyne and Heterodyne detection in quantum optics, where a beam splitter mixes the measurement signal with an additional oscillator mode [21, 26, 30, 31]. For Heterodyne detection, this oscillator needs to be detuned from the system frequency, introducing an additional time-dependent phase in the definition of the operator c [26, 30]. Here, this would correspond to a cycling between measuring in the eigenbases of τ^x and τ^y, see Appendix A.

In this section, we used stochastic equations to describe detector measurements. However, as we saw that an average returns to the Lindblad equation, we can also use stochastic equations to *unravel* Lindblad equations corresponding to the evolution of open systems described by Eq. (2.3). This method can be used for the numerical simulation of such dynamics [26, 31], as will be seen in Chapter 5.

2.2.3 Entanglement swapping

Another famous peculiarity of quantum mechanical measurements is the possibility of inducing entanglement between seemingly disconnected system parts. This phenomenon is mostly known as *entanglement swapping* or *quantum teleportation* [7] [33]. The basic principle is that entanglement between parties A(lice) and B(ob)1 and entanglement between parties B(ob)2 and C(harlie) is transformed by a suitable measurement into entanglement between parties A and C. The basic principle of this operation can be seen in Fig. 2.2 and is often used for applications in quantum communication [33].

In the aforementioned context of detector measurements, entanglement swapping corresponds to a detector consisting of multiple qubits and is now measured in an *entangled basis*. This stands in contrast to its initialization, where a multi-partite detector can be reasonably assumed to be

[7] The latter is more general and includes the teleportation of general (unknown) states [33].

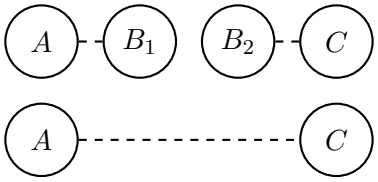

Figure 2.2: Evolution of entanglement in an entanglement swapping protocol. Entanglement between A and B_1, and between B_2 and C is swapped into entanglement between A and C by measuring B.

in a (disconnected) product state. This possible choice of the measurement basis is, of course, a feature of multi-partite systems, going beyond the previously discussed basis changes of single qubit detectors.

As before, a change of the measurement basis corresponds to a unitary evolution or transformation, performed on the detector after the combined system-detector evolution. This is especially instructive when considering the usual quantum circuit model. In particular, we use the following gates defined by the respective operator acting on one or two qubits [29]:

$$\text{CNOT} = \quad = \begin{pmatrix} 1 & 0 & 0 & 0 \\ 0 & 1 & 0 & 0 \\ 0 & 0 & 0 & 1 \\ 0 & 0 & 1 & 0 \end{pmatrix}, \quad -\boxed{H}- = \frac{1}{\sqrt{2}} \begin{pmatrix} 1 & 1 \\ 1 & -1 \end{pmatrix}, \quad \boxed{R_{\alpha_1,\alpha_2}(\phi)} = e^{-i\frac{\phi}{2}\sigma_1^{\alpha_1}\sigma_2^{\alpha_2}} \tag{2.26}$$

The controlled-NOT (CNOT) gate and the Hadamard gate H, together with the phase gate S, form the so-called Clifford group [8]. With the T gate, they can be used to define a universal gate set [8, 29]. We also introduced the two-qubit Pauli rotation gate $R_{\alpha_1,\alpha_2}(\phi)$, which we will use in subsequent chapters. Additionally, measurements in the computational basis that correspond to a projective measurement of σ^z are denoted by —⊡.

Now, let us discuss the simple example of two system and two detector qubits, all initialized in their respective $|0\rangle$ state. To perform entanglement swapping, we need to prepare two pairs of entangled states, each comprised of one system and one detector qubit. This can again be done by a unitary evolution which couples a system qubit to its corresponding detector qubit. In the usual nomenclature, system qubit 1 then corresponds to the party *Alice* and system qubit 2 to *Charlie* while both detector qubits belong to *Bob*.

The system-detector pair can be prepared in the state $(|00\rangle_{sd} + |11\rangle)_{sd}/\sqrt{2}$, which is one of the maximally entangled Bell states, by applying a Hadamard gate on the system qubit and a subsequent CNOT gate between both, as seen in Fig. 2.3. To perform the entanglement swapping,

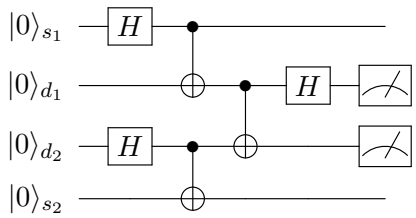

Figure 2.3: Quantum circuit which performs entanglement swapping between system qubits s and detector qubits d. Firstly, s_i and d_i are prepared in a maximally entangled state, and then a Bell measurement is performed on the detector. Depending on the measurement outcome ξ, η, the system is prepared in the Bell state $|\Phi_{\xi,\eta}\rangle_s$. See the main text for details.

both detector qubits are measured projectively in the Bell basis

$$\begin{aligned} |\Phi_{\xi=0,\eta=\pm}\rangle_d &= \left(|00\rangle_d \pm |11\rangle_d\right)/\sqrt{2}, \\ |\Phi_{\xi=1,\eta=\pm}\rangle_d &= \left(|01\rangle_d \pm |10\rangle_d\right)/\sqrt{2}. \end{aligned} \tag{2.27}$$

In a quantum circuit, this can be done by applying the unitary transformation containing one CNOT and one Hadamard gate with a subsequent measurement in the computational basis. The resulting system state comprised of s_1 and s_2 is then given by the Bell state $|\Phi_{\xi,\eta}\rangle_s = (|0\xi\rangle_s + \eta|1(1-\xi)\rangle_s)/\sqrt{2}$ depending on the measured state $|\frac{1-\eta}{2}\xi\rangle_d$ of the two detectors, where $\xi = 0, 1$ and $\eta = \pm$ encode the four possible measurement outcomes. To obtain a specific (Bell) state, the measurement outcome can be used to apply local transformations on the state after the measurement [33].

Thus, measurements can also be used to create entanglement in contrast to the often considered disentangling nature of measurements as used, e.g., in measurement-induced phase transitions [1]. We will make use of this feature of quantum measurements for our measurement-based state preparation protocols that will be presented in the following chapters.

2.2.4 Weak values

In preparation for Chapter 4, we want to briefly discuss another phenomenon present in weak measurements, known as weak values. They were first postulated by Aharonov, Albert, and Veidman in Ref. [34] in 1988 as the result of a pre- and postselected quantum measurement.

To obtain a weak value, one needs to initialize a quantum system in the initial state $|\Psi_i\rangle$ and weakly measure an observable A_1. Then, the resulting state is post-selected onto a final (or target, see next chapter) state $|\Psi_f\rangle$ by measuring another observable A_2 projectively.

The weak value of A_1 is then defined as

$$W_{A_1} = \frac{\langle\Psi_f|A_1|\Psi_i\rangle}{\langle\Psi_f|\Psi_i\rangle} = \frac{\mathrm{Tr}\left(\rho_f A_1 \rho_i\right)}{\mathrm{Tr}(\rho_f \rho_i)}, \tag{2.28}$$

where we used $\rho = |\Psi\rangle\langle\Psi|$ for pure states.

Remarkably, in contrast to the usual measurement results of a Hermitian observable during projective measurements, see Section 2.2, weak values can take on any value, including positive and negative and even complex values, outside the usually allowed range of (projective) eigenvalues of A_1 [34]. It can be seen that a necessary condition for such values is $[A_1, A_2] \neq 0$, such that both measurements do not commute [35].

We will see later how weak values naturally arise during the classical calculations of our state preparation protocol presented in Chapter 4. Beforehand, we want to discuss one of the limits for the measurements discussed here, namely, in terms of time scales.

2.2.5 Measurement time

Throughout this section, we have assumed that measurements are performed instantaneously, i.e., the measurement time τ_m should be far shorter than all other time-scales of the problem at hand, in particular

$$\tau_m \ll \delta t. \tag{2.29}$$

In practice, however, measurements are often the longest time-scales when running computations on quantum chips, in particular for current superconducting transmon qubits [2, 16], also carrying far higher error probability than single- and two-qubit gates [16]. As with other sources of errors, new device generations promise improvements in this respect, while other qubit architectures offer possible advantages, e.g., trapped ions with higher measurement fidelity but longer readout times [15]. In general, a more rigorous approach might be necessary for a full description, where a finite τ_m is included into the dynamics as an extra layer of system-only evolution, either unitarily or through a CPTP map when coupled to an environment. We leave this avenue for future work.

Let us now turn to the introduction of protocols that allow for state preparation utilizing the different dynamics introduced in this section, namely the interplay of unitary dynamics and measurements.

Chapter 3

Measurement-based target state preparation

In this chapter, we will discuss how measurements can be harnessed to *steer* quantum systems into a desired state. The steering is based on the previously introduced notion of so-called weak measurements. The coupling of the detectors to the system of interest can now be used to drive the system into a specific pre-chosen state by suitable interaction Hamiltonians. We will discuss different possibilities for how measurements are performed. Introducing active steering, this chapter gives the theoretical background for the steering protocols presented in the remainder of this work.

3.1 Passive steering

Already in the original formulation of quantum mechanics, Erwin Schrödinger noted the ability to influence a system's state by measuring another system that is entangled with the former [36]. He coined this phenomenon *quantum steering*.

In a more rigorous way, we want to introduce the term *steering* protocols as used in this work based on Ref. [14]. Such schemes make use of the back-action of measuring the so-called detector on the state of the system of interest in a controlled way. Building on the general formulation of the previous chapter, we now consider a protocol, where the system-detector coupling is used to *steer* the system to a predefined *target state* $|\Psi_f\rangle$. Ideally, the target state should be reached independently of its starting state [14]. To this end, the initially decoupled detector is prepared in a fixed state $|\Phi_0\rangle$ at time t. Then, for a time duration of length δt, system and detector are coupled by a coupling Hamiltonian H_{sd}, entangling both. At the end of this time step at time $t + \delta t$, the system and the detector are decoupled and the detector is measured projectively in a basis $\{|\Phi(i)\rangle\}$. This time step is now repeated multiple times, each time with freshly prepared detector states. A sequence of steering measurements in the time-continuum limit can then be seen as a continuous measurement which leads to a quantum trajectory of the system state inside

the Hilbert space.

A single time step is described by the following sequence of states:

$$\rho_s \to \rho_s \otimes |\Phi_0\rangle\langle\Phi_0| \to e^{-i\delta t H_{sd}} \rho_s \otimes |\Phi_0\rangle\langle\Phi_0| e^{i\delta t H_{sd}} \to \langle\Phi(i)|e^{-i\delta t H_{sd}}|\Phi_0\rangle \rho_s \langle\Phi_0|e^{i\delta t H_{sd}}|\Phi(i)\rangle \quad (3.1)$$

This definition of steering is in contrast to the one appearing in the literature, sometimes denoted *quantum steering* [37, 38]. Both go back to Schrödinger's original description of the aforementioned phenomenon [36], however, *quantum steering* in quantum information theory concerns itself with determining which different classes of states are influenced by the back-action of measuring a system entangled to another. We here restrict ourselves to the meaning of (measurement) steering as *guiding a state* towards a pre-designated target.

Following the nomenclature used in Ref. [18] for different classes of steering protocols, we first introduce *passive* steering protocols.

In passive steering, we assume the coupling H_{sd} to be the same in each time step. Therefore, along the course of the protocol, no further alterations are needed. The measurement outcomes can be used to stop the protocol, e.g., once a single "click" is measured, see also the previous chapter.

For the steering procedure to be scalable to many-body problems, it is useful to demand that the number of detectors, or more generally, the size of the detector space, should not scale faster than the system size. Also, we assume the coupling to be spatially local.

Note that in this chapter we discard any environment e. Additionally, we will restrict the following examples to the case where system and detector do not have any intrinsic Hamiltonians, i.e., $H_s = H_d = 0$.

As a simple example, one can consider a single system qubit coupled to a single detector qubit with the target state being $|\Psi_f\rangle = |0\rangle_s$. A suitable coupling Hamiltonian is given by [14]

$$H_{sd,1} = J\sigma^+\tau^- + h.c. \quad (3.2)$$

As in Chapter 2, we set our initial detector state to be $|0\rangle_d$. The evolution can most easily be understood when the detector measurement is done in the computational basis, leading to a jump-type evolution of the system qubit. The EOM is given by the SME (2.19) with $H_L = 0$ and the corresponding jump operator

$$c^{(1)} = \sqrt{\Gamma}\sigma^+, \quad P_1^{(1)} = \frac{1}{2}\Gamma\delta t(1 - \langle\sigma^z\rangle) \quad (3.3)$$

with the rate $\Gamma = J^2\delta t$. This then leads to the qubit state being in the target state $|0\rangle_s$ as soon as a "click" occurs, i.e., the detector state $|1\rangle_d$ is measured. If no "click" occurs, the measurement back-action leads to the state getting gradually closer to the target state as long as the state is not in the orthogonal state $|1\rangle_s$ [18]. Once the target state is reached, the "click" probability vanishes and the state stops evolving. In this way, reading out the measurement outcome speeds up the

steering process while increasing the target fidelity [18], compared to discarding the outcomes, which will be explained next.

3.1.1 Blind steering

As a further simplification and subclass of passive steering, we consider blind steering protocols as the ones where the measurement outcomes are not read out during the course of the protocol. Evidently, this corresponds to an average over all possible measurement outcomes, and the evolution is therefore defined by tracing out the detector.

Each time step now simplifies and can be represented in terms of the time evolution of the system density matrix introduced before, namely

$$\rho_s(t+\delta t) = \mathrm{Tr}_d\left(\rho_{sd}(t+\delta t)\right) = \mathrm{Tr}_d\left(e^{-iH_{sd}\delta t}\rho_s(t)\otimes\rho_d e^{iH_{sd}\delta t}\right), \tag{3.4}$$

where again $\rho_d = |\Phi_0\rangle\langle\Phi_0|$ is the detector density matrix at the beginning of each time step.

We saw before that in the weak-coupling limit, this results in an effective Lindbladian form of the EOM, see Chapter 2. One can think of the detector in this setting as an engineered environment acting on the system [14]. Due to the decoupling and reinitialization of the detector at the beginning of each time step, this environment is intrinsically Markovian [14]. In this way, such protocols are closely connected to drive-and-dissipation protocols, which make use of the interplay of environmentally induced dissipation and an applied drive to also prepare target states or target *dark* spaces [11, 12]. In contrast to environmentally induced jump-operators, blind steering allows engineering these operators by suitable couplings to target specific states. In particular, local couplings allow steering to eigenstates of unfrustrated local projector Hamiltonians [14].

For the simple example of a single qubit mentioned before, the EOM in the limit of blind steering is given by

$$\rho_s(t+\delta t) = \rho_s(t) + \delta t\Gamma\mathcal{D}[\sigma^+]\rho_s(t) \tag{3.5}$$

leading to the single dark state $|0\rangle_s$ as expected. In this case, the time evolution can also be computed exactly, giving an exponential decay towards the target as expected for the Lindblad evolution, see Ref. [14] and [18] for details. The target state is therefore reached in the long-time limit, irrespective of the initial state.

Next, we will go beyond passive and blind steering protocols by using the measurement results to change the coupling between system and detector along the course of the protocol.

3.2 Active steering

For the steering scheme presented before, no specific knowledge of our current state, except possibly at the end of the protocol, was needed. In this section, we want to introduce the notion of *active steering*. Here, we assume some (limited) knowledge of our time-dependent system state. Based on this knowledge, we are able to make *active* decisions that can improve our

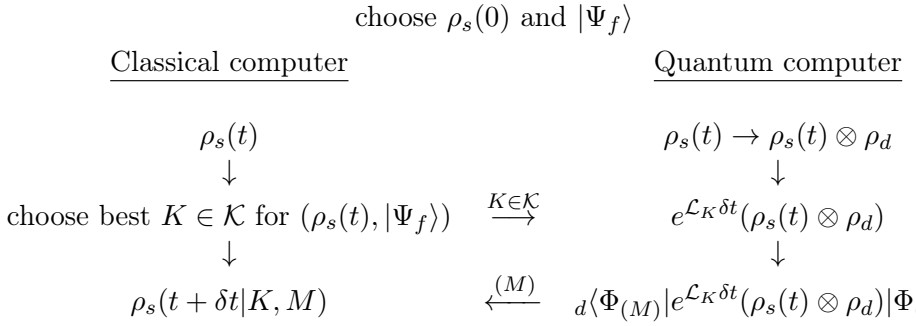

Figure 3.1: General active steering protocol: The classical computation determines the best possible coupling K out of the family of couplings $\mathcal{K}$, depending on the current system state $\rho_s(t)$ and the target state $|\Psi_f\rangle$. This choice is fed into the quantum computer as a coupling between system and detector. After a time evolution of length δt, given in general by a CPTP generator $\mathcal{L}_K$ depending on the chosen coupling, the detector is measured in the basis $|\Phi_{(M)}\rangle$, where (M) denotes the measurement outcome. This is fed back into the classical computer to keep track of the system state.

state-preparation protocol. Improvement can be in terms of a speedup of the time necessary to prepare the target state, or an improved fidelity with the target state after finite time [18]. In the next chapter, we will see that it is even possible to reach target states that are entirely impossible to prepare by a comparable blind steering protocol with local couplings.

We want to consider a measurement protocol, where the measurement results are used to alter the steering along the course of the evolution. Therefore, multiple system-detector couplings are needed, forming a coupling family $\mathcal{K}$, so that for each steering step as described before, one of the couplings $K \in \mathcal{K}$ can be chosen. As for the size of the detector space, also the number of different possible couplings should not scale faster than the system's size and respect reasonable locality restrictions (geometrically or in the operator space of composite systems) [18]. The *decision making* for the coupling choice should then be performed in such a way that the target state $|\Psi_f\rangle$ is approached as fast as possible or with the highest possible fidelity.

Note that passive protocols can also contain multiple couplings which can be chosen, e.g., in a cyclic way [18]. In contrast, for active steering protocols, the choice of the couplings should depend on the previous measurement outcomes, i.e., the running system state.

The general operation is depicted in Fig. 3.1. We assume to be operating a quantum machine, e.g., a quantum processor containing multiple qubits. The (abstract) decision making process is assumed to be performed automatically by classical processing done in parallel to the quantum evolution. Therefore, we have to keep track of our system by updating the system state according to the evolution given by coupling K and the outcome (M) of the detector measurement.

We note that the classical processing can be based on full knowledge of the quantum state ρ_s but also on having only partial knowledge by, e.g., keeping track of certain observables. In particular, environmentally induced errors might act on the state ρ_s, represented by an evolution under a Lindbladian $\mathcal{L}$. In general, such an evolution mixes the quantum state and spoils our

initially full knowledge of the state. Thus, questions arise on how strong these errors might become before rendering the decision making useless. We will explore this question in Chapter 5.

Throughout this process, all components of the protocol might carry inherent faults. However, we will always assume that at time $t = 0$ we have perfect knowledge of our state, which should be initialized in a pure (product) state, usually chosen to be $|0 \dots 0\rangle$ for a chain of qubits. This assumption is in agreement with the second DiVincenzo criterion for quantum computers, which states that it should be possible to initialize all the qubits of a quantum computer in a fiducial starting state [29, 39]. We also assume the detector preparation and measurement to be error-free, such that only environmentally induced errors will be present. We leave any extension of errors to future work.

Now, the question arises, how to perform the (classical) decision making process to prepare the target state $|\Psi_f\rangle$. This problem corresponds to finding the (best possible) path for the system state in its Hilbert space. While in principle one could tackle this task by exploring all coupling possibilities and measurement outcomes along the course of the protocol, this quickly becomes unfeasible. This is true even for small systems and short runtimes, even more so for many-body systems where the different possible couplings do not commute with each other, denoted as frustrated [18]. For this particularly interesting case, Ref. [18] put forward two possible heuristic decision making strategies, which we will discuss next.

3.2.1 Quantum state machines

One way of actively steering our system toward the target state is by using so-called Quantum state machines (QSM). The basic principle is to map the Hilbert space to a colored multigraph such that the vertices represent the basis states connected by different edges. These edges represent all possible transformations between basis states for the different couplings in our coupling set in different colors, where each measurement outcome in general gives a different evolution, represented by a separate edge. The state-preparation protocol then corresponds to finding the best path on this graph.

For the example described before of a single qubit coupled to a single detector qubit by the coupling Hamiltonian (3.2), the QSM can be seen in Fig. 3.2(a). Again, we see that once a measurement outcome $|1\rangle_d$ is detected, the state gets projected into the target state $|0\rangle_s$, represented by the solid blue edge. For this simple example, where the "no click" operator is described by $1 - \frac{1}{2}\delta t c^\dagger c$, cf. Eq. (2.16), the corresponding transitions for outcome $|0\rangle_d$ contain self-loops for all basis states (contribution of 1) and additionally, any transition which can be constructed by first following a "click" transition forward (corresponding to the action of c) and then another in the backward direction (corresponding to the action of $c^\dagger$), see Ref. [18] for a more thorough discussion. Here, only self-loops are present in Fig. 3.2(a); however, weight leaks into the target state $|0\rangle_s$ due to the measurement back-action (negative sign of the $c^\dagger c$ term).

As discussed, for a possibility for decision making, we need different couplings, so we addi-

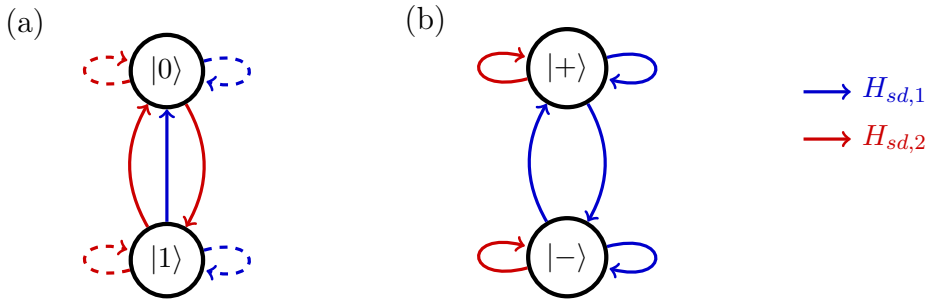

Figure 3.2: QSM showing the transitions in a qubit system corresponding to coupling Hamiltonians $H_{sd,1}$ from Eq. (3.2) (blue) and $H_{sd,2}$ from Eq. (3.6) (red) in (a) the computational basis and (b) the eigenbasis of σ^x. The "click" measurement outcome transitions are represented by solid lines, while the "no click" is shown in (a) by dotted lines. The "no click" transitions in (b) follow in the usual way, see Ref. [18] and the main text, and only contain self-loops.

tionally want to consider the second coupling Hamiltonian

$$H_{sd,2} = J\sigma^x\tau^x, \tag{3.6}$$

so that we obtain a second possible jump operator $c^{(2)} = \sqrt{\Gamma}\sigma^x$ with probability $P_1^{(2)} = \Gamma\delta t$. The corresponding evolution is shown in the QSM in Fig. 3.2 in red.

We see that if we are in the state $|1\rangle_s$, the second coupling can also bring us into the target by a single click. In all other cases, however, the target state cannot be prepared because the state continues to have non-zero overlap with the state $|1\rangle_s$ and does not prepare the target $|0\rangle_s$ with high fidelity. In fact, the state will just be flipped back and forth between the two states $|\Psi(0)\rangle$ and $\sigma^x|\Psi(0)\rangle$. The "no click" measurement outcome does not change the state and is therefore only represented by self-loops in Fig. 3.2(a).

The QSM representation for a given problem is not unique. We can perform a basis transformation, which might be useful for the decision making process, depending on the targets and the couplings. Therefore, an infinite amount of different representations of the system Hilbert space exist, where some might allow for a more efficient decision making [18]. Finding the best representation is not necessarily straightforward.

Fig. 3.2(b) shows the transformed QSM of the previous example when switching to the eigenbasis of σ^x. We see that while the possible evolution under $H_{sd,2}$ becomes clearer in this representation, the edges representing $H_{sd,1}$ now exhibit so-called interference effects, where edges from two vertices go into the same vertex. This is due to the fact that a general quantum state will be in a superposition of multiple states on the graph. In particular, this superposition can also be created by couplings with two outgoing edges from one vertex.

These quantum effects cannot be completely removed by a basis transformation, hindering the application of known path-finding algorithms on graphs [18]. However, it is possible to group parts of the system into blocks to obtain a coarse-grained representation of the QSM. These blocks

should then not exhibit quantum effects in their connections, facilitating the partial application of classical algorithms for the decision making process [18].

This QSM-based approach is partly limited by the size of the Hilbert space and the number of different couplings. Nonetheless, it is a useful technique when analyzing steering problems and coupling families, offering speedups compared to passive protocols [18] and helping in the visualization of active steering transitions.

A second way of performing active measurement steering introduced by Ref. [18] is using a so-called cost-function. While for certain problems this approach might be slower than decision making based on a QSM, it is more easily applicable to generic systems.

3.2.2 Cost function

For any state-preparation protocol, the distance of the running state to the target state is an important measure of the efficacy of the protocol. Therefore, it is useful to introduce a cost function $C(\rho_s, |\Psi_f\rangle)$, describing such a distance along the course of the protocol. Similar to certain methods known from (quantum) machine learning protocols [19], the goal of the state preparation protocol is then translated to minimizing such a cost function, where $C = 0$ corresponds to the successful preparation of the target state.

By evaluating the cost function during the protocol, we can introduce a decision making policy, choosing the coupling that takes the system to the global minimum of the cost function in the fastest possible time. In general, this task is again computationally expensive since for many-body states a combination of different couplings in multiple time steps will be necessary. Instead, we want to employ the so-called "greedy strategy" [18], where the expected consequences of different couplings on the cost function are evaluated for a single steering step. It is then useful to choose the coupling according to

$$\min_{K\in\mathcal{K}} C\left(\langle\rho_s(t+\delta t|K)\rangle_{\mathrm{ms}},\ |\Psi_f\rangle\right) \tag{3.7}$$

where $\langle\rho_s(t+\delta t|K)\rangle_{\mathrm{ms}}$ is the system state after a time step with coupling K averaged over all possible measurement outcomes. If multiple couplings minimize the expected cost function, one of these couplings can be chosen at random.

The appropriate choice of the cost function can highly depend on the problem at hand. The intuitive first choice of using the *infidelity* $C(\rho_s, |\Psi_f\rangle) = 1 - \langle\Psi_f|\rho_s|\Psi_f\rangle$ to encode the distance between running and target state allows the acceleration of the preparation of Matrix product states, see Ref. [18]. Also, for our example above, this cost function choice will prefer the correct coupling $H_{sd,1}$ to prepare the target state $|0\rangle_s$. However, already Ref. [18] noted that for general many-body systems, such a global cost function will suffer from its flatness in the landscape of the Hilbert space since most states will be orthogonal to the target state. Additionally, for blind steering protocols, the possibly non-monotonous approach towards the target state of many-body problems was noted in Ref. [14], depending on the choice of the function describing the distance

between the current and target state. Both effects are caused by the assumed locality of the steering procedures, making an appropriate choice of the cost function necessary. Such a cost function should, therefore, include both local and global terms to correctly monitor the distance of the running state to the target and allow for an active steering procedure, as will be seen in Chapter 4.

Compared to the QSM approach, the cost function approach can be, in general, more easily adapted to changes in the protocol, both to the target state and the available couplings. However, it comes at a cost of a classical calculation, which for a scalable protocol should be kept at a minimum. In particular, if full knowledge of the state is needed, the classical simulation will be bounded by the limits of the classical simulability of quantum systems. Therefore, it is necessary to define the cost function as a function of local observables or correlations in the system state whose number should scale slower than the Hilbert space size. Steps in this direction will be taken in Chapters 5 and 6; however, it remains a highly complex and generally unsolved problem.

The remainder of this work introduces new active steering protocols based on different kinds of cost functions in order to prepare certain classes of target states. These protocols will make use of dynamics only present when actively reading out measurement outcomes with no passive counterpart. In particular, we will show how states that are inaccessible to passive steering by local couplings can be prepared actively. Before presenting these results, let us discuss some limitations of such active protocols as well as possible extensions, which might be interesting to explore in future works.

3.3 Extensions and implementation

Throughout this thesis, we will always consider systems where one detector qubit is needed per system qubit as presented above. For an improvement in scalability, it is of course useful to reduce the number of detector qubits as much as possible. There has been work on dilute systems for passive steering, see Ref. [40], where it is possible to reduce the setup to a single detector qubit under certain conditions on the target state and the coupling family. Investigating these possibilities for active steering protocols might, therefore, be an interesting route in the future.

Additionally, we do not discuss the preparation of specific mixed states by active steering, which has been examined for blind steering in Ref. [41].

As mentioned, the only source of errors we will consider in this work is a coupled (Markovian) environment. This can be extended to more complex error models, in particular by introducing errors in the detector initialization and measurement and its coupling to the system, as done in Ref. [32] for blind protocols. Also, the analysis of inefficient detector measurements might be of importance for an experimental realization of measurement steering [26, 31].

As discussed at the end of Chapter 2, in general, measurement times need to be accounted for in practical realizations of these protocols. In particular, for the current generation of NISQ devices, especially superconducting qubits, mid-circuit measurements pose a great obstacle during

computations [2, 3]. In practice, measurements are therefore often performed at the end of the experiment [4], e.g., by transforming the circuit using space-time duality mappings, introducing a significant overhead of additional qubits [3]. In general, it is possible to use the principle of deferred measurements, where measurements can be moved to different positions in the quantum circuit [4, 29]. However, this process is not feasible when running the discussed active steering protocols, where the measurement outcomes are needed *during* the steering run to track the system state. Thus, other architectures like Andreev qubits [17], see Chapter 5, or new generations of devices, allowing for mid-circuit measurements [2], will prove useful in order to apply the findings of this thesis in practice. Nonetheless, first experiments with current-generation devices have been performed and showed moderate success in passive steering [42], leading to the hope for practical applications of these protocols in the near future.

The next chapter will show the main result of this thesis by introducing a cost function-based active steering protocol, which will form the basis of all following results.

Chapter 4

Engineering unsteerable quantum states with active feedback

This chapter is taken from Ref. [22]. My contributions are listed in the List of publications after the appendix. Building on the descriptions of measurements using stochastic equations, we introduce a cost function-based active protocol using entanglement swapping measurements in order to target arbitrary many-qubit states. Additional information on the coupling sets between system and detector and additional equations are shown in Appendix B. There, we also introduce the exact expressions of the system's evolution, going beyond the weak measurement limit used in Ref. [22].

The previously used subscript s denoting system states is mostly dropped in instances where it is clear which state is referred to.

4.1 Introduction

Solving complex tasks by means of control and feedback circuits is of ubiquitous importance in the modern world. A famous example is the Apollo space mission, where optimal control enabled a spaceship to smoothly land on the moon with vanishing target velocity. Can one design a similar strategy where one "steers" a *quantum* system at will towards a predesignated target state? In the quantum case, exerting "control" over the system requires the ability to perform quantum measurements while "feedback" may arise from unitary Hamiltonian dynamics and from measurement backaction [26, 29]. While the analogy to the classical case sounds appealing, quantum mechanics imposes several fundamental differences. In particular, the probabilistic outcome of quantum measurements implies that the state dynamics will resemble a random walk where quantum jumps can cause large state changes. The present work explores the potential of such approaches in the context of quantum state preparation for a system of N qubits. Our ideas may be tested in different platforms of current interest [2, 4, 15, 16, 43–49], including superconducting qubit arrays, trapped ion setups, photonic circuits, and ultracold atom lattices.

Quantum state preparation in general represents a complex challenge [26, 29]. One possible avenue is to employ deterministic schemes, without feedback from measurements over the course of the protocol. For sufficiently small N, applying a sequence of single- and two-qubit unitary gates (that is, a quantum circuit) is an option. However, with increasing N, a deterministic gate sequence leading from a given initial state $|\Psi(0)\rangle$ to a predesignated and possibly highly entangled final target state $|\Psi_f\rangle$ is generally difficult to identify and requires an exponential overhead of additional ancilla qubits [50]. If $|\Psi_f\rangle$ represents a non-degenerate ground state of a gapped local Hamiltonian, one can resort to analog quantum simulations and/or quantum annealing or cooling methods [51], where the corresponding Hamiltonian is implemented in a controlled and tunable way, e.g., using lattices of trapped ions or ultracold atoms weakly coupled to a thermal environment. For very low temperature, the quantum state then dynamically evolves towards the ground state $|\Psi_f\rangle$. However, such approaches may become impractical if the Hamiltonian is gapless. Moreover, a certain class of states cannot be expressed as ground states of a "parent Hamiltonian," the latter being the sum of local Hamiltonians. Examples are exotic highly entangled N-qubit states such as the Green-Horne-Zeilinger (GHZ) state and the W state [29, 52]. Written in the standard basis defined by Pauli-Z operators,

$$\begin{aligned} |\mathrm{GHZ}\rangle &= \frac{1}{\sqrt{2}}(|00\cdots0\rangle + |11\cdots1\rangle), \\ |\mathrm{W}\rangle &= \frac{1}{\sqrt{N}}\left(|10\cdots0\rangle + |01\cdots0\rangle + \cdots + |00\cdots1\rangle\right), \end{aligned} \tag{4.1}$$

represent two state classes with different types of high multipartite entanglement for $N > 2$ qubits [52], where $|\mathrm{GHZ}\rangle$ (resp., $|\mathrm{W}\rangle$) is a superposition of two (resp., N) product states.

In this work, we instead study measurement-based strategies where the protocol is designed to autonomously find a desired target state of arbitrary form. It is widely recognized that quantum measurements offer great freedom in shaping and controlling the dynamics of quantum many-body systems, far beyond the possibilities offered by the unitary Hamiltonian dynamics of closed systems or the dissipative dynamics of driven open systems [26, 29, 31, 53–55]. For instance, the interplay of projective measurements of stochastically selected qubits with the unitary dynamics due to local two-qubit random gates causes nontrivial entanglement phase transitions in random quantum circuits, see Ref. [1] for a recent review. By allowing for projective measurements on detector qubits weakly coupled to the system qubits, weak measurement protocols can be designed for "steering" the system state $|\Psi(t)\rangle$ towards a desired target state $|\Psi_f\rangle$, as discussed in Chapter 3.

Importantly, there are major obstacles which can prevent the success of passive steering. First, while a state may in principle be passively steerable, the required steering operators can be so complicated that they are not available for the hardware at hand. Second, more fundamentally, it is impossible to passively steer certain state classes by *any* set of *local* steering operators. This is the case if the state cannot be represented as a ground state of a non-frustrated parent

Hamiltonian [13]. The active steering protocols detailed in this work can overcome the no-go theorem of passive steering in Ref. [13] for two reasons: (i) In an active protocol, one follows the time evolution of the state and takes the decision (which steering operator is applied during the next time step) based on the history of previous measurement outcomes. (ii) Unlike with standard passive protocols, an important part of the state dynamics now comprises manipulations or measurements of the detector qubits. In our implementation, we introduce a weak-measurement variant of entanglement swapping (for details, see below).

It is worth emphasizing that previous applications of active decision making to the problem of steering, cf. Ref. [18], have only used sets of "passive" measurement operators, i.e., operators which allow one to passively steer the system at long times. The goal was to accelerate steering by properly choosing — based on the current system state — one of the available operators at each step of the protocol. In the present work, a much more challenging question is addressed and solved: Is it possible to actively steer the system using a set of local measurement operators that would never yield the desired target state without active decisions?

Important examples for passively unsteerable (by local[1] steering) N-qubit states are given by the GHZ and W states, see Eq. (4.1). While tracing over a single qubit implies an only classically correlated reduced density matrix (RDM) for the remaining qubits for the GHZ state, the W state is more robust against entanglement loss. Highly entangled states such as those in Eq. (4.1) can be used as a resource [56], e.g., for increasing the sensitivity of quantum detectors [7, 57, 58]. We note that the GHZ state is a stabilizer state which can be prepared by projective measurements of a set of commuting products of Pauli operators (stabilizers) augmented by Clifford operations or postselection if one measures "wrong" stabilizer eigenvalues [8, 29]. Previous measurement-based state preparation experiments, see, e.g., Refs. [59–62], have typically been limited to stabilizer states. Related ideas for preparing topologically ordered states in the large-N limit have been described in recent works [14, 49, 63–73]. However, the underlying strategies apply only in special cases where, for instance, all measurement operators commute with all unitary gates.

In this work, we show that passively unsteerable states, including non-stabilizer states such as the W state, can be prepared by active steering protocols using only a limited, and usually available, set of simple steering operators. Even if $|\Psi_f\rangle$ is passively steerable, active steering will usually result in significantly faster protocols. In general, active steering protocols involve decision making strategies where (a part of) the history of measurement outcomes is taken into account in the subsequent time evolution [18, 20, 43, 74–80]. In our protocol, we consider N system qubits, each of which is allowed to couple only to its own detector qubit partner, see Fig. 4.1(a) for a schematic illustration. The respective system-detector coupling ("steering operator") is chosen

[1]We reiterate that the condition of locality here is crucial: the no-go theorem on steerability assumes steering operators acting only on a local subset of the system degrees of freedom (which does not scale up with system size). For example, in Ref. [18], passive steering of a three-qubit W state was addressed, which became possible because one of the steering operators used there involved all three qubits, thus representing "global steering." In what follows, passively unsteerable states are understood as those that cannot be passively steered by applying local operators.

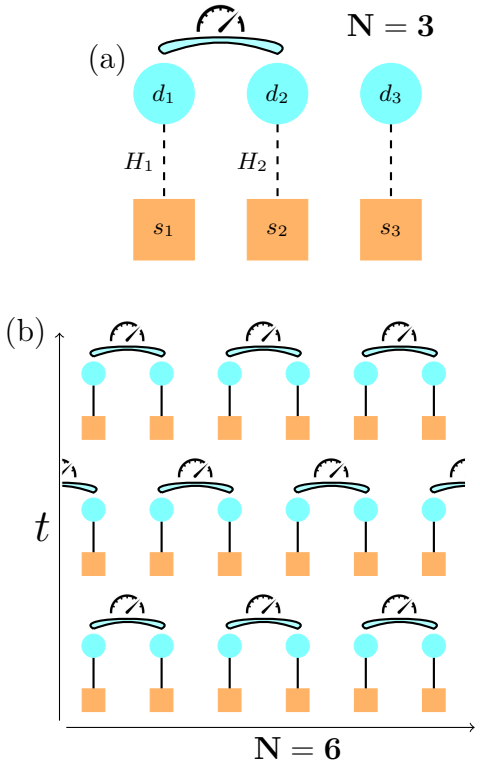

Figure 4.1: Cartoon of the active steering protocol. (a) N system qubits (orange squares, here shown for $N = 3$) are coupled to the respective detector qubit (blue circles) by selected Pauli steering operators (here denoted by H_1 and H_2), see Eq. (4.4) below. After a unitary time step, projective Bell measurements of neighboring detector qubit pairs (in this example for qubits 1 and 2, with qubit 3 not being measured) implement weak local Bell measurements for the state $|\Psi\rangle$ of the system qubits (entanglement swapping, see Fig. 4.2 for details). (b) Time evolution of the monitored quantum circuit with active feedback, shown for three time steps of a chain of $N = 6$ qubits with periodic boundary conditions. A possible scheme for Bell measurements of neighboring detector qubit pairs in subsequent cycles is indicated. For details, see main text.

from a small set of Pauli operators, where the choice is determined by an active decision making strategy. We emphasize that direct couplings between system qubits are not needed and only a single steering operator (not superpositions thereof) is applied during a given time step of duration δt. One cycle then corresponds to a sequence of the following operations, see Fig. 4.1(b):

1. One prepares the detector qubits in a simple product state.

2. The chosen steering operators (see below for our active decision making policy) are switched on and unitary time evolution sets in.

3. After the time δt has elapsed, the steering operators are switched off again. One now performs projective Bell measurements on neighboring detector qubit pairs. The measurement outcomes are used for selecting the steering operators in the next cycle.

Since steering operators associated with different system qubits commute by construction, and measurement operators for distinct (non-overlapping) qubit pairs commute as well, one can simultaneously steer $[N/2]$ pairs in a given time step, cf. Fig. 4.1(b).

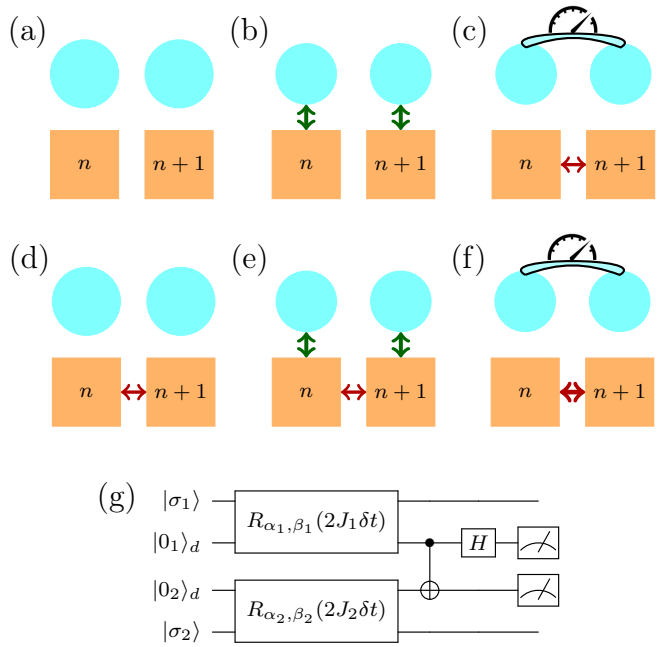

Figure 4.2: Schematic illustration of entanglement generation during one time step of the protocol. We use a weak-measurement variant of entanglement swapping [33, 81–87], where one steers the neighboring system qubits $(n, n+1)$ indicated by squares. Circles depict the corresponding detector qubits as in Fig. 4.1. (a) Configuration at initial time $t = 0$, where all qubits are decoupled from each other. (b) At time δt (after one time step), each system-detector qubit pair is entangled (green vertical arrows) due to unitary time evolution under the chosen steering operators. (c) After a projective Bell measurement of the detector pair, system and detector qubits disentangle and, depending on the measurement outcome, entanglement between the system qubits (red horizontal arrow) builds up. Panels (d)-(f) show the corresponding steps during the subsequent time step of the protocol, where entanglement generated in the previous time step is already present. Typically, entanglement increases after the Bell measurement (thicker red horizontal arrow). (g) Quantum circuit representation of entanglement swapping. The Pauli rotations (R) depend on the chosen steering operators (see Sec. 4.2.1 for details) and act on system and detector qubits, with a subsequent measurement of the detector qubits in the Bell basis. System (detector) qubit states are here denoted by $|\sigma_{1,2}\rangle$ ($|\sigma_{1,2}\rangle_d$). The Bell basis measurement is achieved by CNOT and Hadamard gates.

The above Bell measurements realize weak measurements on the system qubits and provide an efficient way to systematically generate entanglement in $|\Psi\rangle$ by means of a weak-measurement version of entanglement swapping [33, 81–87], where entanglement is incrementally teleported from the detector qubits to the system qubits, as introduced in Section 2.2.3. (We simply refer to "entanglement swapping" in what follows.) We illustrate the basic mechanism in Fig. 4.2, where $|\sigma_{n,n+1}\rangle$ ($|\sigma_{n,n+1}\rangle_d$) with $\sigma = 0, 1$ refer to basis states of the respective system (detector) qubits

n and $n+1$. In panels (a)-(c), we consider the first cycle of the protocol, starting at the initial time $t = 0$: (a) One starts from the simple product state $(|0_n\rangle \otimes |0_n\rangle_d) \otimes (|0_{n+1}\rangle \otimes |0_{n+1}\rangle_d)$. (b) Switching on the selected steering operators during a time step of duration δt, each system and detector qubit pair are entangled by the unitary time evolution. (c) The subsequent projective Bell measurement of the detector qubits then disentangles the system and detector qubits but at the same time generates entanglement among the system qubits by means of entanglement swapping. Next, in panels (d)-(f) we illustrate what happens during the next cycles of the protocol: (d) As a result of the last step, some entanglement may now be present in the system state $|\Psi(\delta t)\rangle$, before one applies the steering operators for the next step. (e) After the unitary time step, each system-detector qubit pair becomes entangled. (f) One performs again a Bell measurement, which typically increases the entanglement in the resulting state $|\Psi(2\delta t)\rangle$. Finally, we provide a quantum circuit representation of this entanglement swapping protocol [29] in Fig. 4.2(g). A detailed discussion of our entanglement swapping protocol can be found in Sec. 4.2.1.

We emphasize that the re-initialization of detector qubits after the measurements is possible in our scheme, see also Refs. [2, 42]. Without such a property, the number of detector qubits would proliferate for large circuit depth. Moreover, since the implementation of such measurements only requires two-qubit interactions, we expect that entanglement swapping is easier to realize experimentally than, for instance, the generation of entanglement through measurements done on single detector qubits coupled to two or more system qubits. In fact, one can show that in the latter setup, with a fixed set of Pauli steering operators, it is not possible to reach arbitrary target states $|\Psi_f\rangle$, not even for $N = 2$. As shown below, entanglement swapping does not suffer from this problem. Measuring a pair of qubits in their Bell basis also is a standard procedure in many platforms of current interest. More generally, we find that an arbitrary state obtainable by consecutively entangling pairs of qubits, say, by applying two-qubit gates, can also be engineered by means of active steering based on entanglement swapping. In principle, this includes highly entangled states with volume-law growth of the entanglement entropy.

In order to make progress, we consider an idealized situation free from external noise or other imperfections [32]. In particular, we assume that the parameters characterizing allowed steering operators are known from prior calibration runs. If the initial pure state $|\Psi(0)\rangle$ (e.g., an easily accessible product state) and the measurement outcomes are known, one can then track the state trajectory $|\Psi(t)\rangle$ at later times $t = m\delta t$ (integer m) by a classical calculation. (For a given measurement record, $|\Psi(t)\rangle$ always remains pure. By averaging over measurement outcomes, one may obtain a mixed state.)

For moderate values of N, those assumptions may be justified to reasonable accuracy on time scales below the respective qubit dephasing time. This case is also of practical interest if parts of the system can be steered locally and the whole system is then composed of small-N blocks, see Ref. [73] for related work. A different perspective is to run our protocol on a fault-tolerant circuit with quantum error correction [8, 29, 88–95], where all system and detector qubits are encoded logical qubits. Errors related to external noise can thereby be detected and actively

corrected. We note that recent experimental works managed to beat the break-even point for fault tolerance of a logical qubit [96, 97]. In Sec. 4.4.3, potential extensions of our protocol to noisy quantum circuits will be discussed, see also Ref. [32]. While we show numerical simulation results based on the present formulation of our active steering protocol only for $N \leq 6$ system qubits in Sec. 4.3, we expect that large values of N can be reached using closely related protocols, see Sec. 4.4.2. Our work represents a proof of concept that active steering protocols can reach passively unsteerable target states.

A central element of our approach is active feedback: based on the measurement outcomes recorded after a given time step, the steering operators used in the next time step are determined by optimizing a non-negative cost function $C(t)$. Convergence, i.e., $|\Psi\rangle = e^{i\gamma}|\Psi_f\rangle$ with arbitrary global phase γ, is reached only for $C = 0$, such that one has to minimize $C(t)$. In practice, for each steering parameter configuration K, we compute the expected cost function change in the next time step,

$$\langle dC(K)\rangle_{\rm ms} \equiv \langle C(t+\delta t;K)\rangle_{\rm ms} - C(t), \tag{4.2}$$

where $\langle\dots\rangle_{\rm ms}$ indicates an average over measurement outcomes. The steering operator K is then chosen to maximize the cost function gain $|\langle dC(K)\rangle_{\rm ms}|$ with $\langle dC(K)\rangle_{\rm ms} \leq 0$. For a proper cost function, and assuming a sufficiently large ("universal") steering operator set, $\langle dC(K)\rangle_{\rm ms} < 0$ is required for at least one K unless one has already reached convergence. An obvious cost function candidate is related to the fidelity F [29],

$$C_N = 1 - F^2, \quad F = |\langle\Psi_f|\Psi\rangle|. \tag{4.3}$$

However, Eq. (4.3) is *not* sufficient for our active steering protocol. For instance, consider steering from $|\Psi\rangle = |00\cdots0\rangle$ to $|\Psi_f\rangle = |11\cdots1\rangle$. Flipping single (or a few) qubits, $|0\rangle \to |1\rangle$, evidently brings one closer to the target state, yet the resulting state remains orthogonal, $F = 0$, unless one flips all N qubits simultaneously. In essence, we encounter a situation reminiscent of Anderson's orthogonality catastrophe [98] with similarities to the barren plateau problem in machine learning [99]. In any case, when using Eq. (4.3) as cost function, active steering will generally fail. This failure already affects the minimal case $N = 2$, see Sec. 4.2.3 for details, and becomes more severe with increasing N. We show below that by incorporating "local" fidelity cost function terms, this problem can fortunately be resolved. ("Locality" is here meant in the sense of operator locality.) For all possible RDMs for $r < N$ qubits built from $|\Psi(t)\rangle$, those terms minimize a suitable operator distance measure between the RDM and the respective RDM constructed from $|\Psi_f\rangle$. We address convergence properties of the resulting active steering protocols in Sec. 4.2.4.

The structure of the remainder of this chapter is as follows. In Sec. 4.2, we discuss the detailed quantum state dynamics of the actively monitored circuit described above. In Sec. 4.3, we present numerical simulation results to illustrate the performance of the active steering protocol. We then discuss implementation aspects and summarize possible perspectives for future work in Sec. 4.4.

4.2 Active steering protocol

We now turn to a quantitative description of the active steering protocol. The measurement-conditioned dynamics of the quantum circuit in Fig. 4.1 is analyzed in detail in Sec. 4.2.1. For concreteness, we study a chain of N system qubits with periodic boundary conditions, where each system qubit can be coupled to a detector qubit. However, our protocol can easily be adapted to other circuit geometries. In Sec. 4.2.2, we summarize the Bloch tensor state representation, which considerably simplifies the subsequent steps. We proceed with an analysis of the active decision making strategy in Sec. 4.2.3, which crucially depends on the construction of a cost function employed in the optimization process. Utilization of a global fidelity cost function introduces "weak values" [34] into the ensuing stochastic evolution equation. Using these weak values, we show that successful active steering is only possible if local fidelity terms are added to the cost function. Finally, we discuss convergence aspects in Sec. 4.2.4. Additional details can be found in Appendix B.2.

4.2.1 Stochastic Schrödinger equation

In what follows, system qubits are described by the operators σ_n^μ, where $n = 1, \ldots, N$ labels the qubits, $\mu = 0$ corresponds to the identity, and for $\mu = \alpha \in \{1, 2, 3\} = \{x, y, z\}$, we have standard Pauli matrices. Similarly, detector qubits correspond to the operators τ_n^μ. For clarity, we assume below that all states of the uncoupled system qubits and, separately, all states of the detector qubits are degenerate, assigning to them zero energy. In other words, we assume no intrinsic Hamiltonian of the system and detector qubits. During a unitary time evolution step, a steering operator H_{n,K_n} can couple the system qubit σ_n with the corresponding detector qubit τ_n, where K_n is chosen from a set of allowed steering parameters. We here consider Pauli steering operators,

$$H_{n,K_n} = s_n J_n \sigma_n^{\alpha_n} \tau_n^{\beta_n}, \tag{4.4}$$

with the sign $s_n \in \{1, -1\}$ and the Pauli operator indices $\alpha_n \in \{x, y, z\}$ and $\beta_n \in \{x, y, z\}$. (Identity operators acting on other qubits are often kept implicit below.) Clearly, the steering operators in Eq. (4.4) commute for $n \neq n'$. We stress that for each pair (σ_n, τ_n), only a single Pauli operator couples the respective system and detector qubit during a given time step — no superpositions of different Pauli operators are needed in our protocol. The coupling constants $J_n > 0$ are assumed to be fixed and known, such that the available steering operators are parametrized by $K_n = (s_n, \alpha_n, \beta_n)$. Without loss of generality, the sign s_n can be restricted to $s_n = +1$ for $\beta_n \neq z$, implying a set of 12 possible steering parameters $\{K_n\}$. Further reductions of the steering operator set are possible in special cases. For instance, we empirically find that in order to prepare the GHZ state, one can exclude steering operators with $\beta_n = y$. Such operators are, however, needed for the W state. Determining the minimal set of steering operators required for achieving convergence to general target states remains an interesting open issue.

Let us now consider a specific nearest-neighbor qubit pair $(n, n+1)$ as illustrated in Fig. 4.2. Before each unitary time evolution step, the corresponding detector qubits are initialized in a simple product state, say, $|00\rangle_d$. (The index d distinguishes the detector Hilbert space from system space.) Subsequently, the steering operator $H_K = H_{n,K_n} + H_{n+1,K_{n+1}}$ is switched on for suitably chosen steering parameters $K = (K_n, K_{n+1})$, and unitary time evolution of the full system sets in. After the time step δt with $J_{n/n+1}\delta t \ll 1$, the steering operator H_K is switched off again, and one projectively measures the detector pair in its Bell basis $|\Phi_{\xi,\eta}\rangle_d$ [29], see Eq. (2.27), where symmetric ($\eta = +1$) and antisymmetric ($\eta = -1$) Bell states have either even ($\xi = 0$) or odd ($\xi = 1$) parity. Here "symmetry" refers to the behavior of the state under exchange of the two qubits, while even (odd) "parity" means that it is built from the basis states $\{|00\rangle_d, |11\rangle_d\}$ ($\{|01\rangle_d, |10\rangle_d\}$). Since the initial state $|00\rangle_d$ obviously has even parity, we refer to measurement outcomes with $\xi = 1$ as "quantum jumps". By means of entanglement swapping [33, 81–87], see Fig. 4.2, one can then generate entanglement in the system state $|\Psi\rangle$, where the binary stochastic variables ξ and η encode the measurement outcomes. Their probabilistic nature is a fundamental consequence of quantum mechanics. We emphasize that the above Bell measurements are local in the sense that only nearest-neighbor detector pairs are probed. In practice, they can be implemented by simultaneously measuring two commuting Pauli operators for detector qubit pairs [29],

$$\mathcal{O}^x = \tau_n^x \tau_{n+1}^x, \quad \mathcal{O}^z = \tau_n^z \tau_{n+1}^z. \tag{4.5}$$

Indeed, one easily checks that

$$\mathcal{O}^x |\Phi_{\xi,\eta}\rangle_d = \eta |\Phi_{\xi,\eta}\rangle_d. \quad \mathcal{O}^z |\Phi_{\xi,\eta}\rangle_d = (1-2\xi)|\Phi_{\xi,\eta}\rangle_d. \tag{4.6}$$

A projective measurement of the Bell state $|\Phi_{\xi,\eta}\rangle_d$ thus implies that one measures the eigenvalues $\mathcal{O}^x = \eta (= \pm 1)$ and $\mathcal{O}^z = +1$ (for $\xi = 0$) or $\mathcal{O}^z = -1$ (for $\xi = 1$) for the observables in Eq. (4.5). Finally, we note that for the quantum circuit in Fig. 4.2(g), in the computational basis of the two detector qubits, the measurement has the possible outcomes $|\frac{1-\eta}{2}, \xi\rangle_d$.

For measurement outcome (ξ, η) after a completed time step, the state of the full system is given by $|\Psi(t+\delta t)\rangle \otimes |\Phi_{\xi,\eta}\rangle_d$, where the system state $|\Psi(t+\delta t)\rangle$ depends on (ξ, η) because of entanglement swapping, see Fig. 4.2. In our protocol, since direct couplings between system qubits are absent, entanglement is solely generated (or removed) through the above Bell measurements. Upon re-initializing the detector pair, the full state is prepared for the next time step as $|\Psi(t+\delta t)\rangle \otimes |00\rangle_d$. Since all measurement operators $\mathcal{O}^{x,z}$ for non-overlapping pairs commute, and also the corresponding steering operators H_K commute, one can simultaneously steer and measure $[N/2]$ distinct pairs in one time step. For instance, for $N = 4$ qubits, we could steer the qubit pairs $(1, 2)$ and $(3, 4)$ in the first cycle, and then the pairs $(2, 3)$ and $(4, 1)$ in the second cycle. We do not allow for next-nearest-neighbor couplings within our notion of locality, i.e., only adjacent detector qubit pairs are subject to Bell measurements. Hence, direct pair-steering of $(1, 3)$ and $(2, 4)$ is not taken into account. In general, for subsequent time steps, one can choose

either a random pattern or an alternating pattern of measurement pairs; the latter case is shown in Fig. 4.1(b). We find that a randomized pair assignment gives slightly superior convergence properties, but both schemes work well in practice.

Given the above remarks, it suffices to analyze the state change in one time step when steering and measuring only a single pair $(n, n{+}1)$. For the measurement outcome (ξ, η), the state $|\Psi(t{+}\delta t)\rangle$ after the measurement is obtained by using the Kraus operators $A_{\xi,\eta} = {}_d\langle\Phi_{\xi,\eta}|e^{-i\delta t H_K}|00\rangle_d$ and the outcome probabilities $P_{\xi,\eta}$ [26, 29, 31], as discussed in Section 2.2.

In the weak measurement limit [26], the couplings J_n and the time step δt are adjusted such that the rates

$$\Gamma_n = J_n^2 \delta t \tag{4.7}$$

are effectively independent of δt and satisfy $J_n \delta t = \sqrt{\Gamma_n \delta t} \ll 1$. We assume this limit throughout.

Expanding the Kraus operators to lowest nontrivial order in δt, we then obtain

$$A_{\xi,\eta} = \sqrt{\frac{\delta t}{2}}\xi c_\eta + \frac{1}{\sqrt{2}}(1-\xi)\left[1 - i\delta t\left(H_\eta - \frac{i}{2}c_\eta^\dagger c_\eta\right)\right], \tag{4.8}$$

where the effective Hamiltonian H_η and the jump operators c_η act on the system Hilbert space. These quantities apply to a given time step and for the chosen qubit pair $(n, n+1)$. We note that H_η only appears in Eq. (4.8) if one measures the same (even, $\xi = 0$) parity of $|\Phi_{\xi,\eta}\rangle_d$ as for the initial detector state $|00\rangle_d$. With the Kronecker symbol $\delta_{\beta,\alpha}$ $(\alpha = x, y, z)$, we obtain

$$H_{\eta=\pm} = \sum_{m=n,n+1} s_m J_m \delta_{\beta_m,z}\sigma_m^{\alpha_m} + \eta\sqrt{\Gamma_n\Gamma_{n+1}}(\delta_{\beta_n,x}\delta_{\beta_{n+1},y} + \delta_{\beta_n,y}\delta_{\beta_{n+1},x})\sigma_n^{\alpha_n}\sigma_{n+1}^{\alpha_{n+1}}, \tag{4.9}$$

where the term $\propto \eta$ arises from a Lamb shift contribution. In addition, for $\beta_m \neq z$, quantum jumps — transitions from $|00\rangle_d$ into the odd-parity sector signaled by $\xi = 1$ — are possible, with the respective jump rates given by Eq. (4.7). With the compact notation

$$\delta_{\beta,\perp}^{(c)} = \delta_{\beta,x} + i\delta_{\beta,y}, \quad \delta_{\beta,\perp} = \delta_{\beta,x} + \delta_{\beta,y}, \tag{4.10}$$

the jump operators take the form $(\eta = \pm)$

$$c_\eta = -i\left(\eta\sqrt{\Gamma_n}\delta_{\beta_n,\perp}^{(c)}\sigma_n^{\alpha_n} + \sqrt{\Gamma_{n+1}}\,\delta_{\beta_{n+1},\perp}^{(c)}\sigma_{n+1}^{\alpha_{n+1}}\right). \tag{4.11}$$

From Eq. (4.8), the outcome probabilities can be written as

$$P_{\xi,\eta} = \frac{1}{2}\left(\delta_{\xi,0} + (\delta_{\xi,1} - \delta_{\xi,0})\delta t\,\langle c_\eta^\dagger c_\eta\rangle\right) \tag{4.12}$$

with $\langle c_\eta^\dagger c_\eta\rangle = \langle\Psi(t)|c_\eta^\dagger c_\eta|\Psi(t)\rangle$. From Eq. (4.11), we obtain

$$\langle c_\eta^\dagger c_\eta\rangle = 2\eta\sqrt{\Gamma_n\Gamma_{n+1}}\left(\delta_{\beta_n,x}\delta_{\beta_{n+1},x} + \delta_{\beta_n,y}\delta_{\beta_{n+1},y}\right)Q_{n,n+1}^{\alpha_n,\alpha_{n+1}} + \sum_{m=n,n+1}\Gamma_m\delta_{\beta_m,\perp} \tag{4.13}$$

with the correlation function

$$Q_{n,n'}^{\alpha,\alpha'} = \langle\Psi(t)|\sigma_n^{\alpha}\sigma_{n'}^{\alpha'}|\Psi(t)\rangle. \tag{4.14}$$

The average of the binary quantum jump variable $\xi \in \{0,1\}$ then has a state-independent form,

$$\langle\xi\rangle_{\rm ms} = \sum_{\xi,\eta}\xi P_{\xi,\eta} = \sum_{m=n,n+1}\Gamma_m\delta t\,\delta_{\beta_m,\perp}. \tag{4.15}$$

Since $\langle\xi\rangle_{\rm ms} \propto \delta t$, terms $\propto \xi\delta t$ are beyond the accuracy of the lowest-order expansion in δt and will be neglected throughout. However, the identity $\xi^2 = \xi$ implies that terms involving products of ξ are of order δt and must be retained [26, 31].

From Eq. (4.8), we find that the state change after one time step, $|d\Psi\rangle = |\Psi(t+\delta t)\rangle - |\Psi(t)\rangle$, follows from a jump-type nonlinear stochastic Schrödinger equation as in Eq. (2.20) [25, 26, 31, 100],

$$|d\Psi\rangle \;=\; \left[-i\delta t H_\eta + \xi\left(\frac{c_\eta}{\sqrt{\langle c_\eta^\dagger c_\eta\rangle}} - 1\right) - \frac{\delta t}{2}\left(c_\eta^\dagger c_\eta - \langle c_\eta^\dagger c_\eta\rangle\right)\right]|\Psi(t)\rangle. \tag{4.16}$$

Unless noted otherwise, we assume an easily accessible pure product initial state, say, $|\Psi(0)\rangle = |00\cdots0\rangle$. For given measurement record, the state $|\Psi(t)\rangle$ then always remains pure and follows from Eq. (4.16). Depending on the choice of the steering operators, the quantum state dynamics in Eq. (4.16) includes single- and two-qubit unitary Hamiltonian terms (from H_η), single-qubit Pauli gates (due to quantum jumps for $\xi = 1$), and two-qubit unitary terms (from the last term, which represents state diffusion [31]). In principle, given the set of steering operators in Eq. (4.4), which in turn determine the jump operators c_η and the Hamiltonian H_η, all operations needed for accessing a target state of arbitrary form are therefore contained in Eq. (4.16) [29, 101–103]. We discuss convergence properties of our protocol in Sec. 4.2.4.

One can equivalently describe the state dynamics by using the density matrix, $\rho(t) = |\Psi(t)\rangle\langle\Psi(t)|$. Using Eq. (4.16), the change in one time step, $d\rho = \rho(t+\delta t) - \rho(t)$, is determined by the stochastic master equation [26]

$$d\rho = -i\delta t[H_\eta,\rho] + \xi\left(\frac{c_\eta\rho c_\eta^\dagger}{\langle c_\eta^\dagger c_\eta\rangle} - \rho\right) - \frac{\delta t}{2}\left\{c_\eta^\dagger c_\eta - \langle c_\eta^\dagger c_\eta\rangle, \rho\right\}, \tag{4.17}$$

with the anticommutator $\{\cdot,\cdot\}$. State normalization holds because of $\mathrm{Tr}(d\rho) = 0$. Apart from a unitary evolution term due to H_η, Eq. (4.17) again contains a jump term $\propto \xi$ which can result in large state changes, and a stochastic contribution of diffusion type (the anticommutator).

Averaging Eq. (4.17) over measurement outcomes using the probabilities (4.12) will usually result in a mixed state. The averaged state change, $\langle d\rho\rangle_{\rm ms} = \sum_{\xi,\eta} d\rho_{\xi,\eta}P_{\xi,\eta}$ with $d\rho_{\xi,\eta}$ in

Eq. (4.17), is governed by a Lindblad master equation [25, 26],

$$\langle d\rho\rangle_{\rm ms} \;=\; \delta t \sum_{m=n,n+1} \Big(-is_m J_m \delta_{\beta_m,z}[\sigma_m^{\alpha_m},\rho] + \Gamma_m \delta_{\beta_m,\perp}\mathcal{D}[\sigma_m^{\alpha_m}]\rho\Big), \tag{4.18}$$

with $\mathcal{D}[\sigma_m^{\alpha_m}]\rho = \sigma_m^{\alpha_m}\rho\sigma_m^{\alpha_m} - \rho$. Equation (4.18) corresponds to the time evolution under a blind steering protocol, where measurement outcomes are simply discarded, as discussed in Chapter 3. Since only uncorrelated contributions from qubits n and $n+1$ appear in Eq. (4.18), the averaged state dynamics by itself is not capable of detecting entanglement structures built up in measurement-conditioned state trajectories.

4.2.2 Bloch tensor representation

Given the Pauli form of the steering operators (4.4), it is convenient to employ the rank-N Bloch tensor $R_{\mathcal{S}}$ for representing states. (In quantum information theory, $R_{\mathcal{S}}$ is usually referred to as N-qubit Bloch vector.) To that end, we first define Pauli string operators of length N,

$$\mathcal{S} = \sigma_1^{\mu_1}\sigma_2^{\mu_2}\cdots\sigma_N^{\mu_N}, \quad \mu_j \in \{0,1,2,3\}. \tag{4.19}$$

(We synonymously use the notations $\mu_j = x,y,z$ and $\mu_j = 1,2,3$.) An arbitrary N-qubit state ρ can be written in the form

$$\rho = \frac{1}{2^N}\sum_{\mathcal{S}} R_{\mathcal{S}}\mathcal{S}, \quad R_{\mathcal{S}} = \mathrm{Tr}(\rho\mathcal{S}), \tag{4.20}$$

where the 4^N Bloch tensor coefficients $R_{\mathcal{S}} = R_{\mu_1,\ldots,\mu_N}$ are real-valued (because of $\rho = \rho^\dagger$) and satisfy $R_{0,\ldots,0} = 1$ (because of state normalization). Using a standard tensor product representation in the computational basis ($\sigma_j = 0,1$), a pure state is parametrized by 2^N complex numbers $C_{\sigma_1,\ldots,\sigma_N}$ subject to normalization,

$$|\Psi\rangle = \sum_{\sigma=\{\sigma_1,\ldots,\sigma_N\}} C_\sigma|\sigma\rangle, \qquad |\sigma\rangle = |\sigma_1,\sigma_2,\ldots,\sigma_N\rangle, \tag{4.21}$$

where the Bloch tensor follows as

$$R_{\mathcal{S}} = \sum_{\sigma,\sigma'} C_\sigma^* C_{\sigma'} \prod_{j=1}^{N} \langle\sigma_j|\sigma_j^{\mu_j}|\sigma_j'\rangle. \tag{4.22}$$

For instance, for $|\Psi\rangle = |00\cdots0\rangle$, one finds $R_{\mathcal{S}} = \prod_{j=1}^N(\delta_{\mu_j,0}+\delta_{\mu_j,3})$.

The stochastic master equation (4.17) then determines the measurement-conditioned change of the Bloch tensor in one time step,

$$dR_{\mathcal{S}} = R_{\mathcal{S}}(t+\delta t) - R_{\mathcal{S}}(t) = \mathrm{Tr}(d\rho\,\mathcal{S}), \tag{4.23}$$

see Eq. (B.2) for an explicit expression. Averaging over measurement outcomes, the Lindbladian

form of Eq. (4.18) gives

$$\langle dR_{\mathcal{S}}\rangle_{\rm ms} \;=\; -2\delta t \sum_{m=n,n+1}\sum_{\alpha\neq\alpha_m}\Big(s_m J_m\,\delta_{\beta_m,z}\sum_{\alpha'}\varepsilon_{\alpha_m\alpha\alpha'}+\Gamma_m\delta_{\beta_m,\perp}\Big)\delta_{\mu_m,\alpha}R_{\mathcal{S}}, \qquad (4.24)$$

with the standard Levi-Civita symbol ε.

By taking a partial trace over the Hilbert space pertaining to one (or several) qubits, one obtains the RDM describing the state of the remaining qubits [29, 64]. In many cases, this state is mixed. For the RDM $\rho^{(r)}_{\mathcal{M}}$, one selects an ordered subset of $r<N$ qubits, $\mathcal{M}=\{j_1,j_2,\ldots,j_r\}$ with $1\leq j_1<\cdots<j_r\leq N$, and partially traces over the $N-r$ remaining other qubits. With the complementary set $\mathcal{M}_c$ corresponding to the traced-out qubits, we have $\rho^{(r)}_{\mathcal{M}}=\mathrm{Tr}_{\mathcal{M}_c}\rho$. To proceed, we again use Pauli string operators $\mathcal{S}_{\mathcal{M}}$ as in Eq. (4.19) but keeping only operators $\sigma_j^{\mu_j}$ with $j\in\mathcal{M}$, i.e., operators for traced-out qubits are left out when constructing the length-r string operator $\mathcal{S}_{\mathcal{M}}$ from the original length-N string operator $\mathcal{S}$. Since Pauli matrices are traceless, Eq. (4.20) then yields

$$\rho^{(r)}_{\mathcal{M}}=\frac{1}{2^r}\sum_{\mathcal{S}_{\mathcal{M}}}R^{(r)}_{\mathcal{S}_{\mathcal{M}}}\mathcal{S}_{\mathcal{M}}, \qquad (4.25)$$

where the rank-r Bloch tensor $R^{(r)}_{\mathcal{S}_{\mathcal{M}}}$ follows from the Bloch tensor $R_{\mathcal{S}}$ for the pure state $\rho=|\Psi\rangle\langle\Psi|$ by simply putting $\mu_j=0$ for all traced-out qubits ($j\in\mathcal{M}_c$).

Let us briefly give a few examples. For $N=1$, Eq. (4.20) reproduces the standard Bloch vector representation of a single-qubit state, $\rho=\frac{1}{2}\left(\sigma^0+\mathbf{R}\cdot\boldsymbol{\sigma}\right)$, with the Bloch vector $\mathbf{R}=(R_1,R_2,R_3)^T$ and $\boldsymbol{\sigma}=(\sigma^x,\sigma^y,\sigma^z)$. For $N=2$, Eq. (4.20) involves the 4×4 Bloch matrix R_{μ_1,μ_2} [104]. The entries $R_{\alpha_1,0}$ and R_{0,α_2} with $\alpha_j\in\{1,2,3\}$ determine the Bloch vectors $\mathbf{R}_1$ and $\mathbf{R}_2$ for the single-qubit RDMs $\rho_1^{(1)}$ and $\rho_2^{(1)}$ corresponding to the first and second qubit, respectively. The remaining entries encode the correlator (4.14), $R_{\alpha_1,\alpha_2}=Q_{1,2}^{\alpha_1,\alpha_2}$. For $N=3$, the state is represented by R_{μ_1,μ_2,μ_3}. The Bloch vector $\mathbf{R}_1$ determining the single-qubit RDM for the first qubit, $\rho_1^{(1)}=\mathrm{Tr}_{2,3}\rho$, follows as $\mathbf{R}_1=(R_{1,0,0},R_{2,0,0},R_{3,0,0})^T$, and likewise for other qubits. Similarly, there are three two-qubit RDMs, $\left\{\rho_{12}^{(2)},\rho_{23}^{(2)},\rho_{13}^{(2)}\right\}$. For instance, $\rho_{12}^{(2)}$ — the mixed state of qubits 1 and 2 after tracing over qubit 3 — is represented by $R^{(2)}_{\mu_1,\mu_2}=R_{\mu_1,\mu_2,0}$ according to Eq. (4.25). The matrix elements $R^{(2)}_{\alpha_1,0}$ and $R^{(2)}_{0,\alpha_2}$ encode the Bloch vectors $\mathbf{R}_1$ and $\mathbf{R}_2$, while $R^{(2)}_{\alpha_1,\alpha_2}=Q_{1,2}^{\alpha_1,\alpha_2}$.

In what follows, the Bloch tensor representation of the target state $\rho^f=|\Psi_f\rangle\langle\Psi_f|$ is denoted by $R^f_{\mathcal{S}}$, which also determines the Bloch tensors $R^{(r)f}_{\mathcal{S}_{\mathcal{M}}}$ for the corresponding r-qubit RDMs $\rho^{(r)f}_{\mathcal{M}}$.

4.2.3 Active feedback and cost function

We next discuss the active decision making part of the protocol, where the steering parameters $K=(K_n,K_{n+1})$ used in the next time step are selected. In our protocol, this decision is based on optimizing the expected (i.e., averaged over measurement outcomes) change of a cost function, $\langle dC(K)\rangle_{\rm ms}$, with respect to the steering parameters, see Eq. (4.2). If several K form a set with the

same optimal average cost function gain, we choose K according to a uniform random distribution from this set.

We note in passing that interesting variants of our protocol could be based on other strategies. For instance, one could optimize an entanglement measure such as the entanglement entropy in order to steer states towards a class of highly entangled target states. Grouping N qubits into two subsets A and B, and defining the RDM $\rho_A = \mathrm{Tr}_B \rho(t)$, the entanglement entropy is given by [29]

$$S(t) = -\mathrm{Tr}_A \left(\rho_A \ln \rho_A\right). \tag{4.26}$$

The measurement-conditioned change, $dS = S(t+\delta t) - S(t) = -\mathrm{Tr}_A \left(d\rho_A \ln \rho_A\right)$, then has a nonlinear dependence on ρ. While the use of entanglement measures for active feedback protocols is beyond the scope of this work, we show results for $S(t)$ in Sec. 4.3 in order to illustrate how entanglement is generated (or removed) in the active steering process.

For state preparation, one cost function candidate is the fidelity-based cost function $C_N = 1 - \mathrm{Tr}(\rho\rho^f)$ in Eq. (4.3). For a given steering parameter choice K, the expected cost function change is given by

$$\langle dC_N(K)\rangle_{\mathrm{ms}} = -\mathrm{Tr}(\langle d\rho\rangle_{\mathrm{ms}}\, \rho^f) = -\frac{1}{2^N}\sum_{\mathcal{S}} \langle dR_{\mathcal{S}}\rangle_{\mathrm{ms}}\, R^f_{\mathcal{S}}, \tag{4.27}$$

with $\langle d\rho\rangle_{\mathrm{ms}}$ in Eq. (4.18) and $\langle dR_{\mathcal{S}}\rangle_{\mathrm{ms}}$ in Eq. (4.24). Interestingly, the same quantity can equivalently be expressed in terms of weak values [34].

Weak Value representation

The weak value representation of Eq. (4.27) follows by writing $\langle dC_N(K)\rangle_{\mathrm{ms}} = -\langle\Psi_f|\langle d\rho\rangle_{\mathrm{ms}}|\Psi_f\rangle$ and using Eq. (4.18). Assuming that the time-evolving state $|\Psi\rangle$ is *not* orthogonal to the target state $|\Psi_f\rangle$ (i.e., $C_N < 1$), we find

$$\frac{\langle dC_N(K)\rangle_{\mathrm{ms}}}{1-C_N} = \delta t \sum_{m=n,n+1} \Big[-2s_m J_m \delta_{\beta_m,z}\, \mathrm{Im}(W_{m,\alpha_m}) + \Gamma_m \delta_{\beta_m,\perp}\left(1 - |W_{m,\alpha_m}|^2\right)\Big], \tag{4.28}$$

with complex-valued weak values [34] pertaining to single-qubit Pauli operators,

$$W_{m,\alpha_m} = \frac{\langle\Psi_f|\sigma_m^{\alpha_m}|\Psi\rangle}{\langle\Psi_f|\Psi\rangle}. \tag{4.29}$$

If the target state has been reached, $|\Psi\rangle = e^{i\gamma}|\Psi_f\rangle$, all W_{m,α_m} are real-valued (because $\sigma_m^{\alpha_m}$ is Hermitian) and satisfy $|W_{m,\alpha_m}| \leq 1$. Evidently, Eq. (4.28) then tells us that one cannot find steering parameters that could further improve the average cost function, precisely as expected at convergence. If convergence has not yet been reached, however, successful steering requires that at least one steering configuration K exists such that the cost function can still be improved on average, $\langle dC_N(K)\rangle_{\mathrm{ms}} < 0$. According to Eq. (4.28), if $\mathrm{Im}(W_{m,\alpha_m}) \neq 0$ holds for at least

one choice of (m, α_m), one can satisfy $\langle dC_N(K)\rangle_{\rm ms} < 0$ for the global fidelity cost function by choosing $\beta_m = z$ and $s_m = \mathrm{sgn}[\mathrm{Im}(W_{m,\alpha_m})]$. Since for nearly orthogonal states $|\Psi\rangle$ and $|\Psi_f\rangle$, weak value matrix elements tend to be large ("weak value amplification" [34]), Eq. (4.28) suggests that a particularly large improvement of the cost function can arise in this case.

However, it may happen that *all* possible weak values in Eq. (4.29) are real-valued with $|W_{m,\alpha_m}| \leq 1$ before convergence has been reached, i.e., for $C_N > 0$. Equation (4.28) then predicts $\langle dC_N(K)\rangle_{\rm ms} \geq 0$ for all possible K, and the state trajectory gets stuck in a state where the average cost function cannot be lowered anymore by any steering operator. In what follows, we refer to such states as "trapped states." Active steering protocols based on the global fidelity cost function C_N then encounter a prohibitive roadblock. Remarkably, trapped states are abundant already for just $N = 2$ qubits, and they tend to proliferate with increasing N. For instance, consider a specific $N = 2$ Bell target state

$$|\Psi_f\rangle = |\mathrm{Bell}\rangle = (|00\rangle + |11\rangle)/\sqrt{2}, \tag{4.30}$$

where we can easily show that $|\Psi\rangle = |00\rangle$ is a trapped state. Indeed, for this example, we find $C_2 = 1/2$ and the weak values (4.29) are given by $W_{m,\alpha_m} = \delta_{\alpha_m,z}$. Hence Eq. (4.28) implies $\langle dC_2(K)\rangle_{\rm ms} \geq 0$ for all K.

In general, trapped states form a manifold in Hilbert space whose dimensionality depends on the target state. Let us briefly illustrate this point for a two-parameter class of even-parity target states for $N = 2$,

$$|\Psi_f\rangle = u|00\rangle + e^{i\theta}\sqrt{1-u^2}|11\rangle, \tag{4.31}$$

with real parameters $u \in [0, 1]$ and $\theta \in [0, 2\pi)$. Computing the weak values in Eq. (4.29), we find from Eq. (4.28) that for $u \neq \frac{1}{\sqrt{2}}$, the states

$$|\Psi\rangle = v|00\rangle + e^{i\theta}\sqrt{1-v^2}|11\rangle \tag{4.32}$$

with arbitrary $v \in [0, 1]$ span a one-dimensional trapped-state manifold. For $u = \frac{1}{\sqrt{2}}$, the dimensionality of the manifold can further increase because trapped states may now also receive contributions from the odd-parity sector.

We conclude that the weak values in Eq. (4.29), evaluated along the time-evolving state trajectory, can provide useful hints about steering protocols. In particular, they are able to diagnose trapped-state manifolds which arise when all accessible weak values are real-valued with $|W_{m,\alpha_m}| \leq 1$.

We note that there is another mechanism which can also invalidate active steering based on the global fidelity cost function. This mechanism arises from the orthogonality catastrophe problem discussed in Sec. 4.1. In fact, for orthogonal states $|\Psi\rangle$ and $|\Psi_f\rangle$, the weak value matrix elements in Eq. (4.29) are ill-defined. However, $\langle dC_N(K)\rangle_{\rm ms}$ in Eq. (4.28) can then be written in

the form

$$\langle dC_N(K)\rangle_{\rm ms} = -\delta t \sum_{m=n,n+1} \Gamma_m \delta_{\beta_m,\perp} |\langle\Psi_f|\sigma_m^{\alpha_m}|\Psi\rangle|^2. \tag{4.33}$$

If all matrix elements $\langle\Psi_f|\sigma_m^{\alpha_m}|\Psi\rangle$ of single Pauli operators vanish, we have $\langle dC_N(K)\rangle_{\rm ms} = 0$ and the steering protocol gets stuck, i.e., $|\Psi\rangle$ is a trapped state. This case is typically encountered for orthogonal many-qubit states.

The above discussion shows that the averaged fidelity-based cost function (4.3) is not able to guarantee the success of active steering protocols because of the presence of trapped states. Such states are either diagnosed by weak values or arise because of the orthogonality catastrophe problem. In addition, the separation of $\langle dC_N(K)\rangle_{\rm ms}$ into single-qubit weak values, see Eq. (4.28), indicates that entanglement structures are not captured. This separation is a consequence of the linearity of C_N in ρ and of the uncorrelated Lindblad dynamics of $\langle d\rho\rangle_{\rm ms}$ in Eq. (4.18). We will now describe how one can resolve this apparent roadblock.

Local cost function terms

In order to enable successful steering under protocols with active feedback, we next include local fidelity contributions in the cost function. To that end, we introduce basis-independent terms which enforce that all RDMs formed from the state $\rho(t)$ will approach the respective RDMs for ρ^f. This strategy is able to resolve the trapped-state problem.

To that end, let us define a local cost function term, $C_r(t)$, for r-qubit RDMs with $r < N$. This term includes contributions from all ordered subsets $\mathcal{M}$ which can be constructed for r qubits, see Sec. 4.2.2. The number of such subsets is given by a binomial coefficient, $N_r = \begin{pmatrix} N \\ r \end{pmatrix}$. Using the squared Frobenius norm (*aka* relative purity) [29] to quantify the distance between the RDM and the corresponding target RDM, we arrive at

$$C_r(t) = \frac{1}{2N_r} \sum_{\mathcal{M}} {\rm Tr}\left(\rho_{\mathcal{M}}^{(r)}(t) - \rho_{\mathcal{M}}^{(r)f}\right)^2. \tag{4.34}$$

This cost function penalizes r-qubit RDMs which deviate from the respective r-qubit RDM of the target state. We observe that for $r = N$, Eq. (4.34) reduces to $C_N(t)$ in Eq. (4.3). Using the Bloch tensor representation (4.25), we obtain

$$C_r(t) = \frac{1}{2^{r+1}N_r} \sum_{\mathcal{M}} \sum_{\mathcal{S}_\mathcal{M}} \left(R_{\mathcal{S}_\mathcal{M}}^{(r)}(t) - R_{\mathcal{S}_\mathcal{M}}^{(r)f}\right)^2, \tag{4.35}$$

where we recall that the Bloch tensors $R_{\mathcal{S}_\mathcal{M}}^{(r)}(t)$ for RDMs follow from the Bloch tensor $R_\mathcal{S}(t)$ for the pure state $\rho(t) = |\Psi(t)\rangle\langle\Psi(t)|$ by setting $\mu_j = 0$ for all traced-out qubits, see Sec. 4.2.2. Given the time-evolving Bloch tensor $R_\mathcal{S}(t)$, it is then straightforward to determine the cost functions $C_r(t)$. It is worth mentioning that one could employ other distance measures instead of the squared Frobenius norm in Eq. (4.34), e.g., the max norm, the trace norm, or a Schatten

p-norm [105]. However, we expect that the corresponding active steering protocols perform with similar efficiency.

Importantly, all cost function terms $C_r(t)$ with $r = 1, \ldots, N$ are non-negative and simultaneously minimized by $C_r = 0$ when the time-evolving state converges to the target state. This scenario is reminiscent of the parent Hamiltonian construction in Ref. [13], where passive steerability of a state was shown to be equivalent to the simultaneous minimization of all local contributions of a parent Hamiltonian. However, our cost function-based approach is more general and does not suffer from the restrictions on steerability discussed in Ref. [13].

We here employ the weighted-sum method [106], that is, we use a single cost function $C(t)$ which takes into account the r-qubit contribution $C_r(t)$ with probability weight p_r,

$$C(t) = \sum_{r=1}^{N} p_r C_r(t), \quad \sum_r p_r = 1. \tag{4.36}$$

This function is minimized, with $C = 0$, by the converged state, $|\Psi\rangle = e^{i\gamma}|\Psi_f\rangle$. The expected cost function change in one time step, $\langle dC(K)\rangle_{\rm ms} = \sum_r p_r \langle dC_r(K)\rangle_{\rm ms}$, see Eq. (4.2), then follows from

$$\langle dC_r(K)\rangle_{\rm ms} = \frac{1}{2^r N_r} \sum_{\mathcal{M},\mathcal{S}_\mathcal{M}} \left[\left(R^{(r)}_{\mathcal{S}_\mathcal{M}} - R^{(r)\,f}_{\mathcal{S}_\mathcal{M}} \right) \langle dR^{(r)}_{\mathcal{S}_\mathcal{M}}\rangle_{\rm ms} + \frac{\left\langle dR^{(r)\,2}_{\mathcal{S}_\mathcal{M}} \right\rangle_{\rm ms}}{2} \right], \tag{4.37}$$

where $\langle dR^{(r)}_{\mathcal{S}_\mathcal{M}}\rangle_{\rm ms}$ follows from Eq. (4.24). We note that for $r = N$, Eq. (4.37) reduces to Eq. (4.27). The term $\left\langle dR^{(r)\,2}_{\mathcal{S}_\mathcal{M}} \right\rangle_{\rm ms}$ is due to the nonlinear state dependence of the cost functions in Eq. (4.34). We provide its explicit form in Eq. (B.6). In fact, $\langle dC_{r<N}(K)\rangle_{\rm ms}$ has a nonlinear dependence on $d\rho$ because $\mathrm{Tr}(\rho^{(r)\,2}_\mathcal{M}) \leq 1$ is possible for RDMs. (For a pure state, $\mathrm{Tr}(\rho^2) = 1$ instead implies that the cost function change is linear in $d\rho$.) Thanks to this nonlinearity, the disentangling character of the averaged Lindblad dynamics in Eq. (4.28) can be avoided.

In practice, the efficiency of the active steering protocol depends on the choice of the probability weights p_r in Eq. (4.36) [106]. Unfortunately, we have not found a simple strategy for determining the optimal weights. Our heuristic choices are described in Sec. 4.3, but future work may be able to achieve a better understanding of this important issue.

4.2.4 Convergence properties

We here address the convergence properties of the protocol discussed above. Even though we do not have a mathematically rigorous proof valid for arbitrary number N of system qubits, the numerical simulation results for $N \leq 6$ in Sec. 4.3 suggest that the protocol does converge for general N. In fact, in our simulations, we never encountered a case where a predesignated target state was out of reach. In addition, the arguments in Sec. 4.2.1 suggest that the scheme does converge since one can, in principle, realize arbitrary sequences of single- and two-qubit gates.

In this section, for the case $N = 2$, we provide analytical arguments indicating that our active steering protocol converges to a predesignated target state of arbitrary form. For the Bell state, these arguments are rigorous. The results below also illustrate how the inclusion of local cost functions resolves the trapped-states problem.

For $N = 2$, it suffices to take into account only steering operators with $\beta \in \{x, z\}$ in Eq. (4.4). We use the Bloch vectors $\mathbf{R}_{1,2}$, with components $R_1^\alpha = R_{\alpha,0}$ and $R_2^\alpha = R_{0,\alpha}$, see Sec. 4.2.2, in order to parameterize the time-evolving system state. Similarly, $\mathbf{R}_{1,2}^f$ with components $R_m^{\alpha\, f}$ describes the target state. The average local cost function change (4.37) for $N = 2$ can be written as

$$\begin{aligned}\langle dC_1\rangle_{\rm ms} &= \frac{\delta t}{2}\sum_{m=1,2}\left(-s_m J_m \delta_{\beta_m,z}(\mathbf{R}_m\times\mathbf{R}_m^f)^{\alpha_m}+\sum_{\alpha\neq\alpha_m}\Gamma_m\delta_{\beta_m,x}R_m^\alpha\, R_m^{\alpha\, f}\right)\\ &\quad -\delta t\delta_{\beta_1,x}\delta_{\beta_2,x}\frac{\Gamma_1\Gamma_2(\Gamma_1+\Gamma_2)X_{\alpha_1,\alpha_2}}{(\Gamma_1+\Gamma_2)^2-4\Gamma_1\Gamma_2R_{\alpha_1,\alpha_2}^2},\\ &\quad X_{\alpha_1,\alpha_2}=\frac{1}{2}(1-R_{\alpha_1,\alpha_2}^2)(\mathbf{R}_1^2+\mathbf{R}_2^2)-(R_1^{\alpha_1})^2-(R_2^{\alpha_2})^2+2R_{\alpha_1,\alpha_2}R_1^{\alpha_1}R_2^{\alpha_2},\end{aligned}\tag{4.38}$$

where we used $Q_{1,2}^{\alpha_1,\alpha_2}=R_{\alpha_1,\alpha_2}$, see Eq. (4.14). Instead of the weak value representation (4.28), it is here more convenient to express the average global fidelity change $\langle dC_2\rangle_{\rm ms}$ in terms of Bloch tensors as well. From Eqs. (4.27) and (4.24), we then obtain the equivalent representation

$$\begin{aligned}\langle dC_2\rangle_{\rm ms} &= \frac{\delta t}{2}\sum_m\Big[-s_mJ_m\delta_{\beta_m,z}\big\{(\mathbf{R}_m\times\mathbf{R}_m^f)^{\alpha_m}+\sum_{\alpha'}(\mathbf{S}_{m;\alpha'}\times\mathbf{S}_{m;\alpha'}^f)^{\alpha_m}\big\}\\ &\quad +\Gamma_m\delta_{\beta_m,x}\sum_{\alpha\neq\alpha_m}\big\{R_m^\alpha\, R_m^{\alpha\, f}+\sum_{\alpha'}S_{m;\alpha'}^\alpha S_{m;\alpha'}^{\alpha\, f}\big\}\Big].\end{aligned}\tag{4.39}$$

For given $m \in \{1, 2\}$ and $\alpha' \in \{x, y, z\}$, the vector $\mathbf{S}_{m;\alpha'}$ is here defined by the components $S_{m=1;\alpha'}^\alpha = R_{\alpha,\alpha'}$ and $S_{m=2;\alpha'}^\alpha = R_{\alpha',\alpha}$. With the probability weight p_1 in Eq. (4.36), the average total cost function change follows as $\langle dC\rangle_{\rm ms} = p_1\langle dC_1\rangle_{\rm ms} + (1-p_1)\langle dC_2\rangle_{\rm ms}$.

Let us first study $|\Psi_f\rangle = |\text{Bell}\rangle$ as target state, see Eq. (4.30), where the Bloch vectors vanish, $\mathbf{R}_{1,2}^f = 0$. (Analogous arguments can be given for the other Bell states.) For $p_1 = 0$ in Eq. (4.36), i.e., without the local fidelity term, a subclass of trapped states is then given by Eq. (4.32) with $\theta = 0$. This class is parametrized by $0 \leq v \leq 1$ with $v \neq \frac{1}{\sqrt{2}}$. Importantly, it is always possible to identify at least one steering operator such that $\langle dC_1\rangle_{\rm ms} < 0$ for these states. As a consequence, the active steering protocol will converge to the Bell state by allowing for a finite weight $p_1 > 0$. To see this, we note that $\mathbf{R}_{1,2}^f = 0$ implies that only the X_{α_1,α_2}-term in Eq. (4.38) can contribute to $\langle dC_1\rangle_{\rm ms}$. Accordingly, one has to choose $\beta_1 = \beta_2 = x$, where we can specify at least one steering parameter set (α_1, α_2) such that $X_{\alpha_1,\alpha_2} > 0$. Indeed, for the states in Eq. (4.32), we find $R_m^{\alpha_m} = (2v^2-1)\delta_{\alpha_m,z}$ and $R_{\alpha_1,\alpha_2} = \delta_{\alpha_1,\alpha_2}\tilde{Q}_{\alpha_1}$, with $\tilde{Q}_x = -\tilde{Q}_y = 2v\sqrt{1-v^2}$ and $\tilde{Q}_z = 1$. From Eq. (4.38), we thus obtain $X_{\alpha_1,\alpha_2} = 0$ for $\alpha_1 = z$ or $\alpha_2 = z$, but $X_{\alpha,\alpha} = (2v^2-1)^4$ for $\alpha \neq z$ and $X_{x,y} = X_{y,x} = (2v^2-1)^2$. One can therefore always lower the total cost function (4.36) until

convergence has been achieved. This convergence proof for the Bell state also illustrates how the inclusion of local cost functions resolves the trapped-states problem and thereby allows for successful active steering.

We observe numerically that the protocol also converges to a predesignated target state $|\Psi_f\rangle$ of arbitrary form, with non-vanishing Bloch vectors $\mathbf{R}_m^f$. In order to rationalize this observation, we first observe that the terms $\sim s_m J_m$ in Eqs. (4.38) and (4.39) imply that one can always lower the cost function by choosing $\beta_m = z$ and a suitable sign s_m unless the Bloch vectors $\mathbf{R}_m$ are parallel (or antiparallel) to $\mathbf{R}_m^f$, respectively. Similarly, the cost function in Eq. (4.39) can be lowered by $\beta_m = z$ terms until the vectors $\mathbf{S}_\alpha \equiv \mathbf{S}_{2;\alpha}$ satisfy the relations

$$\sum_\alpha \mathbf{S}_\alpha \times \mathbf{S}_\alpha^f = 0 \tag{4.40}$$

and (for all pairs $\alpha < \alpha'$)

$$\mathbf{S}_\alpha \cdot \mathbf{S}_{\alpha'}^f = \mathbf{S}_{\alpha'} \cdot \mathbf{S}_\alpha^f. \tag{4.41}$$

In addition, purity of the state, i.e., $\mathrm{Tr}(\rho^2) = \mathrm{Tr}(\rho^{f\,2}) = 1$, implies the relation

$$\sum_m (a_m^2 - 1)(\mathbf{R}_m^f)^2 + \sum_\alpha [(\mathbf{S}_\alpha)^2 - (\mathbf{S}_\alpha^f)^2] = 0, \tag{4.42}$$

where we write $\mathbf{R}_m = a_m \mathbf{R}_m^f$. We can express the solution to Eqs. (4.40) and (4.41) as

$$\begin{aligned}
\mathbf{S}_x &= b_f \mathbf{S}_x^f + b_\times \mathbf{S}_y^f \times \mathbf{S}_z^f + b_{xy} \mathbf{S}_y^f + b_{xz} \mathbf{S}_z^f, \\
\mathbf{S}_y &= b_f \mathbf{S}_y^f + b_\times \mathbf{S}_z^f \times \mathbf{S}_x^f + b_{xy} \mathbf{S}_x^f + b_{yz} \mathbf{S}_z^f, \\
\mathbf{S}_z &= b_f \mathbf{S}_z^f + b_\times \mathbf{S}_x^f \times \mathbf{S}_y^f + b_{xz} \mathbf{S}_x^f + b_{yz} \mathbf{S}_y^f,
\end{aligned} \tag{4.43}$$

where the real coefficients $(b_f, b_\times, b_{xy}, b_{xz}, b_{yz})$ must satisfy Eq. (4.41) and $\mathbf{S}_\alpha$ has to be of pure-state form [104]. We then examine the effects of $\beta_m = x$ steering operators. From the terms aside the X-term in Eq. (4.38), convergence requires $a_m \geq 0$ and for $\alpha \in \{x, y, z\}$ the relations

$$\sum_{\alpha' \neq \alpha} \mathbf{S}_{\alpha'} \cdot \mathbf{S}_{\alpha'}^f \geq 0, \quad \sum_{\alpha'} \left(\mathbf{S}_{\alpha'} \cdot \mathbf{S}_{\alpha'}^f - S_{\alpha'}^\alpha S_{\alpha'}^{\alpha\, f} \right) \geq 0. \tag{4.44}$$

The X-term is important since it is the only term coupling the Bloch vectors and the vectors $\mathbf{S}_\alpha$. A sufficient condition for successful steering arises if the only solution for the above relations is given by $a_m = 1$ and $b_f = 1$, with $b_\times = b_{xy} = b_{xz} = b_{yz} = 0$. The requirement that $\mathbf{S}_\alpha$ must be of the pure-state form (4.43), together with all the above restrictions, suggests that there is essentially no freedom for other solutions besides $\mathbf{S}_\alpha = \mathbf{S}_\alpha^f$. While the above argument is not a convergence proof, it gives further evidence for the fact that our steering protocol does converge for all possible $N = 2$ target states.

4.3 Simulation results

In order to test the active steering protocol introduced above, we have performed numerical simulations of the stochastic Schrödinger equation (4.16). We provide general remarks on our numerical approach in Sec. 4.3.1, followed by a presentation of numerical results for the simplest case $N = 2$ in Sec. 4.3.2. We here mainly focus on the Bell state in Eq. (4.30). In Sec. 4.3.3, we turn to the highly entangled GHZ and W states for N qubits in Eq. (4.1). We begin with the case $N = 3$, and then turn to larger values of N.

4.3.1 General remarks

All cost function terms in Eq. (4.36) as well as the expectation values for the corresponding changes in Eq. (4.37) can be computed from the time-evolving Bloch tensor $R_{\mathcal{S}}(t)$, which in turn follows from Eq. (4.22). For every time step, $[N/2]$ non-overlapping pairs of adjacent qubits are steered, where we scan through all possible steering parameters K for each pair in order to identify the optimal choice giving the largest expectation value of the cost function gain. The steering parameters are taken from the Pauli operators (4.4). Unless noted otherwise, the numerical results shown below were obtained by excluding detector operators of Pauli type $\beta_n = y$ in Eq. (4.4). (However, such terms are helpful when preparing the W state or for product states.) Once the optimal steering parameters have been identified, the quantum measurement is simulated by stochastically determining the measurement outcome (ξ, η) according to the probabilities $P_{\xi,\eta}$ in Eq. (4.12). Subsequently, the quantum state is updated using Eq. (4.16) and the respective detector qubit pair is re-initialized in the product state $|00\rangle_d$ before the next iteration step is launched.

For a given state trajectory, starting from the initial state $|\Psi(0)\rangle = |00\cdots0\rangle$, the steering protocol is terminated once the fidelity $F(t)$ in Eq. (4.3) exceeds a predefined threshold value F^* above which the state is considered converged. The corresponding time t defines the number of time steps $n_t = t/\delta t$ needed for reaching convergence. Of course, this number varies for different measurement-resolved state trajectories. By collecting a histogram from $M \gg 1$ trajectory realizations, we can obtain a numerical estimate for the probability distribution of the step number n_t. This distribution depends on the chosen fidelity threshold F^*. As shown below, we find that the distribution is quite different from a Gaussian distribution and of a typical asymmetric shape. (We have tried to fit our numerical results to commonly used distributions but did not find satisfactory agreement.) For a qualitative description of the simulation results, we characterize the distribution by three indicators, namely (i) the median N_s, (ii) the mode N_m corresponding to the maximum, and (iii) the half-width ΔN defined as the width of the histogram at half-maximum height. All three numbers depend on the fidelity threshold F^*.

Apart from the statistics of the number of iteration cycles needed for achieving convergence, we also show results for the time dependence of the fidelity cost function $C_N(t) = 1 - F^2(t)$, see Eq. (4.3), both on the level of individual state trajectories and for averages taken over

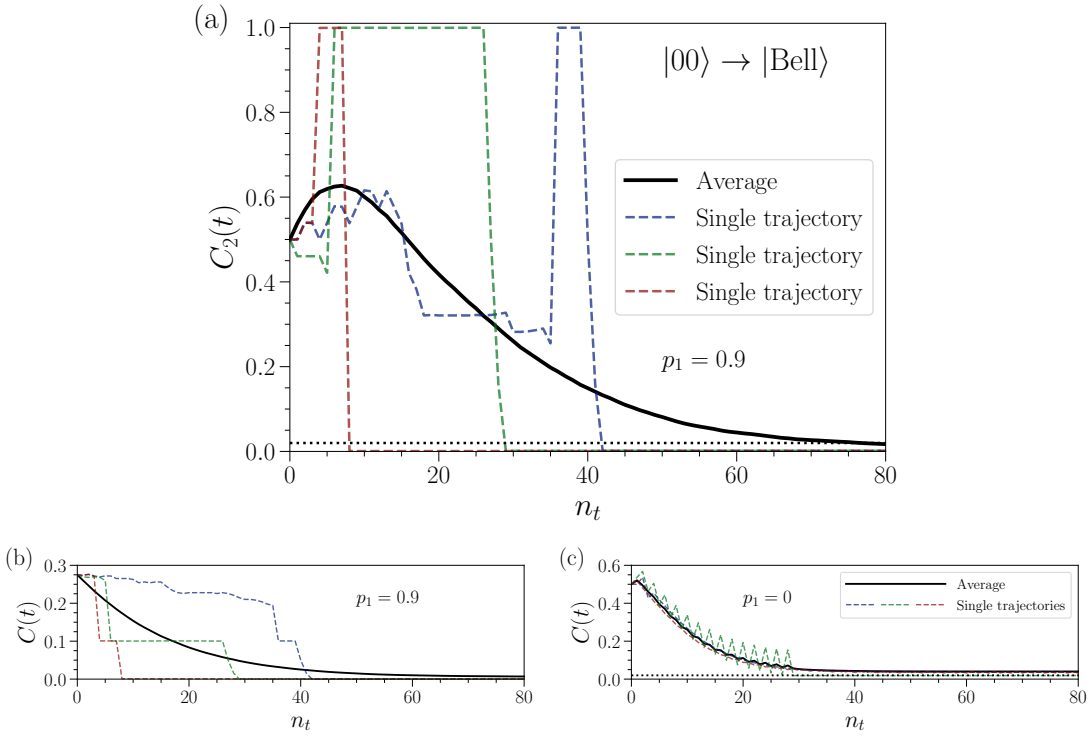

Figure 4.3: Active steering protocol for $N = 2$ qubits and the target state $|\Psi_f\rangle = |\text{Bell}\rangle$ in Eq. (4.30), using the total cost function $C(t)$ in Eq. (4.36) with $p_1 = 1 - p_2 = 0.9$ and target fidelity $F^* = 99\%$. (a) Time evolution of the global fidelity cost function $C_2(t) = 1 - F^2(t)$ vs number of time steps $n_t = t/\delta t$. The colored dashed lines show three measurement-resolved trajectories, the solid black curve is an average over $M = 10^4$ runs. The dotted horizontal line indicates the fidelity threshold value. (b) Corresponding results for the total cost function $C(t)$. (c) Corresponding results for $p_1 = 0$, where $C(t) = C_2(t)$ includes only the global fidelity cost function. For the shown data, our simulations were modified to tolerate a tiny increase in $\langle dC_2(K)\rangle_{\text{ms}}$ in order to still allow for active decision making. Nonetheless, the fidelity threshold is only passed by very few state trajectories, while the great majority of trajectories fails to converge.

many realizations. Similarly, we monitor the time dependence of the total cost function $C(t)$ in Eq. (4.36). Since no steering operations are applied anymore once the fidelity threshold has been passed, the cost functions averaged over multiple trajectories $\overline{C_r(t)}$ can depend on the chosen value of F^* at long times.

Throughout, we assume identical system-detector couplings, $J_n = 1$, and choose $\delta t = 0.2$ as elementary time step such that $\Gamma_n = 0.2$. We have checked that weak asymmetries in the J_n-couplings and/or moderate changes of δt do not cause qualitative changes.

4.3.2 Bell state

We start with the simplest case of $N = 2$ qubits and study the active steering protocol for the target state $|\Psi_f\rangle = |\text{Bell}\rangle$ in Eq. (4.30). Let us recall that all entangled $N = 2$ states are

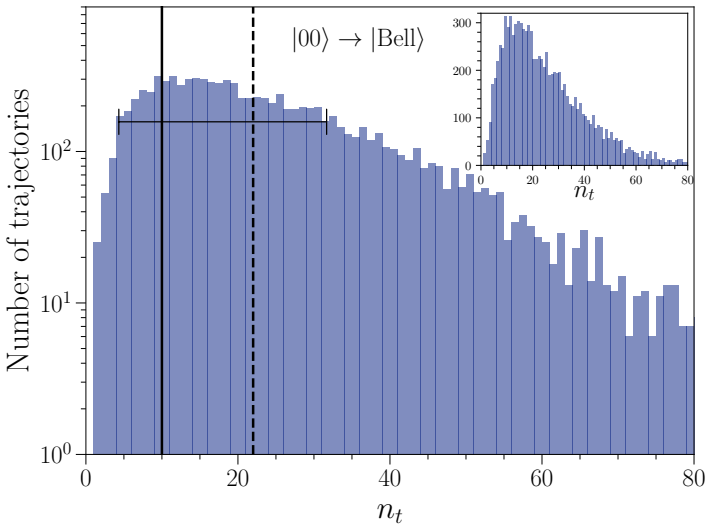

Figure 4.4: Histogram of the number of trajectories that have reached fidelity $F^* = 99\%$ in $n_t = t/\delta t$ time steps, obtained from $M = 10^4$ realizations of the $N = 2$ protocol with $|\Psi_f\rangle = |\text{Bell}\rangle$, see Fig. 4.3. Note the logarithmic scale for the vertical axis. The solid vertical line (horizontal bar) indicates the mode N_m (half-width ΔN), the dashed vertical line shows the median N_s. Inset: Same results but with a linear scale for the vertical axis.

equivalent under local operations and classical communication (LOCC) to $|\text{Bell}\rangle$ [107]. In fact, we have numerically tested for many examples that other $N = 2$ target states can be reached with similar efficiency by our protocol. For several measurement-resolved state trajectories and for an average taken over $M = 10^4$ runs of the protocol, Fig. 4.3(a) shows the time evolution of $C_2(t) = 1 - F^2(t)$. Similarly, Fig. 4.3(b) shows the total cost function $C(t)$ in Eq. (4.36). We here used the probability weights $p_1 = 0.9$ and $p_2 = 0.1$ for the r-qubit cost function terms in Eq. (4.36), but simulation results are qualitatively similar for all $p_1 \gtrsim 0.5$ (with $p_2 = 1 - p_1$). While the analytical argument given at the end of Sec. 4.2.3 suggests that the trapped-states problem can be resolved for any $p_1 > 0$, we find that in practice, for small p_1, the protocol becomes inefficient.

We observe that the individual state trajectories in Fig. 4.3 are characterized by strong fluctuations and large quantum-jump-induced steps in the global fidelity $F(t)$. Typically, the steering protocol $|\Psi(0)\rangle \to |\Psi_f\rangle$ does *not* result in a monotonically increasing time dependence of the fidelity at the level of individual trajectories. Figure 4.3(a) shows that the protocol instead first steers the system into one of the other Bell states, which is orthogonal to the target state ($F = 0$), but then just one additional quantum jump is enough to bring the system to the target state. By allowing for a decrease of the global fidelity $F(t)$ at intermediate times, the protocol is thereby able to allow for fast and efficient active steering. Such state trajectories are easily found and implemented by our protocol because of the presence of the local cost function $C_1(t)$, see Sec. 4.2.3. It is worth emphasizing that, in our case, most state trajectories reach the target state with almost perfect fidelity, well above the fidelity threshold F^* used in Fig. 4.3. We

note in passing that the active decision framework of Ref. [18] is consistent with this scenario. However, a crucial difference is that Ref. [18] considers steering operators pertaining to passive steering protocols, where the active-decision policy only accelerates the steering. In the present protocol, active steering based on global and local cost functions instead allows one to "steer the unsteerable", i.e., to engineer passively unsteerable target states.

At the same time, the total cost function $C(t)$ is observed to monotonically decrease at the level of individual trajectories, see Fig. 4.3(b), even though $C(t)$ could in principle increase after an "unfavorable" measurement outcome. In fact, our protocol only enforces a decrease of the *average* cost function $\langle C(t)\rangle_{\rm ms}$, which must be a monotonically decreasing function for $M \to \infty$. Similarly, after an initial transient behavior, the squared global fidelity averaged over trajectories, $\overline{F^2(t)} = 1 - \overline{C_2(t)}$, increases monotonically, where we find an approximately exponential time dependence for approaching the target state, see Fig. 4.3(a). Interestingly, the slope $\frac{d}{dt}\overline{F^2(t)}$ is larger for short-to-intermediate times than in the long-time limit: states that are nearly orthogonal to the target state tend to be "corrected" more rapidly. This observation is consistent with the weak value amplification mechanism discussed in Sec. 4.2.3.

Next, Fig. 4.3(c) shows the corresponding results obtained from the active steering protocol with $p_1 = 0$, where only the global fidelity cost function is used. In that case, steering is not successful because of the emergence of trapped states, see Sec. 4.2.3. In such cases, state trajectories get stuck before convergence has been reached, and the averaged cost function saturates at some value above the target fidelity threshold. While very few trajectories are still able to pass the fidelity threshold, the scheme is inefficient and fails to converge.

For the fidelity threshold $F^* = 99\%$ and using $M = 10^4$ realizations, Fig. 4.4 shows a histogram of the number of time steps n_t needed for achieving convergence. Evidently, the corresponding distribution function of n_t is asymmetric, quite broad, and rather different from a Gaussian distribution. This fact is particularly evident from the inset of Fig. 4.4, where we use a linear scale for the vertical axis. Using the quantities introduced in Sec. 4.3.1 to characterize the distribution, we find the maximum (mode) $N_m = 10$, the median $N_s = 22$, and the half-width $\Delta N = 28$. Importantly, there are many trajectories which end up in the target state after just a few cycles. On the other hand, we also encounter rare trajectories which require an exceptionally large number of iterations for convergence.

In Fig. 4.5, we study the time evolution of the global fidelity cost function $C_2(t)$ (main panel) and of the total cost function $C(t)$ (inset) if the protocol is run in the opposite direction: we here start from $|\Psi(0)\rangle = |\text{Bell}\rangle$ and steer towards $|\Psi_f\rangle = |00\rangle$. This seemingly trivial task, where entanglement needs to be removed from the system, is much more difficult to realize than the case in Fig. 4.3 using the present formulation of the protocol. In fact, entanglement swapping as employed in our protocol gives efficient ways to inject entanglement into the system, but the removal of entanglement is harder to achieve. Even though we target only the relatively poor fidelity $F^* = 90\%$ in Fig. 4.5, convergence times are now much longer.

From the main panel in Fig. 4.5, we observe that different measurement-resolved trajectories

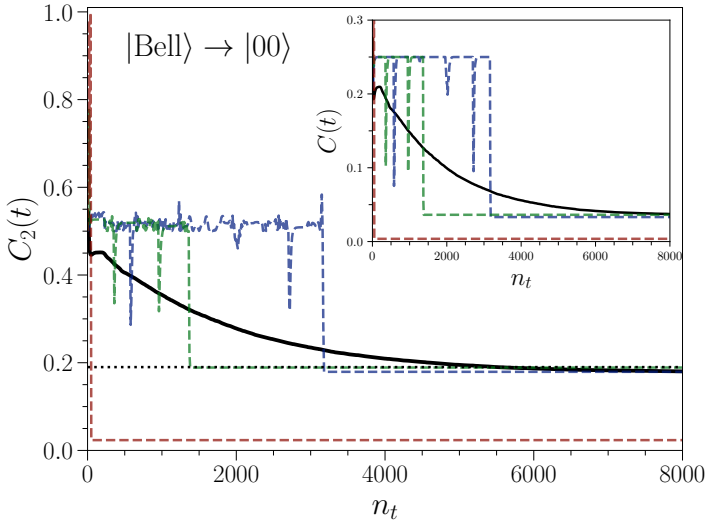

Figure 4.5: Reversed steering protocol for $N = 2$ as in Fig. 4.3 but with interchanged initial and target states, $|\Psi(0)\rangle = |\text{Bell}\rangle$ and $|\Psi_f\rangle = |00\rangle$, using $p_1 = 1 - p_2 = 1$ in Eq. (4.36) and $F^* = 90\%$. The steering operator set includes $\beta_m = y$ terms. Main panel: Time evolution of the global fidelity cost function $C_2(t) = 1 - F^2(t)$ vs number of time steps $n_t = t/\delta t$. Dashed colored curves show individual trajectories, the solid black curve is an average over $M = 10^4$ realizations. The dotted horizontal line indicates the fidelity threshold F^*. Inset: Corresponding results for the total cost function $C(t)$. For $p_1 = 1$, we have $C = C_1$.

surpass the fidelity threshold at widely different times, but they typically do not reach the target state with (almost) perfect fidelity as in Fig. 4.3. One of the shown trajectories passes the fidelity threshold after just 49 steps. Since a finite fraction of all trajectories show such a behavior, we obtain a step-like initial decrease of the fidelity cost function averaged over trajectories $\overline{C_2(t)}$ and of the averaged total cost function $\overline{C(t)}$ at very short times. While individual trajectories sometimes show a sudden increase of $C(t)$ due to unfavorable measurement outcomes, the average $\overline{C(t)}$ decreases monotonically except for a shallow minimum at short times. This minimum is possible because of the finite number M of runs used in computing the average. Since one here typically ends up in states with imperfect fidelity, $F^* < F(t) < 1$, where no steering operations are applied after the corresponding time anymore, $\overline{C(t)}$ and $\overline{C_2(t)}$ show a significant dependence on F^* at long times.

The measurement-resolved trajectories in Fig. 4.5 show that an improvement in the global fidelity is often reversed again in the next step due to unfavorable measurement outcomes. Such a behavior indicates that it is a nontrivial task for our protocol to remove entanglement from the system. However, this task could easily be made highly efficient by adding occasional rounds of single-detector qubit measurements to the active steering protocol. Since our main interest is in the preparation of exotic highly entangled states, however, we do not pursue this extension here. We conclude that, even though less efficient, the protocol is also able to actively steer in the backward direction.

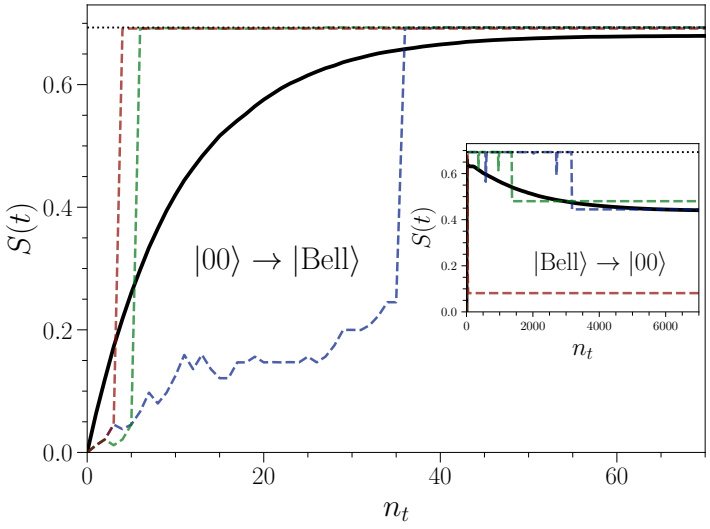

Figure 4.6: Time evolution of the entanglement entropy $S(t)$ for $N = 2$, see Eq. (4.26). Main panel: $S(t)$ vs $n_t = t/\delta t$ for $|\Psi_f\rangle = |\text{Bell}\rangle$ for the same measurement-resolved trajectories as in Fig. 4.3(a). The solid black curve is an average over $M = 10^4$ runs. The dotted horizontal line indicates $S_{\max} = \ln 2$. Inset: Same but for the reversed protocol in Fig. 4.5, where the low fidelity $F^* = 90\%$ implies that $S(t)$ saturates at a relatively large value instead of approaching zero.

The time evolution of the entanglement entropy $S(t)$ in Eq. (4.26) during the above $N = 2$ steering protocols is shown in Fig. 4.6. For the direction $|00\rangle \to |\text{Bell}\rangle$, the main panel of Fig. 4.6 shows $S(t)$ for the same trajectories as in Fig. 4.3(a). We observe that entanglement is quickly built up and one approaches (at long times) the maximal value $S = \ln 2$ expected for $|\text{Bell}\rangle$, see Refs. [54, 108] for related results. In fact, since the trajectory typically cycles through other Bell states before reaching the final target state $|\text{Bell}\rangle$, see Fig. 4.3(a), the convergence of $\overline{S(t)}$ toward $S = \ln 2$ at long times is faster than the corresponding convergence of the fidelity cost function $\overline{C_2(t)}$ shown in Fig. 4.3(a). In the inset of Fig. 4.6, using the trajectories in Fig. 4.5 for the reversed steering direction $|\text{Bell}\rangle \to |00\rangle$, we illustrate that entanglement can also be removed from the system.

In Fig. 4.7, for several target states with $N = 2$ and $N = 3$, we show the mode N_m, the median N_s, and the half-width ΔN as functions of the target fidelity F^*. These three numbers characterize the distribution function of the step number n_t, see Sec. 4.3.1, which in turn is estimated by collecting a histogram. Figure 4.7 indicates that the F^*-dependence of N_m and N_s is very weak for the $|\text{Bell}\rangle$ and $|\text{GHZ}\rangle$ states, while it is approximately exponential for $|\text{W}\rangle$. We note that a steeper increase in $N_s(F^*)$ is observed for the $N = 3$ states in Fig. 4.7 in the limit $F^* \to 1$. This increase can be rationalized by recalling that our termination policy, where one ceases to apply steering operations once a fluctuating state trajectory has passed the fidelity threshold, also affects the long-time limit of averaged cost functions. As a result, an exceptionally large number of steps is needed on average for reaching convergence if the target fidelity is very

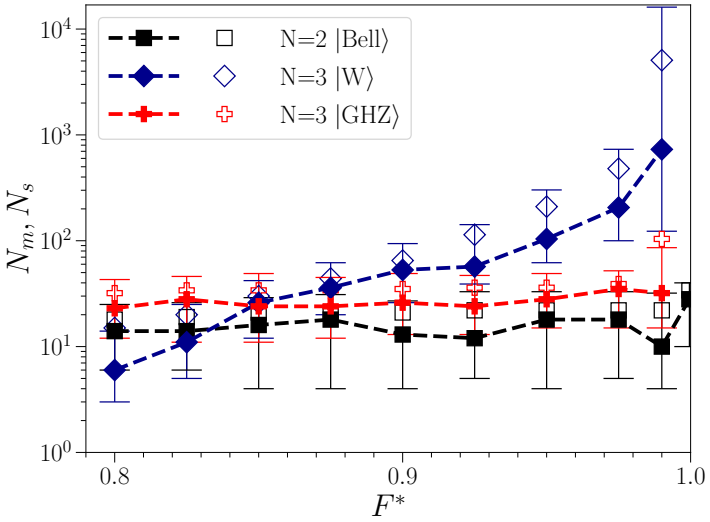

Figure 4.7: Mode N_m (filled symbols), median N_s (open symbols), and half-width (vertical bars) vs target state fidelity F^* for active steering to the $N = 2$ target state $|\text{Bell}\rangle$ and for the maximally entangled $N = 3$ states $|\text{GHZ}\rangle$ and $|\text{W}\rangle$. The shown results have been obtained from $M = 10^4$ trajectories. Note the logarithmic scale for the vertical axis. Dashed lines are a guide to the eye only. For the W state, steering operators with $\beta = y$ in Eq. (4.4) have been included.

close to $F^* = 1$.

4.3.3 W and GHZ states

We next turn to the case $N = 3$, where we consider active steering from $|\Psi(0)\rangle = |000\rangle$ to either $|\Psi_f\rangle = |\text{GHZ}\rangle$ or $|\Psi_f\rangle = |\text{W}\rangle$ in Eq. (4.1). These two states represent different types of maximal tripartite entanglement [52]. However, we have numerically checked that the steering protocol performs with similar efficiency for many other $N = 3$ target states, e.g., with additional phase factors in Eq. (4.1). For all $N = 3$ results shown here, we have used the probability weights $p_1 = 0.9$, $p_2 = 0.09$, and $p_3 = 1 - p_1 - p_2 = 0.01$ for the total cost function in Eq. (4.36). Our protocol is then capable of finding both target states, but one needs a larger number of steps than for $N = 2$.

Results for the time evolution of the cost functions are shown in Fig. 4.8 for the W state, and in Fig. 4.9 for the GHZ state. In both cases, the fidelity threshold is $F^* = 97.5\%$. For these states, the dependence of the mode N_m, of the median N_s, and of the half-width ΔN on the target fidelity F^* are shown in Fig. 4.7. Figure 4.7 indicates that reaching the $|\text{W}\rangle$ state requires more steps than for the $|\text{GHZ}\rangle$ state, especially when asking for high target fidelity F^*. This observation is consistent with the fact that almost all $N = 3$ states with genuine tripartite entanglement are LOCC-related to $|\text{GHZ}\rangle$ [52]. Preparing the much more elusive $|\text{W}\rangle$ state thus is expected to be a challenging task. By comparing the results in Figures 4.8 and 4.9, we observe that the individual trajectories are of different character for both target states. For the GHZ

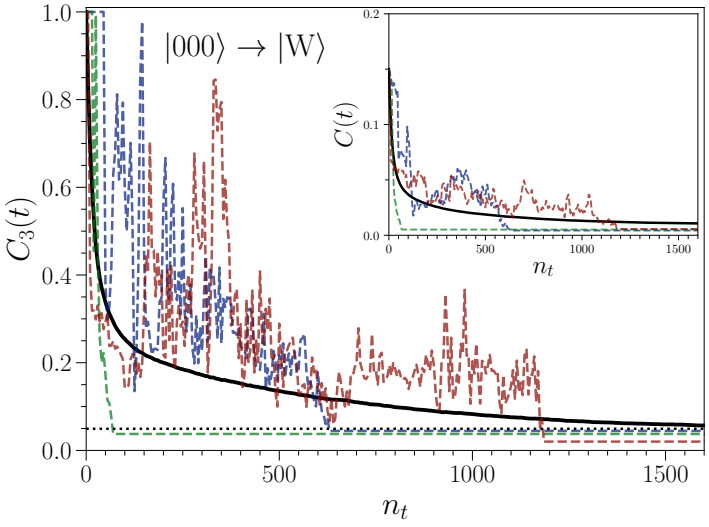

Figure 4.8: Active steering protocol for $N = 3$ qubits and the target state $|\Psi_f\rangle = |\mathrm{W}\rangle$ in Eq. (4.1), with target fidelity $F^* = 97.5\%$. We use the total cost function $C(t)$ in Eq. (4.36) with $p_1 = 0.9$, $p_2 = 0.09$ and $p_3 = 1 - p_1 - p_2 = 0.01$, and include $\beta = y$ steering operators. Main panel: Global fidelity cost function $C_3(t) = 1 - F^2(t)$ vs number of time steps $n_t = t/\delta t$. The dashed colored curves show three measurement-resolved trajectories, the solid black curve is an average over $M = 10^4$ runs. The dotted horizontal line corresponds to the fidelity threshold. Inset: Corresponding results for $C(t)$.

state in Fig. 4.9, we find similar trajectories as for the Bell state in Fig. 4.3: the trajectory cycles through highly entangled intermediate states different from the target state, but then one quantum jump is enough to reach the final target state. For the W state, on the other hand, Fig. 4.8 shows that the fluctuating trajectories are qualitatively different. Typically, jumps to the almost perfect target state (as found for the GHZ state) are much less likely.

This difference is also manifest in a different dependence of N_m and N_s on the target fidelity F^* as shown in Fig. 4.7. While the dependence of N_m and N_s on F^* is exponential for both states, the rate governing the growth of $N_m(F^*)$ and $N_s(F^*)$ is very small for the GHZ state but of significant magnitude for the W state. Similarly, for the target fidelity $F^* = 97.5\%$, the histograms in Fig. 4.10 yield $N_m = 206$ for the W state (blue histogram) but $N_m = 35$ for the GHZ state (green histogram). The GHZ state is therefore much easier to realize. The distribution functions are again found to be broad, asymmetric, with a non-Gaussian shape as observed for the Bell state in Fig. 4.4.

We next apply our active steering protocol to systems with qubit number $N > 3$. The weights p_r in Eq. (4.36) have empirically been chosen as $p_{r+1} = 0.1p_r$ for $1 < r < N - 1$, with $p_1 = 0.9$ and $p_N = 1 - \sum_{r<N} p_r$, but the protocol could probably be made more efficient by a smarter choice for these weights. Since the computational effort for numerical simulations using the present formulation of the protocol scales exponentially in N, we here limit ourselves to $N \leq 6$ qubits and moderate target fidelities F^*. We refer to Sec. 4.4.2 for a discussion of variants of

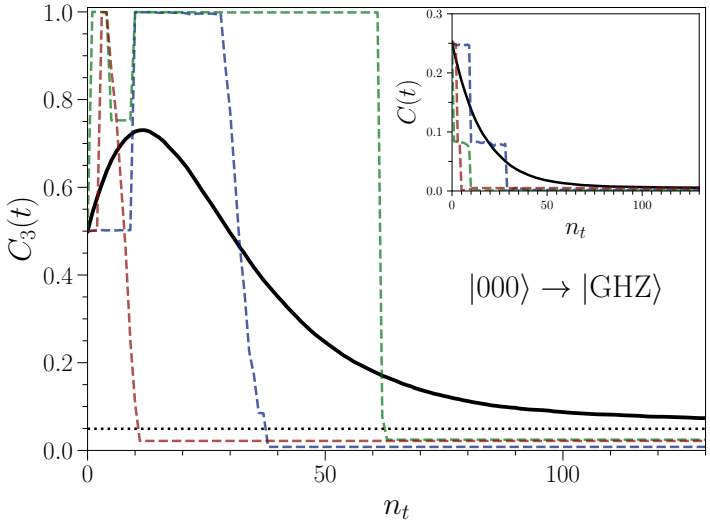

Figure 4.9: Same as Fig. 4.8 but for the target state $|\mathrm{GHZ}\rangle$, again for $F^* = 97.5\%$ and with the same weights p_r. Main panel: Global fidelity cost function $C_3(t) = 1 - F^2(t)$ vs $n_t = t/\delta t$, where dashed colored curves correspond to individual trajectories and the black curve is an average over $M = 10^4$ runs. The dotted horizontal line corresponds to the fidelity threshold. Inset: Corresponding results for the total cost function $C(t)$.

our protocol which should be able to reach large values of N. First, in Fig. 4.11, choosing a rather poor but fixed fidelity threshold $F^* = 80\%$, we explore how N_m, N_s, and ΔN scale with the qubit number N for the highly entangled N-qubit states $|\mathrm{GHZ}\rangle$ and $|\mathrm{W}\rangle$ in Eq. (4.1). We recall that, on general grounds, such states cannot be prepared by physically realizable passive steering protocols [13], see Sec. 4.1. Moreover, while the N-qubit GHZ state could be prepared in a simpler way by projective measurements of suitable stabilizer operators, such a route is not available for the non-stabilizer W state. Figure 4.11 shows that upon increasing N with fixed fidelity threshold, the values of N_m and N_s also increase. Similar to our observations in Fig. 4.7 for the F^*-dependence of these numbers at fixed N, the requirements needed for preparing the W state are more demanding than for the GHZ state.

In Fig. 4.12, we next show the steering dynamics for the $N = 4$ W state, again for selected measurement-resolved trajectories and for the averaged cost functions. The corresponding histogram is shown in Fig. 4.13. On a qualitative level, the steering protocol gives similar results as for the $N = 3$ W state in Figs. 4.8 and 4.10. However, even for the modest fidelity threshold $F^* = 90\%$ used in Figs. 4.12 and 4.13, the mode N_m and median N_s of the distribution are about one order of magnitude larger than what we found for the $N = 3$ W state with $F^* = 97.5\%$, see Figs. 4.8 and 4.10. Finally, in Fig. 4.14, we show the steering dynamics and the corresponding histogram for the $N = 5$ GHZ state. The typical trajectories again feature jump-like steps as for $N = 3$, see Figs. 4.9 and 4.10.

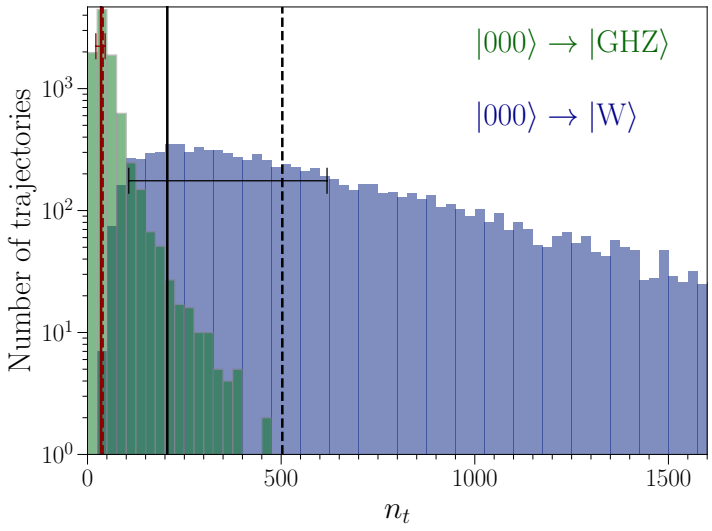

Figure 4.10: Histogram of the number of trajectories that have reached fidelity $F^* = 97.5\%$ in $n_t = t/\delta t$ time steps for the $N = 3$ target states $|\mathrm{W}\rangle$ (blue, see Fig. 4.8) and $|\mathrm{GHZ}\rangle$ (green, see Fig. 4.9). Using a total of $M = 10^4$ runs, each bin shows the corresponding trajectory number accumulated over 25 subsequent time steps. Note the logarithmic scale for the vertical axis. Solid vertical lines (horizontal bars) indicate the respective mode N_m (half-width ΔN), and dashed vertical lines show the median N_s. For the W state, $\beta = y$ steering operators have been included.

4.4 Discussion and outlook

In this section, we summarize our active steering protocol and discuss open points that, in our opinion, deserve to be studied by future work. We begin in Sec. 4.4.1 with several comments on implementation aspects. We then continue in Sec. 4.4.2 with a discussion of the scaling of the protocol with the number N of system qubits. A summary of our key results can be found in Sec. 4.4.3 along with perspectives for future research.

4.4.1 Implementation aspects

While the active steering protocol laid out in Sec. 4.2 is formulated in a platform-independent way, experimental success will depend on the concrete circuit realization. We here discuss several salient points of applied importance for our approach.

First, a key element of our protocol is the ability to efficiently perform Bell measurements of detector qubit pairs. In many platforms, these measurements can be routinely performed by measuring the eigenvalues (syndromes) $\mathcal{O}^{x,z} = \pm 1$ of the detector two-qubit Pauli operators in Eq. (4.5). However, it is still a challenge to perform Bell measurements in some platforms, e.g., in photonic circuits [58, 109]. On the other hand, it is comparatively easy to provide detector qubits in the desired initial state for the photonic platform. We note that one may, in general, use different physical detector qubits during different cycles of the protocol.

It is also important to keep in mind that these projective measurements take a finite time τ_{meas}.

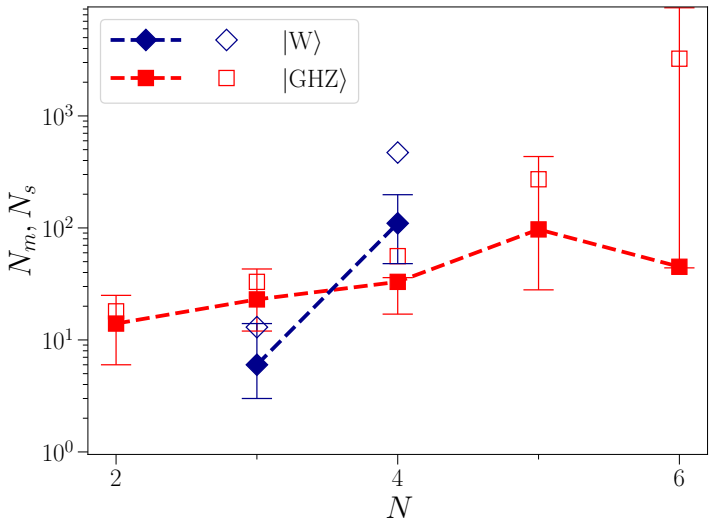

Figure 4.11: Mode N_m (filled symbols), median N_s (open symbols), and half-width (vertical bars) vs qubit number N for active steering to the N-qubit states $|\mathrm{W}\rangle$ and $|\mathrm{GHZ}\rangle$ in Eq. (4.1). Note the logarithmic scale for the vertical axis. For each case, the respective target fidelity is $F^* = 80\%$ and results have been obtained from $M = 10^4$ ($M = 10^3$ for $N = 6$) trajectories. Dashed lines are guides to the eye only. The weights p_r in Eq. (4.36) have been chosen as $p_{r+1} = 0.1p_r$ for $1 < r < N-1$, with $p_1 = 0.9$ and $p_N = 1 - \sum_{r<N} p_r$. For the W state, $\beta = y$ steering operators have been included. For $N = 2$, $|\mathrm{Bell}\rangle$ is identical to $|\mathrm{GHZ}\rangle$ in Eq. (4.1).

In fact, ideal projective measurements (with $\tau_{\mathrm{meas}} \to 0$) come with infinite resource costs [110]. Unless a fault-tolerant platform is available, τ_{meas} should be short compared to the decoherence time of the circuit, as well as to the time scales characterizing the intra-system Hamiltonian evolution. Similar remarks apply to the initial preparation of the detector state $|00\rangle_d$ before every steering cycle. Fast readout and qubit reset techniques (with time scales of order 100 ns) have been reported for superconducting qubit platforms [96, 111]. In addition, for a given physical setup, one may also need to take into account the finite time needed for ramping up (and switching off) the steering operators. However, in a related recent experimental work using superconducting qubits [2], the respective time scales were found to be short compared to τ_{meas}.

Second, let us discuss the basic time scale δt for one iteration cycle of the protocol. On the one hand, δt should not be too short since otherwise the protocol becomes inefficient. On the other hand, δt should be small enough to validate the weak measurement limit and the small-δt expansion of the Kraus operators, see Sec. 4.2.1. Choosing the gate couplings of similar magnitude, $J_n \approx J$, we expect that $J\delta t \sim 0.2$ should work well, cf. Sec. 4.3.

Third, apart from the time scales τ_{meas} and δt, one also needs to account for the finite time τ_{calc} required for the classical calculation performed in parallel to the experimental protocol. In these calculations, $\langle dC(K)\rangle_{\mathrm{ms}}$ is computed for all steering parameter configurations in order to determine the best steering parameter K, and the state $|\Psi(t)\rangle$ is updated after each measurement. For the values of N studied in Sec. 4.3, we find that τ_{calc} is much shorter than the expected

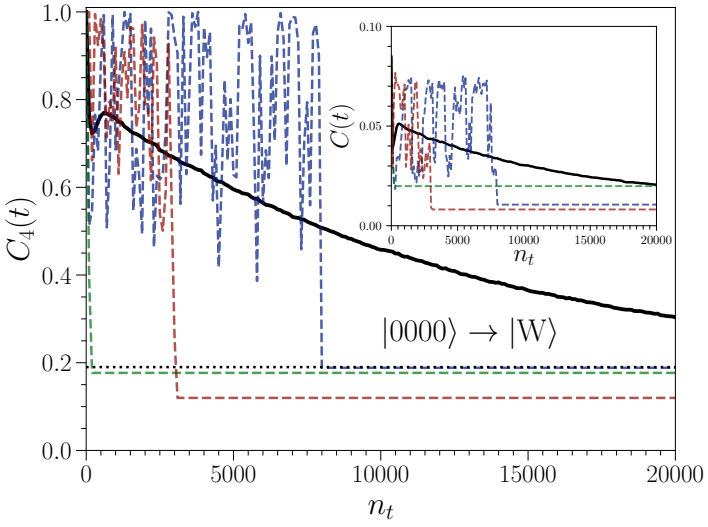

Figure 4.12: Active steering protocol for $N = 4$ qubits and target state $|\Psi_f\rangle = |\mathrm{W}\rangle$ in Eq. (4.1) with target fidelity $F^* = 90\%$, using the total cost function (4.36) with $p_1 = 0.9$, $p_2 = 0.09$, $p_3 = 0.009$, and $p_4 = 1 - p_1 - p_2 - p_3$. We included $\beta = y$ steering operators. Main panel: Global fidelity cost function $C_4(t) = 1 - F^2(t)$ vs number of time steps $n_t = t/\delta t$. The dashed colored curves show three measurement-resolved trajectories, the solid black curve is an average over $M = 10^4$ runs. The dotted horizontal line corresponds to the fidelity threshold. Inset: Corresponding results for the total cost function $C(t)$.

values for τ_{meas}. The classical computation time is thus not expected to impose restrictions.

Fourth, the probably most important practical restriction for our protocol at present comes from our assumption of having a platform free from external noise and/or static errors [32]. In the near future, error-corrected circuits harboring several (say, a dozen) fault-tolerant logical qubits are expected to come into reach [88–97]. Such platforms will represent an ideal playground for our protocols. Without quantum error correction, almost noise-free platforms are available in trapped ion systems [46]. In addition, novel types of noise-protected superconducting qubits [112, 113] may soon realize circuits with strongly reduced noise levels. Similarly, once Majorana qubits become available, very low noise levels are expected due to topological protection mechanisms [11, 12, 114, 115].

Finally, for any implementation, one should verify the ultimate success of the protocol. Such a benchmarking could be performed by using quantum state tomography methods such as shadow tomography [116–118].

4.4.2 Scalability of active decision protocols

In Sec. 4.3, we show explicit numerical simulation results for relatively small qubit number $N \leq 6$ only. Nonetheless, these results constitute a proof of concept that active steering protocols allow for the engineering of passively unsteerable states. Moreover, already for moderate $N \lesssim 10$, the

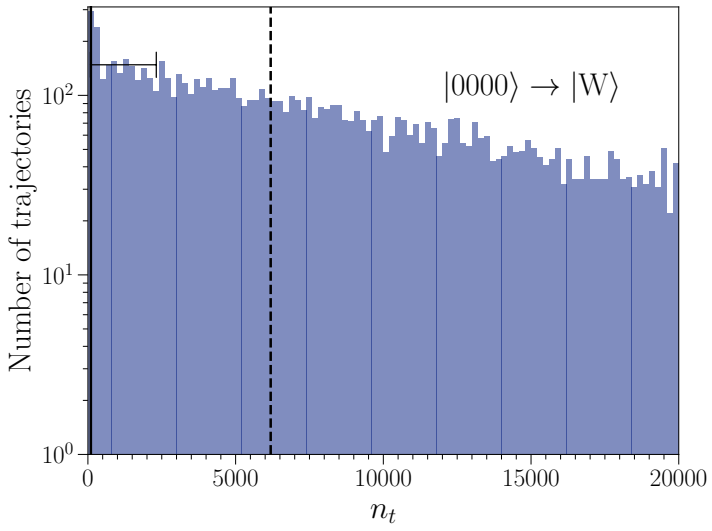

Figure 4.13: Histogram of the number of trajectories that have reached fidelity $F^* = 90\%$ in $n_t = t/\delta t$ time steps from $M = 10^4$ runs for the $N = 4$ target state $|\mathrm{W}\rangle$, see Fig. 4.12. Each bin shows the trajectory number accumulated over 200 subsequent time steps, with a logarithmic scale for the vertical axis. The solid vertical line (horizontal bar) indicates the mode N_m (half-width ΔN), the dashed vertical line shows the median N_s.

preparation of exotic highly entangled states is a very nontrivial task for which active steering provides a fresh perspective. In fact, current experimental efforts on state engineering typically consider quantum hardware with up to ten entangled qubits (rather than large-scale systems), which suffices for typical applications in quantum communication, quantum sensing, or quantum foundational experiments. Our proposal can be readily realized for such systems.

As remarked before, it is not feasible to exactly represent and numerically simulate the time-evolving quantum state trajectories in our active steering protocol on a classical computer for large-scale systems. Since the numerical demands grow exponentially with increasing N, further advances are needed to improve the performance of the protocol for significantly larger N. For instance, with an optimized choice for the probabilities p_r in Eq. (4.36), one may be able to significantly speed up the protocol. Moreover, with suitable modifications, our active feedback strategies could be used for simpler quantum tasks than state preparation. Important examples include adiabatic and non-adiabatic state manipulation, and the realization of entanglement transitions in actively monitored circuits. For such tasks, the protocol becomes much simpler and may enable a study of the large-N limit.

One of the possible routes to scalability of the protocol is multi-block engineering: By employing a variant of our protocol, inspired by Ref. [73], one may consider the local steering of small parts of the system, where one subsequently builds up the full system state by merging different small-N blocks. Since our approach is efficient in actively steering small-N blocks, one may be able to scale to larger system sizes in this manner. While this idea is speculative at

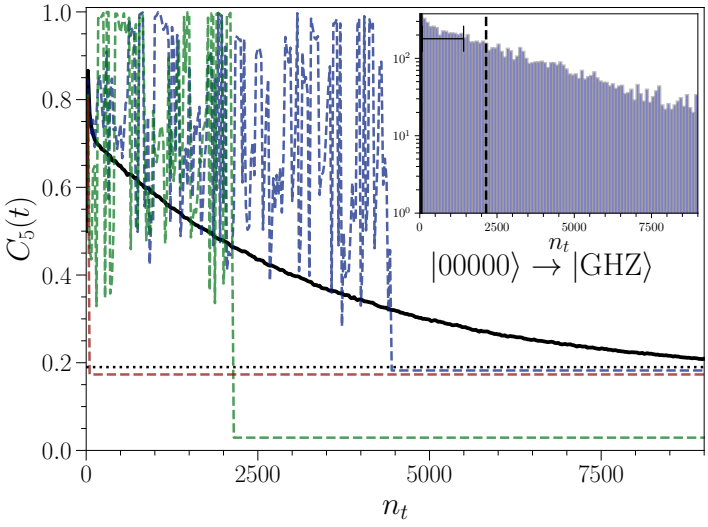

Figure 4.14: Active steering protocol for $N = 5$ qubits and target state $|\Psi_f\rangle = |\mathrm{GHZ}\rangle$ in Eq. (4.1) with target fidelity $F^* = 90\%$, using the total cost function (4.36) with $p_1 = 0.9$, $p_2 = 0.09$, $p_3 = 0.009$, $p_4 = 0.0009$, and $p_5 = 1 - p_1 - p_2 - p_3 - p_4$. Main panel: Global fidelity cost function $C_5(t) = 1 - F^2(t)$ vs number of time steps $n_t = t/\delta t$. The dashed colored curves show three measurement-resolved trajectories, the solid black curve is an average over $M = 10^4$ runs. The dotted horizontal line corresponds to the fidelity threshold. Inset: Corresponding histogram of the number of time steps needed for reaching convergence. Each bin shows the trajectory number accumulated over 100 subsequent time steps, with a logarithmic scale for the vertical axis. The solid vertical line (horizontal bar) indicates the mode N_m (half-width ΔN), the dashed vertical line shows the median N_s.

present, it could eventually obviate the need for expensive classical simulations of a large quantum system.

Furthermore, we expect that the cost functions used in the active decision policy need not be computed exactly in order to achieve state preparation with high fidelity. Indeed, the cost functions in our approach provide (i) an overall "driving bias" for the steering landscape and (ii) a local "potential" to avoid trapped states. Both these main ingredients can, in principle, be simulated approximately. As a consequence, numerical methods for approximately solving quantum problems on classical hardware can be applied, e.g., tensor-network approaches, quantum Monte Carlo simulations, machine learning, or shadow tomography [116, 117]. Such methods often remain efficient for large-scale systems. Adapting them to our protocols and studying the resilience to those approximations are interesting topics for future research.

In Chapter 6 we will use a modification of the protocol presented above, where scalability is achieved by using a different cost function, preparing genuinely entangled states.

4.4.3 Summary and perspectives

We have proposed and tested active steering protocols for quantum state preparation in monitored quantum circuits. In our approach, entanglement is generated in the time-evolving system state $|\Psi(t)\rangle$ by a weak-measurement version of entanglement swapping using Bell measurements of detector qubit pairs. Active decision making strategies then determine the optimal steering operators applied in the next time step. We find that in practice, a limited and realizable set of simple Pauli steering operators is sufficient to warrant convergence of the active steering protocol. We emphasize that we have used a rather restrictive notion of locality in our formulation of the active steering protocol since only Bell measurements between adjacent detector qubits are allowed. Interesting extensions of our protocols could permit a larger spatial coupling range.

A key finding of our analysis is that the standard fidelity is not a useful cost function for active steering to many-body target states. A detailed discussion of this issue can be found in Sec. 4.2.3, where we show that a useful cost function must be able to monitor local substructures of the many-body state. In many cases, those local structures can be efficiently diagnosed by monitoring weak values (which are relatively easy to compute). In other cases, the failure of the fidelity cost function is reminiscent of Anderson's orthogonality catastrophe. We have demonstrated that active steering is possible in practice when including *local fidelity terms* which monitor the r-body reduced density matrices (built from the time-evolving state) in comparison to the corresponding reduced density matrices for the target state. In our present formulation, we constrain all possible local fidelity terms with $1 \leq r \leq N$.

Our numerical simulations reveal that the distribution of the number of time steps n_t needed to reach convergence towards a desired target state is typically far from a Gaussian distribution. (Here, distribution refers to an average taken over many different measurement-resolved trajectories.) The distribution instead is found to be skewed, with a maximum (mode) N_m reached after an only moderate number of steps for small N. We have also characterized the distribution by the median N_s and the half-width ΔN; for a detailed discussion, see Sec. 4.3.

Let us then conclude by describing some perspectives for future research.

State manifolds.— Can active steering protocols converge toward state manifolds instead of a single target state? For example, such a protocol can utilize a cost function maximizing the entanglement entropy (4.26) or other entanglement measures instead of $C(t)$ in Eq. (4.36). The active steering protocol is then expected to target a manifold of maximally entangled states. An interesting open question is to what extent such state manifolds resemble the "dark manifolds" obtained from passive steering [119], where the dark space is a degenerate Lindbladian subspace with eigenvalue zero and the final state depends on the initial state $|\Psi(0)\rangle$. For the active steering case, a different scenario may be that the protocol will continue cycling through all reachable states in the manifold as long as it is evolving in time, independent of the initial state.

We expect that state manifolds may already appear for the cost functions used above. Let us describe three scenarios how this can happen: (i) One may reduce the set of possible steering operators or the number of measurements. In such cases, it is generally not possible anymore

to steer towards an arbitrary target state, and the protocol is likely to reach a state manifold. Because of the drastic simplifications offered by this route, it should also be possible to tackle larger systems. (ii) A similar situation arises if one omits some cost function terms in Eq. (4.36). For instance, by omitting all local fidelity terms with $r < N$, one reaches the trapped-state manifold discussed in Sec. 4.2.3. (iii) One may simultaneously steer towards two non-orthogonal target states $|\Psi_f^{(1)}\rangle$ and $|\Psi_f^{(2)}\rangle$ by adding the respective cost functions weighted with probabilities w_1 and $w_2 = 1 - w_1$. In that case, by varying w_1, we expect that one obtains a manifold of states interpolating between both target states. Since one can systematically study effects of mismatch in the target state, such a protocol could also give useful insights about the impact of errors [32].

State purification.— Within our protocol, if one starts with a pure initial state, the time-evolving state remains pure at all times. With suitable modifications, our protocol could be used for state purification. For instance, one may start from a maximally mixed (infinite temperature) initial state and use the active steering protocol to steer towards an arbitrary, possibly pure, target state. In order to implement this program, one needs to adapt the present formulation of the protocol in order to allow for mixed initial states.

Multipartite entanglement.— One can monitor the increase of multipartite entanglement measures [29] during the protocol. Entanglement structures can be built up very quickly in active steering protocols of the type considered here since limitations imposed by the Lieb-Robinson bound for unitary evolution are absent, see also Ref. [108]. In the present work, we have only studied the entanglement entropy, and we have only considered it for the simplest case of $N = 2$ system qubits.

Memory effects.— Another interesting generalization is to study active steering protocols where instead of the re-initialization of the detector qubit pair in the state $|00\rangle_d$ in each step, one simply takes the previously measured Bell state as new initial state. This scheme is simpler to implement since one avoids the reset of the detector qubits. However, it also introduces memory effects for the state dynamics [120]. At present, it is unclear how this change will affect convergence properties.

Geometrically local fidelity cost functions.— In the present version of the active steering protocol, we take into account all ordered subsets $\mathcal{M}$ of $r < N$ qubits when computing the local cost function $C_r(t)$ in Eq. (4.34). If one truncates the sum over $\mathcal{M}$ in Eq. (4.34) to include only geometrically local sets of nearby qubits, significant simplifications are possible and one is able to study larger system sizes, i.e., larger N. Alternatively, it is also worthwhile to explore whether it suffices to include just the $r = 1$ and $r = 2$ cost function terms on top of the global fidelity term.

Connections to machine learning.— It may be feasible to significantly improve our active steering protocol by employing quantum machine learning methods [19, 121, 122]. Let us briefly speculate about different possibilities. First, machine learning may be useful for optimizing the probability weights p_r appearing in the total cost function (4.36). In the present work, we have simply chosen empirical values for these weights. Second, instead of the exact classical computation of quantum states and the associated cost functions in each step (as done here),

machine learning could offer alternative strategies where such calculations are replaced by faster yet still accurate schemes. Third, in our approach, we start with a known state. In principle, machine learning may be employed in active protocols where the information on the initial state is incomplete. Feeding a neural network with sequences of consecutive readouts, one can perform a partial tomography "on the fly" such that the missing information is reconstructed and the proper cost function can be estimated.

From weak to strong measurements.— Throughout the present work, we have assumed the weak measurement limit, where Kraus operators can be Taylor expanded in $J_n \delta t \ll 1$. On the other hand, for strong system-detector couplings J_n and/or long time steps δt such that $J_n \delta t \sim 1$, one can realize the limit of strong (projective) measurements [26, 29]. Understanding the crossover between the weak and strong measurement regimes in the context of active steering protocols raises an interesting topic for future research. Since the stochastic Schrödinger equation (4.16) does not apply anymore outside the weak measurement limit, one needs to resort to the exact form of the Kraus operators without using the small-δt form. As suggested by the results of Ref. [123], one may accelerate the convergence of our active steering protocol by allowing for larger values of δt. However, we leave this extension to future work.

Noise-resilient schemes.— Ideally, one would like to have active steering protocols that can also tolerate the presence of external noise without requiring a fault-tolerant platform. In the present cost function-based approach, it is difficult to accommodate such effects since state tracking along the time-evolving trajectory is assumed. A conceptually different approach is to target suitable measurement operators and base the active decision making strategy directly on measurement outcomes instead of the evaluation of fidelity cost functions. Such a strategy would be capable of overcoming noise effects since the feedback now directly relies on physically measurable observables. In addition, this approach can, in principle, allow for studying systems in the large-N limit. At present, it is unclear whether such strategies are useful for quantum state preparation, but they certainly can be expected to find other interesting applications.

In the next chapter, we will explore the noise-resilience of the presented steering protocol.

Chapter 5

Error threshold in active steering protocols for few-qubit systems

Building on the general model from Chapter 4, we now introduce environmental error channels during the time evolution. We will reproduce the results from Ref. [23] in a summarized form, showing an appearing threshold depending on the error rate of amplitude damping and dephasing errors. The errors are modeled using Lindbladian dynamics as introduced in Chapter 2. We show results for one and two qubits.

5.1 Introduction

While active steering protocols require one to perform many measurements, which in many presently studied qubit platforms is a quite costly and time-consuming task [124], they also come with important benefits. On the one hand, under fairly general conditions, it is impossible to target certain states, e.g., Green-Horne-Zeilinger (GHZ) states, by driven-dissipative or passive steering protocols [13], while they are accessible to active steering as seen above [22]. We note that for stabilizer states like GHZ states, simpler state preparation schemes are available, see, e.g., Refs. [70, 125, 126]. The results of Ref. [13] do not apply to such routes. Importantly, active steering could also work for non-stabilizer states.

In the present work, however, we focus on small (few-qubit) systems and explore the impact of a finite error rate Γ on active steering. We consider amplitude and/or phase noise, but it is straightforward to add other error channels. The goal of our protocol is to prepare and stabilize, for arbitrarily long times, a predesignated pure target state. Such protocols have previously been studied for circuits with up to $N = 6$ system qubits in the idealized error-free ($\Gamma = 0$) case [22]. A key result of our work is the demonstration of a *sharp error threshold* (characterized, e.g., by a discontinuous derivative with respect to the error strength Γ), present already for just one or two system qubits. The threshold rate, $\Gamma = \Gamma_c$, separates a weak-damping regime ($\Gamma < \Gamma_c$), which realizes a variant of autonomous state stabilization, from a strong-damping regime

($\Gamma > \Gamma_c$) where the target state cannot be reached anymore. The existence of the error threshold is diagnosed using two quantities, namely the fidelity and the purity [127–129] of the late-time state $\overline{\rho}$ averaged over many measurement trajectories. For $\Gamma \ll \Gamma_c$, we obtain nearly perfect fidelity and purity, which then gradually decrease upon increasing Γ. At $\Gamma = \Gamma_c$, we observe a closure of the purity gap [130, 131] and thus have an infinite-temperature state, i.e., a maximally mixed state. Depending on the detailed error channels, for $\Gamma > \Gamma_c$, one either approaches a pure dark state or, if only phase noise is present, one simply remains at the infinite-temperature state.

Our results suggest that active steering can implement autonomous state stabilization as long as the error rate remains sufficiently small. While we study a concrete realization in terms of Andreev qubits, our results are of general nature since we consider a generic model of system and detector qubits coupled by Pauli operators. In order to provide estimates for realistic threshold error rates, we perform numerical simulations for Andreev qubits [132–134] coupled to a photon cavity detector (LC circuit) [124, 135]. Andreev qubits can be encoded by the subgap Andreev bound states (ABSs) in nanoscale superconducting point contacts, as discussed in theoretical [136–142] and experimental [17, 143–153] work. For the Andreev qubit considered below, experiments have already demonstrated coherence times of ~ 500 ns [17], where detector readout times of order 10 ns are possible.

5.2 Active steering in the presence of noise

5.2.1 SME for one and two system qubits

For a single qubit, we consider a protocol where one first initializes the system qubit in a pure state, say, $|\Psi(t=0)\rangle = |+\rangle$ with $\sigma^x|\pm\rangle = \pm|\pm\rangle$, and the detector qubit in the state $|0\rangle_d$. The active steering protocol for preparing and dynamically stabilizing a predesignated target state $|\Psi_f\rangle$, see also Ref. [22], consists of a sequence of finite-time steps of duration δt. Before each time step, one re-initializes the detector qubit in the state $|0\rangle_d$. During a given time step, the system and detector qubits evolve according to a Hamiltonian

$$H = H_s + H_d + H_{sd}, \tag{5.1}$$

where H_s (H_d) acts only on the system (detector) qubit and H_{sd} is a system-detector coupling.

At the end of the time step, one performs a projective measurement of the detector Pauli matrix τ^z, with outcome $\xi = 0$ (if one measures the eigenvalue $+1$ of τ_z) or $\xi = 1$ (if one measures -1).

The Kraus operator A_ξ acts in the Hilbert space of the system qubit, and is given as in the jump-type evolution presented in Section 2.2 with corresponding measurement probabilities P_ξ.

We first define an effective, and in general non-Hermitian, system Hamiltonian $H_{\xi=0,1}$ as

$$H_\xi = H_s\delta_{\xi,0} + {}_d\langle\xi|H_{sd}|0\rangle_d + {}_d\langle\xi|H_d|0\rangle_d. \tag{5.2}$$

We note that for the applications below, the last term in Eq. (5.2) does not contribute. Thus, we obtain the effective Hamiltonian and jump operator according to

$$H_L = H_0, \quad c = -i\sqrt{\delta t}\, H_1. \tag{5.3}$$

One arrives at an SME [22, 26], see Eq. (2.19), where we next include error channels. For that purpose, we use the density matrix $\rho(t)$ of the system qubit since, in general, we now encounter mixed states even for individual measurement trajectories.

For the measurement-conditioned time evolution after one time step, $d\rho_\xi = \rho_\xi(t+\delta t) - \rho$ with $\rho = \rho(t)$, we thereby obtain the canonical SME [26],

$$d\rho_\xi \;=\; -i\delta t\,[H_0,\rho] + \xi\left(\frac{c\rho c^\dagger}{\langle c^\dagger c\rangle} - \rho\right) - \frac{\delta t}{2}\{c^\dagger c - \langle c^\dagger c\rangle, \rho\} + \delta t \sum_\gamma \mathcal{D}[c_\gamma]\rho,$$

where $\{\cdot,\cdot\}$ is the anticommutator and the quantum expectation value of an operator A is $\langle A\rangle = \mathrm{Tr}\,(\rho A)$. The random variable ξ describing the measurement outcome has the *a priori* probabilities,

$$P_{\xi=1} = \delta t \langle c^\dagger c\rangle, \quad P_{\xi=0} = 1 - P_{\xi=1}. \tag{5.4}$$

The sum over the dissipation channels (γ) in Eq. (5.4) contains the dissipator [26], $\mathcal{D}[c]\rho = c\rho c^\dagger - \frac{1}{2}\{c^\dagger c, \rho\}$. For concreteness, we include only two error channels below. However, it is straightforward to add other channels. First, we allow for *amplitude damping* of the system qubit with rate Γ_{AD}. This is described by the jump operator $c_{\mathrm{AD}} = \sqrt{\Gamma_{\mathrm{AD}}}\,\sigma^-$ with $\sigma^- = (\sigma^x - i\sigma^y)/2$ [29]. Second, we include *dephasing* of the system qubit with rate Γ_{PD}, where the jump operator is $c_{\mathrm{PD}} = \sqrt{\frac{\Gamma_{\mathrm{PD}}}{2}}\,\sigma^z$ [29].

We note that Eq. (5.4) tacitly assumes that the measurement time required for performing projective detector measurements is short compared to δt. This assumption may or may not be valid in practice, depending on the platform. Below we give concrete numbers for the case of an Andreev qubit. However, one could refine our analysis by including an extra time interval after each time step, where the measurement dynamics is explicitly considered and the system qubit remains subject to decoherence and dephasing. We leave such generalizations to future work.

Our active steering protocol aims at maximizing a suitable system observable O_s such that the target state is approached over the course of the protocol. For instance, if we wish to prepare the state $|\Psi_f\rangle = |0\rangle$, the observable is chosen as $O_s = \sigma^z$ since the maximal expectation value $\langle O_s\rangle = +1$ is only achieved for the desired target state. While we only assume pure initial states throughout the chapter, it would be straightforward to extend the discussion to an arbitrary initial state, including mixed states. Note that in the case of unitary measurement jump operators, one will not be able to purify the system's state, as discussed below. Taking a fixed system-detector coupling H_{sd}, we assume that, depending on the previous measurement record, one can select one out of seven *steering operators* $H_{s,\alpha}$ (with $\alpha = 1,\ldots,7$) acting on the system qubit during the

following time step. In general, for a given time step, the system Hamiltonian H_s then contains a piece $H_s^{(0)}$, which is always present, and a steering operator $H_{s,\alpha}$ (when choosing the system Hamiltonian for the next step as done here, rather than the system-detector coupling, the active decision making sometimes is referred to as "active shaking" rather than "active steering", cf. [14], where shake-and-steer protocols are discussed),

$$H_s = H_s^{(0)} + H_{s,\alpha}, \quad H_{s,\alpha} \in \{0, \pm J\sigma^x, \pm J\sigma^y, \pm J\sigma^z\}. \tag{5.5}$$

We allow for $H_s^{(0)} \neq 0$ since this term is naturally present in the Andreev qubit application studied below. For the weak measurement limit, the steering operator strength J should satisfy $J\delta t \ll 1$. For simplicity, we assume a fixed constant value for J.

We next describe the active decision making part of the protocol, i.e., how $H_{s,\alpha}$ is chosen for the subsequent time step. After a given time step has been finished with measurement outcome ξ, for every value of α in Eq. (5.5), we compute the measurement-averaged change of the expectation value of the observable O_s anticipated after the following time step,

$$\langle (dO_s)_\alpha \rangle_{\rm ms} = \sum_{\xi=0,1} P_\xi^{(\alpha)} {\rm Tr}\left(d\rho_\xi^{(\alpha)} O_s \right), \tag{5.6}$$

where $\langle O \rangle_{\rm ms}$ indicates an average over measurement outcomes. Here, $d\rho_\xi^{(\alpha)}$ follows from Eq. (5.4) with $H_s = H_s^{(0)} + H_{s,\alpha}$, and the probabilities $P_\xi^{(\alpha)}$ are given in Eq. (5.4). For the next time step, we then select the steering operator (indexed by α) which maximizes Eq. (5.6). In this manner, on average, we effectively also maximize $\langle O_s \rangle$ during the course of the protocol.

The above scheme allows for error channels but requires a classical calculation performed in parallel to the experiment after every time step. As shown by numerical simulations in Sec. 5.3, one approaches the target state (which is the eigenstate for the maximum eigenvalue of O_s) with high fidelity unless error rates become too large.

For two qubits, we again assume that each system qubit only couples to its own detector qubit. The Hamiltonian for $N = 2$ can thus be written as $H = \sum_{n=1,2} H^{(n)}$ with $H^{(n)}$ as in Eq. (5.1). Below, $\boldsymbol{\sigma}_n$ refers to the Pauli matrices for system qubit $n = 1, 2$, and similarly $\boldsymbol{\tau}_n$ for detector qubits. The protocol starts with a pure initial state of the system qubits, say, $|\Psi(0)\rangle = |++\rangle$, and with the state $|00\rangle_d$ for the detector qubits. Before each time step, the detector qubits are re-initialized in this state again.

Weak measurements of the system qubits are performed by projective Bell pair measurements of the two detector qubits, see Chapter 4 for a detailed discussion of this scheme.

One can then construct the SME for the state $\rho(t)$ of the two system qubits in close analogy to the single qubit case, see Eq. (5.4). In analogy to Eq. (5.2), we define the effective system Hamiltonian $H_{\rm eff} = \sum_{n=1,2} H_0^{(n)}$ with

$$H_\xi^{(n)} = \sqrt{2}\ {}_d\langle \Phi_{\xi,\eta} | H^{(n)} | 00 \rangle_d, \tag{5.7}$$

for the nth system qubit. Here Eq. (5.7) is independent of η except for the case $n = 1$ and $\xi = 1$, where we can write $\eta H_1^{(1)}$ for the matrix element. The SME for $d\rho_{\xi,\eta} = \rho_{\xi,\eta}(t + \delta t) - \rho$ conditioned on the measurement outcome follows in almost identical form as in Eq. (5.4),

$$d\rho_{\xi,\eta} \;=\; -i\delta t\,[H_{\rm eff},\rho] + \xi\left(\frac{c_\eta \rho c_\eta^\dagger}{\langle c_\eta^\dagger c_\eta\rangle} - \rho\right) - \frac{\delta t}{2}\{c_\eta^\dagger c_\eta - \langle c_\eta^\dagger c_\eta\rangle, \rho\} + \delta t \sum_\gamma \mathcal{D}[c_\gamma]\rho.$$

The jump operators c_η for outcome $\eta = \pm$ are given by

$$c_\eta = -i\sqrt{\delta t}\left(\eta H_1^{(1)} + H_1^{(2)}\right). \tag{5.8}$$

While the unitary jump operator (5.3) in the single-qubit case considered here does not allow for state purification, the non-unitary jump operators for the two-qubit case in Eq. (5.8) admit this possibility. In fact, for unitary jump operators $c = U$ with $U^\dagger U = 1$ describing measurement effects in the SME, purity is preserved since $\mathrm{Tr}\rho^2 = \mathrm{Tr}(U\rho U^\dagger)^2$. This argument holds as long as one neglects amplitude damping and the interplay with the Hamiltonian dynamics. However, if a quantum jump happens, the dynamics is dominated by the corresponding contribution $\propto \xi$ in Eq. (5.8). We note that while the single-qubit jump operator (5.3) can in general also be non-unitary, for the Andreev qubit application, $(\sigma^s)^2 = 1$ in Eq. (5.15) implies unitarity. The two-qubit case, in contrast, generically comes with non-unitary jump operators. Accordingly, for weak error rates, we find that the active steering protocol generally performs better for $N = 2$ than for $N = 1$ because of the purifying capabilities of the non-unitary $N = 2$ jump operators.

For the SME (5.8), we again introduced dissipation terms such as dephasing and amplitude damping. We assume that those channels separately act on each system qubit $\boldsymbol{\sigma}_{n=1,2}$. The jump operators for dephasing are given by $c_{\rm PD}^{(n)} = \sqrt{\frac{\Gamma_{\rm PD}^{(n)}}{2}}\,\sigma_n^z$, with the corresponding rate $\Gamma_{\rm PD}^{(n)}$. Similarly, for amplitude damping, we have $c_{\rm AD}^{(n)} = \sqrt{\Gamma_{\rm AD}^{(n)}}\,\sigma_n^-$. The summation over γ in Eq. (5.8) includes both the sum over $n = 1, 2$ and over those two error channels. For simplicity, we assume below that the noise strength is identical for each qubit, i.e., $\Gamma_{\rm AD}^{(n=1,2)} = \Gamma_{\rm AD}$ and $\Gamma_{\rm PD}^{(n=1,2)} = \Gamma_{\rm PD}$.

For the active decision making, we proceed as for the single qubit case and maximize the measurement-averaged (anticipated) change of the expectation value of a suitable system observable O_s after the next time step, cf. Eq. (5.6),

$$\langle (dO_s)_\alpha\rangle_{\rm ms} = \sum_{\xi,\eta} P_{\xi,\eta}^{(\alpha)}\,\mathrm{Tr}\left(d\rho_{\xi,\eta}^{(\alpha)}\,O_s\right) \tag{5.9}$$

over the set $\{\alpha\}$ of possible steering operators. In order to target a Bell state, see Eq. (2.27) but now for system qubits, we employ one of the four operators, cf. Eq. (4.5),

$$O_s = \pm\sigma_1^x\sigma_2^x \pm \sigma_1^z\sigma_2^z. \tag{5.10}$$

For instance, by choosing both + signs and maximizing O_s, one targets the symmetric even-parity

Bell state

$$|\Psi_f\rangle = |\Phi_{0,+}\rangle = (|00\rangle + |11\rangle)/\sqrt{2}. \tag{5.11}$$

We here consider the experimentally simplest case, where steering operators only act independently on individual system qubits, cf. Eq. (5.5). We thus assume system Hamiltonians of the form $H_s = \sum_{n=1,2} \left(H_{s,n}^{(0)} + H_{s,\alpha_n} \right)$, where $H_{s,n}^{(0)}$ is given by Eq. (5.12) with $\sigma^z \to \sigma_n^z$ and the index $\alpha = (\alpha_1, \alpha_2)$ now covers $7^2 = 49$ possibilities, cf. Eq. (5.5).

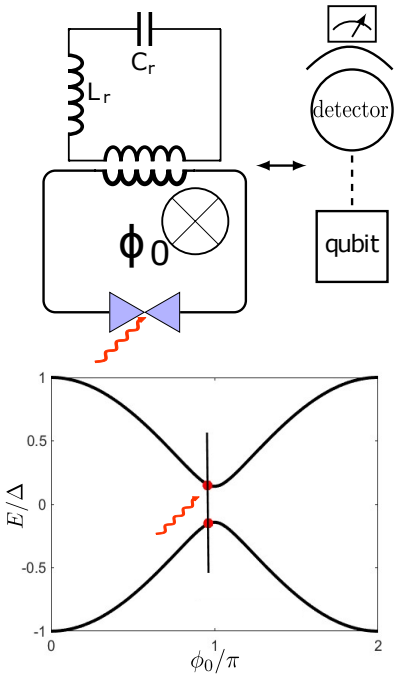

Figure 5.1: Example for the $N = 1$ protocol: The two ABS levels of a phase-biased short nanoscale superconducting junction harbor an Andreev qubit (system qubit), which is coupled to the electromagnetic phase fluctuations of an LC circuit. In a parameter regime allowing for the truncation to only $\xi = 0, 1$ photons in the resonator, the LC circuit serves as detector qubit. Upper panel: The left side shows a sketch of the experimental setup, where the magnetic flux threading a superconducting loop containing the junction imposes the average phase difference ϕ_0 across the junction. The LC circuit is inductively coupled to this loop. The right side shows a schematic of the setup. Red arrows indicate the steering operator $H_{s,\alpha}$, see Eq. (5.5), applied to the point contact, which may induce transitions between system qubit states. Lower panel: ABS dispersion relation $E = \pm E_A(\phi_0)$ (in units of the superconducting gap Δ) vs superconducting phase difference ϕ_0 for transmission probability $\mathcal{T} = 0.98$, see Eq. (5.13). For the implementation of the steering protocol, we fix $\phi_0 = 0.97\pi$ as indicated by red dots.

Application: Andreev qubit

As concrete example for our general approach, we consider an Andreev qubit coupled to an LC resonator operated in the single photon limit, thus acting as an effective detector qubit. The Andreev qubit is realized from the ABS pair in a short nanoscale superconducting point contact

[132–134, 137]. The schematic measurement setup and the ABS dispersion as function of the superconducting phase difference ϕ_0 are shown in Fig. 5.1. For experimental realizations, see Refs. [17, 143–152]. In eigen-energy representation, the system Hamiltonian (without steering operators) is written as

$$H_s^{(0)} = E_A(\phi_0)\,\sigma^z, \tag{5.12}$$

with the positive ABS energy [136, 154–156]

$$E_A(\phi_0) = \Delta\sqrt{1-\mathcal{T}\sin^2(\phi_0/2)}, \tag{5.13}$$

where Δ is the superconducting gap and $\mathcal{T}$ the transmission probability of the contact. The particle-hole partner state is also shown in the lower panel of Fig. 5.1. The Andreev qubit is defined by the ground and excited states according to $|g\rangle = |1\rangle$ and $|e\rangle = |0\rangle$, respectively.

The detector qubit is modeled by an LC circuit with the Hamiltonian $H_d = \Omega a^\dagger a$, where the photon number is constrained to $a^\dagger a \in \{0,1\}$, i.e., we assume that parameters are chosen such that higher photon numbers do not occur with significant weight. Although this condition may be difficult to meet in actual physical implementations of microwave resonators coupled to Andreev qubits [17], we note that our model also describes the coupling of the Andreev qubit to a transmon detector qubit as used in recent experiments [151]. In any case, one can equivalently write H_d (up to an irrelevant energy shift) in qubit language as $H_d = -\Omega\tau^z$, where $|0\rangle_d$ ($|1\rangle_d$) is the state with $\xi = 0$ ($\xi = 1$) photons. The frequency Ω does not influence our protocol since H_d only generates an irrelevant global phase.

Finally, the system and detector qubits are weakly coupled by

$$H_{sd} = \lambda_0 \hat{I}_s \tau^x = \Lambda\,\sigma^s\tau^x, \tag{5.14}$$

with a coupling constant λ_0 and the ABS supercurrent operator $\hat{I}_s = I_0\sigma^s$. Here, σ^s is a rotated Pauli matrix and I_0 denotes the supercurrent scale [137],

$$\begin{aligned} \sigma^s &= \frac{\Delta}{E_A(\phi_0)}\left[-\cos(\phi_0/2)\sigma^z + \sqrt{1-\mathcal{T}}\sin(\phi_0/2)\sigma^y\right], \\ I_0 &= \mathcal{T}\Delta\sin(\phi_0/2). \end{aligned} \tag{5.15}$$

In Eq. (5.14), we have introduced the energy scale $\Lambda = \lambda_0 I_0$ for the system-detector coupling. In the weak measurement limit, $\Lambda\delta t \ll 1$. The steering operators $H_{s,\alpha}$ in Eq. (5.5) could be realized in experiments by means of flux or gate driving pulses along the lines discussed in Ref. [157].

For the results in Sec. 5.3, we assume a transmission probability $\mathcal{T} = 0.98$ and a phase difference $\phi_0 = 0.97\pi$. For $\phi_0 \sim \pi$ and $\mathcal{T}$ close to unity, the Andreev qubit energies $\pm E_A$ in Eq. (5.13) are very small. Since $E_A \ll \Delta$, detrimental transition rates involving above-gap continuum quasiparticles are strongly suppressed and therefore long qubit coherence times are expected [137, 141, 158]. Instead of simply putting $\phi_0 = \pi$ and $\mathcal{T} = 1$, we consider a generic

choice, where the system-detector coupling (5.14) contains σ_y and σ_z.

On the other hand, we assume negligibly short detector readout and detector reset time scales below. (In case one wants to include the effects of those times explicitly, one has to add the uncoupled but noisy evolution of the system qubits during the measurement and reset periods in the SME.) While this assumption is rather unrealistic for transmon qubits, where a readout time ~ 100 ns currently sets the optimal value [135], great progress has been achieved for fast (< 10 ns) dispersive readout of semiconducting quantum dot qubits [159]. Detector reset times are typically much faster [111]. We note that the time step δt of the protocol should be chosen large compared to the measurement (and reset) time of the detector. In fact, the dimensionless parameter $\Delta\delta t$ is limited from both below and from above. The lower limit arises from the measurement (and reset) time and, in numerical computations as presented below, from the fact that otherwise the numerical run-times necessary for converging the protocol towards the steady state become very long. The upper limit instead is imposed by the weak measurement limit assumed in our formulation of the theory. For these reasons, we explore only a relatively narrow window of values for $\Delta\delta t$ in Sec. 5.3 below. However, already for those values, we find indications for "universal" error thresholds.

5.2.2 Numerical solution of the SME

In Sec. 5.3, we present numerical simulation results based on the active steering protocol for $N = 1$ and for $N = 2$, see Sec. 5.2.1. Using the SME in Eq. (5.4), or the one in Eq. (5.8), in the presence of error channels, the measurement-resolved trajectory is described by a mixed state $\rho(t)$ at times $t = j\delta t$ (integer $j > 0$). For an initially pure state $|\Psi(0)\rangle$, however, one can unravel the SME into an equivalent stochastic Schrödinger equation (SSE) [160–164] by resolving pure state trajectories $|\Psi(t)\rangle$ for the measurement dynamics and for the environmental ("bath") stochastic forces which generate the dissipative terms in the SME. In numerical implementations of the SME, it is advantageous to employ the SSE formulation [22, 164, 165]. By averaging the dynamics predicted by the SSE over the stochastic bath variables, one recovers the SME.

We here specify the SSE only for $N = 1$, since the case $N = 2$ follows analogously. Writing $|d\Psi\rangle_{\xi,x_\gamma} = |\Psi(t+\delta t)\rangle_{\xi,x_\gamma} - |\Psi\rangle$ with $|\Psi\rangle = |\Psi(t)\rangle$, one finds [160–164]

$$\begin{aligned} |d\Psi\rangle_{\xi,x_\gamma} &= \left\{ -i\delta t\, H_0 - \frac{\delta t}{2}\left(c^\dagger c - \langle c^\dagger c\rangle\right) + \xi\left(\frac{c}{\sqrt{\langle c^\dagger c\rangle}} - 1\right) + \right. \\ &+ \left. \sum_\gamma \left[\delta t\left(2\langle c_\gamma^\dagger\rangle c_\gamma - c_\gamma^\dagger c_\gamma - \langle c_\gamma^\dagger\rangle\langle c_\gamma\rangle\right) + \sqrt{\delta t}\, x_\gamma\left(c_\gamma - \langle c_\gamma\rangle\right)\right]\right\}|\Psi\rangle, \end{aligned} \tag{5.16}$$

where stochastic bath forces are represented by the normal-distributed random variables $x_\gamma \in \mathcal{N}(0,1)$. These variables are independent of the measurement outcome ξ. Indeed, our numerical analysis confirmed explicitly that ξ and $\{x_\gamma\}$ remain uncorrelated. In contrast to the SME, the SSE (5.16) only evolves pure states and is numerically stable.

An individual measurement-resolved trajectory $\rho(t)$ solving the SME is thereby expressed in terms of an average over $n_w \gg 1$ pure-state trajectories $|\Psi(t)\rangle$ solving the SSE (5.16) for different realizations of the stochastic bath variables $x_\gamma(t)$ (but the same measurement outcomes). The average over $\{x_\gamma(t)\}$ mimics the effect of the corresponding dissipative contributions in the SME. In Sec. 5.3, we choose $n_w = 100$. This value is sufficiently large to ensure convergence to the limit described by the SME without slowing down the numerical simulation too much. We have checked that this value also suffices to describe the largest damping rates discussed in Sec. 5.3. For a detailed discussion of the convergence properties with respect to n_w, see Ref. [164]. On top of the bath average, we may also average over measurement trajectories in order to compute the averaged state $\overline{\rho(t)}$ and/or averaged physical quantities.

5.3 Error threshold

In this section, we present numerical simulation results for the active steering protocols in Sec. 5.2. In Sec. 5.3.1, we study the case of a single Andreev qubit, see Sec. 5.2.1, followed by the two-qubit case in Sec. 5.3.2. For clarity, for $N = 2$, we assume identical parameters for both qubit-detector subsystems and also identical steering couplings ($J_1 = J_2 = J$). In general, we find that our protocol is most efficient and robust if J and the system-detector coupling strength Λ are of comparable magnitude, not differing by more than one order of magnitude. Within these bounds, the detailed choice of these parameters is not important, ensuring the robustness of the protocol. One can rationalize the robustness of the scheme for $J \approx \Lambda$ by noting that the unitary active feedback operations will be inefficient for small J while measurement-based feedback operations become inefficient for small Λ. A good compromise is reached for $J \approx \Lambda$. Below, we either consider equal error rates for amplitude and phase noise, $\Gamma_{\rm AD} = \Gamma_{\rm PD} = \Gamma$, or we study the case of only phase noise with $\Gamma_{\rm AD} = 0$.

5.3.1 One system qubit

Representative numerical simulation results for the time evolution are illustrated in Fig. 5.2, where we show the system state $\overline{\rho(t)}$ averaged over 1000 measurement trajectories. Using the Bloch representation, we write $\overline{\rho(t)} = \frac{1}{2}(\sigma^0 + \mathbf{r}(\mathbf{t}) \cdot \boldsymbol{\sigma})$ with the identity σ^0. In Fig. 5.2, we track the vector $\mathbf{r}(t)$ in the Bloch unit ball, $|\mathbf{r}(t)| \leq 1$, at different time steps. For all panels in Fig. 5.2, we start from $|\Psi(0)\rangle = |+\rangle$ and consider the target state $|\Psi_f\rangle = |0\rangle$, corresponding to $O_s = \sigma_z$ for the active decision making scheme in Sec. 5.2.1. Note that this target state represents an excited state of the Andreev qubit Hamiltonian (5.12). In fact, we find that the active steering protocol approaches an arbitrary predesignated target state with similar convergence rate.

We first study what happens if both amplitude damping and dephasing are present, with $\Gamma_{\rm AD} = \Gamma_{\rm PD} = \Gamma$. For weak damping, see Fig. 5.2(a), the active steering protocol is able to converge the averaged state towards $|\Psi_f\rangle$ with high fidelity, despite of the error channels. We

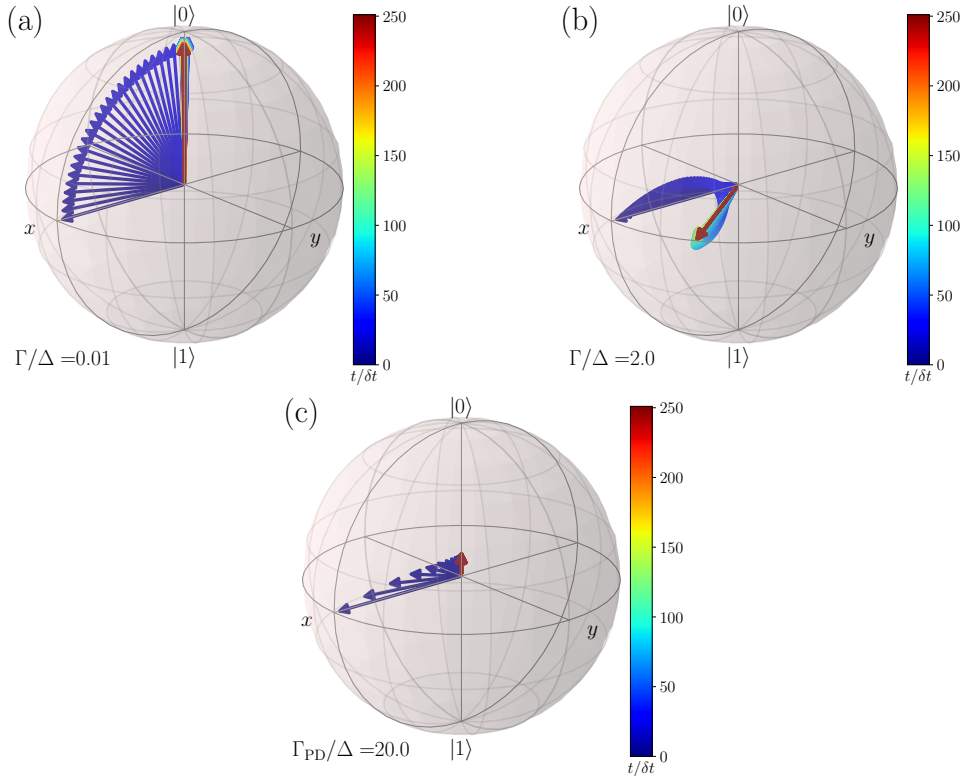

Figure 5.2: Time evolution of the system qubit state $\overline{\rho(t)}$ averaged over 1000 measurement trajectories of the $N = 1$ active steering protocol in the presence of error channels. Starting from $|\Psi(0)\rangle = |+\rangle$, the target state is $|\Psi_f\rangle = |0\rangle$. We show the time evolution of $\overline{\rho(t)}$ in the Bloch unit ball for $\mathcal{T} = 0.98, \phi_0 = 0.97\pi, \Lambda/\Delta = 0.98, J/\Delta = 3, \Delta\delta t = 0.01$, and three choices for the error rates. Color scales correspond to the number of time steps, see the respective color bars. (a) Both amplitude damping and dephasing are present, $\Gamma_{\rm AD} = \Gamma_{\rm PD} = \Gamma$, with $\Gamma/\Delta = 0.01$. (b) Same as panel (a) but for $\Gamma/\Delta = 2$. (c) Only dephasing is present, $\Gamma_{\rm AD} = 0$, with $\Gamma_{\rm PD}/\Delta = 20$.

note that $\overline{\rho(t)}$ always remains approximately pure since the Bloch vector stays near the surface of the Bloch ball.

On the other hand, for strong damping, see Fig. 5.2(b), $\overline{\rho(t)}$ does *not* converge anymore to the desired target state. We observe that $\mathbf{r}(t)$ first leaves the Bloch sphere and enters the interior of the Bloch ball, corresponding to a mixed state. At some time t, an infinite-temperature state with $\mathbf{r}(t) = 0$ is reached. However, the final state $\overline{\rho(\infty)}$ realized at long times is (almost) pure again. This state corresponds to a dark state [119] for the SME in Eq. (5.4). (A dark state is a pure state which is a common zero mode of the entire set of Lindblad operators and an eigenstate of the Hamiltonian.) The long-time dynamics of $\overline{\rho(t)}$ is thus dominated by error channels, and the final state reached by the protocol is basically unrelated to $|\Psi_f\rangle$. For $\Gamma \to \infty$, one would approach the state $|1\rangle$, which is annihilated by the jump operator $c_{\rm AD} \propto \sigma^-$ and also is an eigenstate of $c_{\rm PD} \propto \sigma_z$. However, for the parameters in Fig. 5.2(b), measurement-induced processes are still important and yield a different dark state. In any case, we observe qualitatively distinct regimes

for the dynamics of $\overline{\rho(t)}$ for weak and strong error rates.

Finally, in the absence of amplitude damping, strong phase damping steers the system to a featureless infinite-temperature state, see Fig. 5.2(c). In our case, the Bloch vector $\mathbf{r}(\infty)$ does not precisely vanish because the rate $\Gamma_{\rm PD}$ is not extremely large, and thus measurement-induced processes are still significant. Since the dark space of the Lindbladian for phase damping consists of the z-axis inside the Bloch ball, purity is conserved once this space has been reached. For this reason, $\mathbf{r}(\infty)$ is parallel to the z-axis in Fig. 5.2(c).

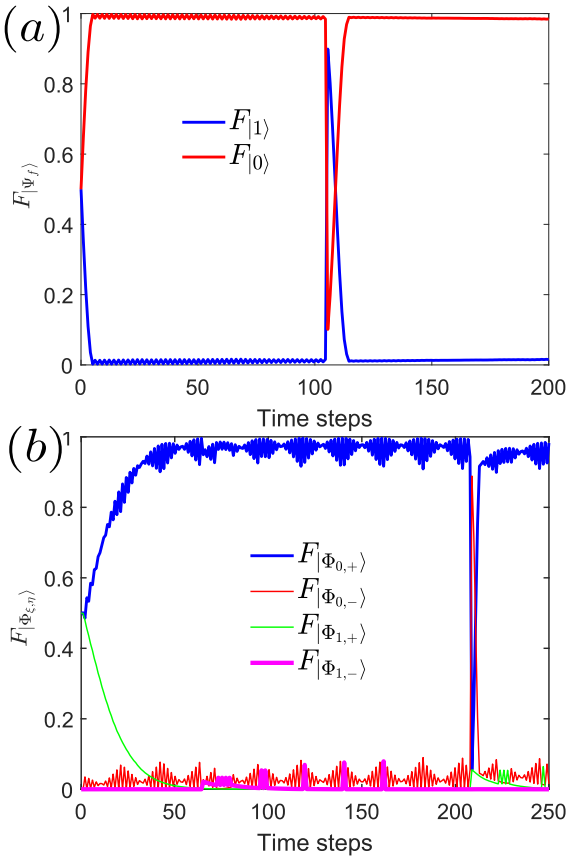

Figure 5.3: Time-dependent fidelities, see Eq. (5.17), obtained from an individual measurement trajectory for $N = 1$ [panel (a)] and $N = 2$ [panel (b)] system qubits under the active steering protocol with error rate $\Gamma/\Delta = 0.001$, where $\Gamma_{\rm AD} = \Gamma_{\rm PD} = \Gamma$. We use the same parameters as in Fig. 5.2 but with $\Delta\delta t = 0.05$. Panel (a): Fidelity vs number of times steps for $N = 1$ with respect to the states $|0\rangle$ and $|1\rangle$, with target state $|\Psi_f\rangle = |0\rangle$. Panel (b): Same as in panel (a) but for $N = 2$. Both system-plus-detector subsystems have identical couplings $\Lambda/\Delta = 0.49$. The initial system state is $|\Psi(0)\rangle = |++\rangle$ and the target state is the symmetric even-parity Bell state $|\Phi_{0,+}\rangle$ in Eq. (5.11). We show the fidelities with respect to each of the four Bell states.

In order to quantify the closeness of the time-evolving system state $\rho(t)$ to the (pure) target state $|\Psi_f\rangle$, a convenient measure is given by the standard fidelity [29],

$$F_{|\Psi_f\rangle}(t) = \langle\Psi_f|\rho(t)|\Psi_f\rangle. \tag{5.17}$$

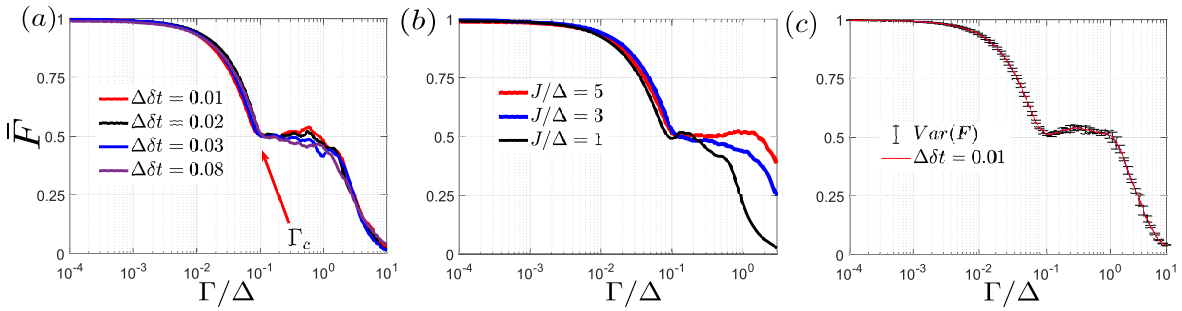

Figure 5.4: Error rate dependence of the fidelity reached at late times of the $N = 1$ steering protocol with $|\Psi(0)\rangle = |+\rangle$ and $|\Psi_f\rangle = |0\rangle$. Both amplitude and phase noise have been included with $\Gamma_{\rm AD} = \Gamma_{\rm PD} = \Gamma$. Note the logarithmic scales for Γ/Δ. We use the same parameters as in Fig. 5.2. Panel (a): Fidelity $\overline{F_{|0\rangle}}$ vs Γ/Δ, averaged over 500 measurement trajectories, for several $\Delta\delta t$. The threshold, $\Gamma_c/\Delta \simeq 0.1$, is marked by an arrow. Panel (b): Same as panel (a) but for $\Delta\delta t = 0.03$ and several J/Δ. Panel (c): Averaged fidelity (red curve) and variance (bars) vs Γ/Δ for $\Delta\delta t = 0.03$. The variance has been computed from 500 trajectories.

This real number is bounded by $0 \leq F(t) \leq 1$, with $F = 1$ only if $\rho(t) = |\Psi_f\rangle\langle\Psi_f|$ is fully converged. When averaged over many measurement trajectories, we denote the averaged fidelity by $\overline{F_{|\Psi_f\rangle}(t)}$. Fig. 5.3(a) shows the time-dependent fidelities $F_{|0\rangle}(t)$ and $F_{|1\rangle}(t)$ for an individual measurement trajectory with $|\Psi(0)\rangle = |+\rangle$ and $|\Psi_f\rangle = |0\rangle$, where the active steering protocol is subject to very weak amplitude and phase damping, $\Gamma_{\rm AD} = \Gamma_{\rm PD} = \Gamma$. We observe that apart from occasional and inevitable quantum jump events, the state is reliably steered towards the desired target state $|0\rangle$. If a quantum jump (with $\xi = 1$) occurs, it comes with a large change in the fidelity. However, the protocol "repairs" this glitch, resulting from an unlikely and unfavorable measurement outcome, quickly by itself again. Our active steering protocol can thus be viewed as an implementation of autonomous state stabilization. In general, our simulation results show that the number of time steps needed for approaching the final state is $\sim (J\delta t)^{-1}$.

For the same $N = 1$ protocol as just discussed, we next turn to the asymptotic long-time value of the averaged fidelity, $\overline{F_{|0\rangle}}$, as a function of the error rate Γ. We again consider the case where both amplitude and phase noise are present. In general, $\overline{F_{|0\rangle}}$ depends on δt for otherwise fixed parameters. (Using Δ as reference energy, the dependence on δt is encoded by the dimensionless parameter $\Delta\delta t$.) However, we observe from Fig. 5.4(a) that results for different δt (approximately) fall onto a single scaling curve when plotting the fidelity as a function of Γ/Δ. The scaling curve is characterized by a sharp threshold error rate Γ_c where a qualitative change happens. For the present parameters, we find $\Gamma_c/\Delta \simeq 0.1$. In order to investigate how this critical value changes when changing physical model parameters for a fixed value of $\Delta\delta t$, Fig. 5.4(b) shows how the curves $\overline{F}$ vs Γ/Δ change when J/Δ is varied. Remarkably, both the threshold value Γ_c and the scaling property are basically unaffected by changing J as long as we are in the regime $J \gtrsim \Lambda$, where steering couplings are significant and the protocol remains efficient. However, the scaling feature of the fidelity now breaks down for strong damping, $\Gamma > \Gamma_c$, where the precise value of

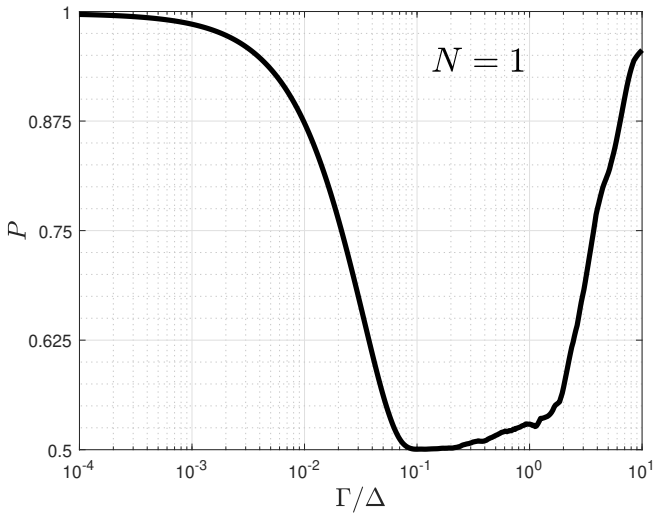

Figure 5.5: Purity P in Eq. (5.18) vs Γ/Δ for $N = 1$, including amplitude and phase damping with $\Gamma_{\rm AD} = \Gamma_{\rm PD} = \Gamma$. Note the logarithmic scales for Γ/Δ. We use the same parameters as well as initial and target states as in Fig. 5.3(a), with $\Delta\delta t = 0.03$ and $\Lambda/\Delta = 0.98$. Averages are over 500 measurement trajectories.

J/Δ matters.

For $\Gamma \ll \Gamma_c$, we conclude that amplitude and phase noise do not harm the active steering protocol. One can still achieve high fidelities, and it is possible to approach and/or stabilize the desired target state with high accuracy. However, with increasing error rate, upon approaching $\Gamma = \Gamma_c$, a qualitative and sudden change in the average fidelity occurs. Apart from the fidelity, this threshold also shows up in other diagnostic measures as detailed below. We note that Fig. 5.4(c) shows the variance of the fidelity (represented by error bars). For $\Gamma \ll \Gamma_c$, the variance is small since basically only the random measurement outcomes cause fidelity variations between different measurement trajectories. As Γ grows, however, also the variance increases since stochastic bath forces now become significant and cause a larger spread.

Next, in Fig. 5.5, we show the purity P of the late-time averaged system state,

$$P = \mathrm{Tr}\left(\overline{\rho(t\to\infty)}^2\right), \tag{5.18}$$

as function of Γ/Δ for $N = 1$. We use the same parameters and the same initial and target states as before. We observe that the fidelity threshold at $\Gamma = \Gamma_c$ in Fig. 5.4 coincides with a *purity gap closing* [130]. For $\Gamma = \Gamma_c$, the asymptotic averaged state is given by the infinite-temperature state, $\overline{\rho} = \frac{1}{2}\sigma^0$, with minimal purity $P = 1/2$. Purity gap closing transitions for mixed density matrices describing ensemble-averaged states have been described within a general theoretical framework in Ref. [130].

On the other hand, one reaches the target state with high purity for $\Gamma \ll \Gamma_c$. In this case, errors remain correctable in our protocol. For $\Gamma > \Gamma_c$, however, the dynamics is dominated by

dissipation channels associated with Γ in Eq. (5.4). We observe that one approaches a pure state again, see also Fig. 5.2(b), where the purity P increases towards its maximum value $P = 1$ as Γ increases. For large Γ, this pure state is linked to the dark state of the dissipative Lindbladian instead of the target state $|\Psi_f\rangle$, which for high amplitude damping and dephasing is given by the ground state $|1\rangle$ of H_s. Remarkably, our numerical simulations show that for $\Gamma \approx \Gamma_c$, the competition between the unitary time evolution due to steering operators and the measurement- and noise-induced dissipative processes results in an infinite-temperature state, where control over the system state is basically lost and the purity gap closes. We note that the error threshold has been discussed above for the ensemble-averaged system, using both the fidelity and the purity as diagnostic measures. For individual measurement trajectories, signatures of the error threshold can also be observed, but these are then subject to random fluctuations, see Fig. 5.4(c).

5.3.2 Two system qubits

We next analyze the case of $N = 2$ system qubits using the protocol described in Sec. 5.2.1, where we assume identical parameters for both system-plus-detector subsystemswith $J_1 = J_2 = J$. In Sec. 5.4, we briefly comment on what happens for asymmetric parameter choices. In principle, we now have $7^2 = 49$ steering operators at hand, see Sec. 5.2.1. For specific tasks, it may be possible to reduce the set of steering operators to a smaller subset that still allows for reaching the desired target state. While we have not explored this option systematically, for setups with $N > 2$, it will be important to determine the minimal set of steering operators in order to obtain efficient protocols.

Again, assuming that both amplitude and phase noise are present, $\Gamma_{\rm AD} = \Gamma_{\rm PD} = \Gamma$, Fig. 5.3(b) shows that for weak error rate Γ, the $N = 2$ protocol is again able to converge the time-evolving state $\rho(t)$ with high fidelity towards a predesignated target state $|\Psi_f\rangle$. In this specific example, we start from the initial state $|\Psi(0)\rangle = |++\rangle$ and steer towards the symmetric Bell target state, $|\Psi_f\rangle = |\Phi_{0,+}\rangle$, see Eq. (5.11). We observe that the protocol is able to retain high fidelity for arbitrarily long times, such that the state is autonomously stabilized. For an individual measurement trajectory, see Fig. 5.3(b), small-amplitude Rabi oscillations can be resolved in the time-dependent fidelity. The frequency of these oscillations corresponds to the energy difference $2E_A$ between the system qubit states, see Eq. (5.13). As for the $N = 1$ case in Fig. 5.3(a), quantum jumps occasionally occur and reduce the fidelity for a very short time span. However, the fidelity recovers quickly to a high value again, demonstrating the robustness of the autonomous state stabilization protocol. In fact, for weak damping, we find that the $N = 2$ protocol is more efficient than its $N = 1$ variant because of the state-purifying capabilities of the non-unitary jump operators for $N = 2$.

For the same $N = 2$ protocol, we show the averaged fidelity reached at late times as function of Γ/Δ in Fig. 5.6(a). Similar to the $N = 1$ case in Fig. 5.4, we again find a sharply defined error threshold, $\Gamma = \Gamma_c$, separating a weak-damping regime ($\Gamma < \Gamma_c$) and a strong-damping regime where steering fails ($\Gamma > \Gamma_c$). The threshold is again accompanied by a closure of the purity gap,

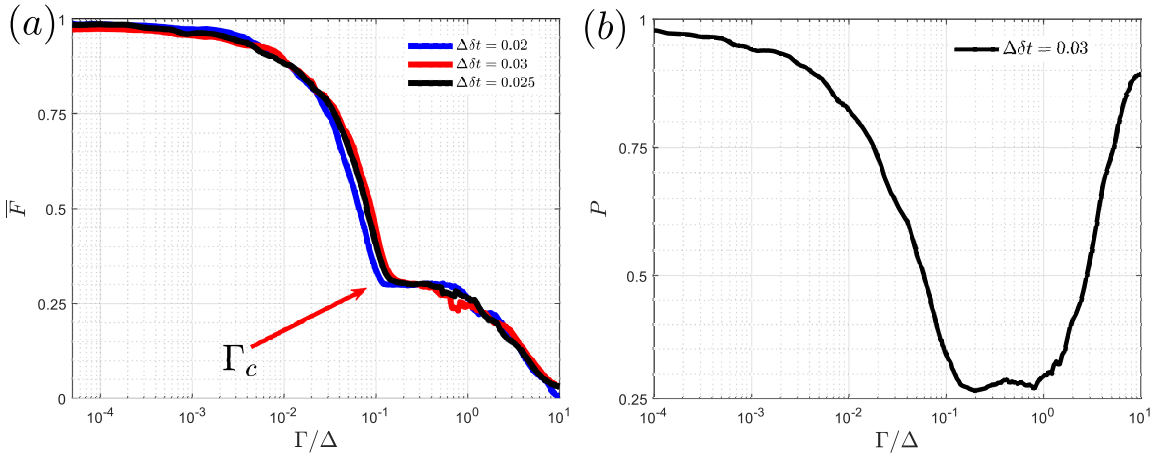

Figure 5.6: Active steering results for $N = 2$ with the same parameters as in Fig. 5.2 for both system-plus-detector subsystems but using $\Lambda/\Delta = 0.49$ and different $\Delta\delta t$. We include both amplitude and phase noise, $\Gamma_{\rm AD} = \Gamma_{\rm PD} = \Gamma$. Note the logarithmic scale for Γ/Δ. Results are averaged over 500 measurement trajectories. Panel (a): Averaged late-time fidelity $\overline{F_{|\Phi_{0,+}\rangle}}$ vs Γ/Δ for $|\Psi(0)\rangle = |++\rangle$ and the Bell target state $|\Psi_f\rangle = |\Phi_{0,+}\rangle$. The threshold value Γ_c is marked by an arrow. Panel (b): Purity P vs Γ/Δ for $\Delta\delta t = 0.03$.

as shown in Fig. 5.6(b). For the considered parameters, the threshold error rate is $\Gamma_c/\Delta \simeq 0.15$. For $\Gamma = \Gamma_c$, we have an infinite-temperature state, $\overline{\rho} = \frac{1}{4}\sigma_1^0\sigma_2^0$, with minimal purity $P = 1/4$. For $\Gamma \ll \Gamma_c$, the averaged state approaches the pure target state $|\Psi_f\rangle$ with high fidelity. By analogy to the QEC case, one may expect that in the limit of large N, the fidelity and the purity approach their ideal values for all $\Gamma < \Gamma_c$. However, for $N = 2$, the fidelity and the purity are gradually degraded upon increasing Γ towards Γ_c. For strong damping $\Gamma \gg \Gamma_c$, on the other hand, one approaches a pure dark state associated with the dissipator $\propto \Gamma$ in Eq. (5.8). As seen in Fig. 5.6(a), the scaling property (i.e., the averaged fidelity depends on Γ/Δ without explicit dependence on δt) holds again.

We next consider the same $N = 2$ protocol but in the presence of only phase noise, $\Gamma_{\rm AD} = 0$ and $\Gamma_{\rm PD} = \Gamma$. The main difference to the previously studied case is that the late-time state reached at large Γ is now the infinite-temperature state. One therefore expects that for $\Gamma > \Gamma_c$, this minimal-purity state persists for all Γ. As shown in Fig. 5.7, this is confirmed by our numerical simulation results. For the parameters in Fig. 5.7, we find $\Gamma_c/\Delta \simeq 0.3$. For $\Gamma > \Gamma_c$, the state is unsteerable and characterized by a very low and approximately constant fidelity (see inset) as well as minimal purity (main panel).

To summarize, the sharp threshold separating a weak-damping regime ($\Gamma < \Gamma_c$, where errors remain correctable) from a strong-damping regime ($\Gamma > \Gamma_c$, where one cannot steer to the desired target state anymore) is also observed in our $N = 2$ simulations. Right at the threshold, the purity gap closes, and one has an infinite-temperature state. For strong damping rates, one in general approaches a pure dark state dominated by the error channels. If only phase noise is

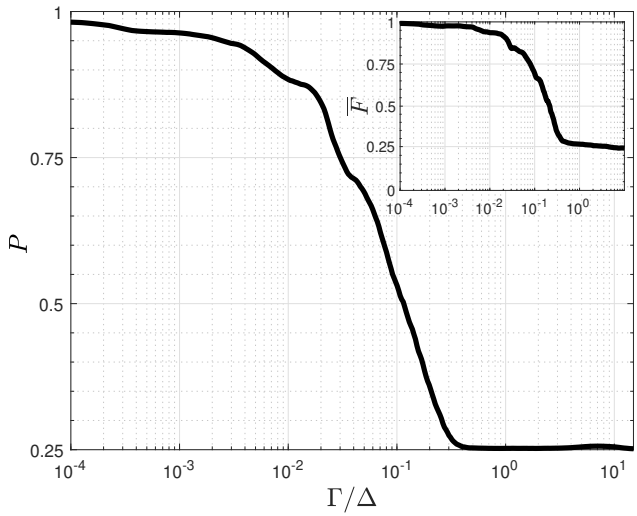

Figure 5.7: Simulation results for the late-time state reached by the $N = 2$ active steering protocol in Fig. 5.6 if only phase noise is present, $\Gamma_{\mathrm{AD}} = 0$ and $\Gamma_{\mathrm{PD}} = \Gamma$. Note the logarithmic scales for Γ/Δ. Averages were taken over 1000 measurement trajectories, using $\Delta\delta t = 0.03$ and $\Lambda/\Delta = 0.49$. Main panel: Purity P vs Γ/Δ, see Eq. (5.18). Inset: Averaged fidelity $\overline{F_{|\Phi_{0,+}\rangle}}$ vs Γ/Δ.

present, one instead finds an infinite-temperature state for all $\Gamma > \Gamma_c$.

5.4 Conclusions and Outlook

In this work, we have formulated active steering protocols in the presence of error channels for few-qubit systems. Our numerical simulations for $N = 1$ and $N = 2$ system qubits reveal a purity gap closing threshold at a specific (non-universal) error rate Γ_c in such an autonomous state stabilization protocol. For $\Gamma \ll \Gamma_c$, the protocol steers the system to the predesignated target state with high fidelity and high purity. For $\Gamma > \Gamma_c$, it is not possible to reach the target state anymore, and for $\Gamma \gg \Gamma_c$, the (undesired) stationary state of the pure error dynamics is instead attained. The competition between the two dynamical resources – active steering and errors – each separately stabilizing a different stationary state, leads to a transition which is found to be sharp, and accompanied by a closure of the purity gap. We expect that such thresholds are likely to appear also in larger-N variants of our protocol. We have presented results for amplitude and phase noise with equal rates, $\Gamma_{\mathrm{AD}} = \Gamma_{\mathrm{PD}}$, and for phase noise only, $\Gamma_{\mathrm{AD}} = 0$. We note in passing that for $\Gamma_{\mathrm{PD}} = 0$, i.e., if only amplitude noise is present, the numerically observed threshold behavior (not shown here) is observed to be qualitatively similar as for $\Gamma_{\mathrm{AD}} = \Gamma_{\mathrm{PD}}$.

It is worth noting that feedback control of a single qubit based on continuous measurements has a long history in quantum optics and quantum information science, see, e.g., Refs. [26, 166, 167]. Similarly, purification protocols for single qubit states are specific examples for such protocols for this type of feedback control, where the measurement basis changes through the

course of the time evolution in order to maximize the state purity. Beyond the single-qubit case, certain multi-qubit entangled states can also be stabilized via feedback based on the measurement of collective system observables, see, e.g., Ref. [168]. In the present case, a weak measurement variant of entanglement swapping has been employed for two system qubits to achieve this goal.

The approach presented here is based on an active steering protocol where error channels are accounted for within the SME. A cost function maximizing the expectation value of a physical observable has been used to guide the measurement trajectory. Since the present formulation requires that one keeps track of the system state, it is not scalable and restricted to relatively small values of N, see also Ref. [22]. The state tracking requirement is a well-known and general obstacle for many state-based feedback schemes. However, for small and very well characterized systems, it may be possible to formulate an active steering protocol only in terms of measurable quantities. In such cases, feedback protocols could avoid state tracking. A detailed study of this interesting question is, however, beyond the scope of this work.

We note that for the $N = 2$ case in Sec. 5.3.2, we have assumed identical parameters for both system-plus-detector subsystems. To ensure that our approach is robust when relaxing this assumption, we have performed additional simulations with parameter asymmetries of order $\sim 3\%$. The corresponding results do not show qualitative differences to the results reported in Sec. 5.3.2, indicating that the purity gap closing threshold transition is robust.

For future work, it would be interesting to study circuits with $N > 2$ qubits, see also Ref. [22]. However, the computational cost of the present scheme grows exponentially with N, both due to the increase in Hilbert space size and in the number of steering operators. On the other hand, the fact that for weak damping, the $N = 2$ scheme is superior to the $N = 1$ approach, together with the option of using a smaller set of steering operators, suggests that one may be able to study systems with, say, $N = 3$ or $N = 4$, with only minor modifications. An important question for future research is to develop scalable variants of our protocol. Once available, one could study if there is a true phase transition associated with the threshold rate Γ_c in the limit $N \to \infty$.

In this work, we have not studied the effects of errors that can induce leakage out of the computational qubit space, e.g., excitations to higher energy levels or quasiparticle poisoning effects. It will be interesting to clarify in future research whether such errors are also associated with a threshold. In Refs. [137, 141], the Andreev state dynamics has been studied, allowing for parity transitions. Incorporating such transitions into our protocol as an additional error channel could be the object of future work. A further intriguing direction aims to generalize the target state from a single state (i.e. a single point on the Bloch sphere) to a two-dimensional state manifold defining a general qubit in order to exhibit control over the whole qubit space. This will provide an active steering variant of quantum error correction protocols [169–171]. Such protocols are not restricted to stabilizer codes.

Chapter 6

Quantum Fisher Information-based protocol

In this chapter, we will reproduce Ref. [24], after a short introduction to the concept of the Quantum Fisher Information. In this publication, building on the protocol presented in Chapter 4, we replace the previously used local cost function in order to target entangled states of many-body systems up to 22 qubits. The reached states form a manifold of genuinely entangled states.

6.1 Quantum Fisher Information

The *Quantum Fisher Information* (QFI) is the quantum version of the classical Fisher Information $F(\lambda)$, which plays a central role in classical parameter estimation. Here, the goal is to determine a certain parameter λ with the lowest possible error, i.e., minimizing the uncertainty $\Delta\lambda$. For this purpose, M independent measurements on a system of interest which is parameterized by λ have to be performed, with measurement outcomes $\zeta = \{\zeta_1, \zeta_2, \ldots, \zeta_M\}$. In this case, the Cramér-Rao lower bound

$$(\Delta\lambda)^2 \geq \frac{1}{MF(\lambda)}, \tag{6.1}$$

gives the fundamentally best precision [26, 172]. Here, the classical Fisher Information is defined as [26]

$$F(\lambda) = \int \mathrm{d}\zeta P(\zeta|\lambda) \left(\frac{\partial \ln P(\zeta|\lambda)}{\partial \lambda} \right)^2, \tag{6.2}$$

where $P(\zeta|\lambda) = \prod_{i=1}^{M} P(\zeta_i|\lambda)$.

As we saw in Chapter 2, in quantum mechanics, generalized measurements can be described by the POVM formalism. We consider a POVM $\{\Pi_\zeta\}$ so that $P(\zeta_i|\lambda) = \mathrm{Tr}(\Pi_{\zeta_i}\rho_\lambda)$ with the quantum mechanical state ρ_λ being parametrized by λ. The QFI is now defined by maximizing the Fisher information over all these possible measurements, giving

$$F_Q(\rho_\lambda) = \max_\Pi F(\lambda), \tag{6.3}$$

and we obtain the quantum Cramér-Rao bound by replacing the classical Fisher information with the QFI [7, 172]. Therefore, we obtain an improved bound.

If the parametrized state ρ_λ can be written as $\rho_\lambda = e^{i\lambda\mathcal{O}}\rho e^{-i\lambda\mathcal{O}}$ with a Hermitian *observable* $\mathcal{O}$, which is the case, e.g., for standard time-evolution, the QFI takes the simpler form

$$F_Q(\mathcal{O},\rho) = 2\sum_{\alpha\beta}\frac{(p_\alpha - p_\beta)^2}{p_\alpha + p_\beta}|\langle\lambda_\alpha|\mathcal{O}|\lambda_\beta\rangle|^2 \leq (\Delta\mathcal{O})^2, \tag{6.4}$$

where $(\Delta\mathcal{O})^2 = \mathrm{Tr}(\rho\mathcal{O}^2) - \mathrm{Tr}(\rho\mathcal{O})^2$ is the variance and the states $|\lambda_\alpha\rangle$ and probabilities p_α are obtained from the decomposition of $\rho = \sum_\alpha p_\alpha|\lambda_\alpha\rangle\langle\lambda_\alpha|$ [172, 173]. For pure states, the inequality turns into an equality [172, 173]:

$$F_Q(\mathcal{O},\rho) = 4\left(\langle\mathcal{O}^2\rangle - \langle\mathcal{O}\rangle^2\right) \tag{6.5}$$

Besides metrology, the QFI is of interest when examining multi-partite entanglement, which becomes clear when considering observables that are sums of local terms, i.e. $\mathcal{O} = \frac{1}{2}\sum_{n=1}^{N} O_n$, where O_n has support on part n of a multi-partite system [173], e.g. qubit n in a qubit chain of length N.

In this case, the QFI can be used as an entanglement witness since it is bounded by $F_Q(\mathcal{O},\rho_{\mathrm{sep}}) \leq N$ for separable states (standard quantum limit) [7, 172–174]. For entangled states, the QFI is bounded by

$$F_Q \leq N^2, \tag{6.6}$$

known as the Heisenberg limit, where the equality is fulfilled by the GHZ state with an arbitrary phase for $O_n = \sigma_n^z$ in a qubit chain [7, 172]. Additionally, if $F_Q(\mathcal{O},\rho_{\mathrm{sep}}) \geq mN$, at least $m+1$ system parties are entangled [172, 174]. States obeying $F_Q(\mathcal{O},\rho_{\mathrm{sep}}) \geq (N-1)N$ are called *genuinely entangled* [172, 174], i.e. they cannot be rewritten as a product state of any bipartition of the system [64].

The next section is taken from Ref. [24], applying these concepts to our previously introduced active steering protocol.

6.2 Towards scalable active steering protocols for genuinely entangled state manifolds

6.2.1 Introduction

In this work, we present an active steering protocol that utilizes the *Quantum Fisher Information* (QFI) [175] as a cost function. Our QFI-based protocol allows one to efficiently reach a one-parameter manifold of genuinely entangled N-qubit states which maximize the QFI, namely

Green-Hornberger-Zeilinger (GHZ) states [29],

$$|\Psi\rangle = \frac{1}{\sqrt{2}}\left(|000\cdots\rangle + e^{i\phi}|111\cdots\rangle\right), \tag{6.7}$$

with an angular parameter ϕ. (For a system qubit with Pauli matrices $\sigma^{x,y,z}$, we use $\sigma^z|0\rangle = |0\rangle$ and $\sigma^z|1\rangle = -|1\rangle$.) By using the QFI as cost function, our protocol significantly accelerates the active steering process. It also allows one to target a specific state with a designated phase ϕ. Additionally, our findings suggest scalability with the system size N, offering promising potential for steering in larger quantum systems. We note that if one stops the protocol before the maximal value for the QFI has been reached, one may also access more general states beyond Eq. (6.7).

In contrast to the active steering protocol discussed below, which employs minimally invasive weak measurements, recent works have explored measurement-based protocols with a single round of strong (projective) Bell measurements plus feedback, see Refs. [126, 176, 177] and references therein. Such protocols allow one to prepare a broad family of genuinely multipartite entangled states, including the GHZ state (6.7), in a very efficient manner. Depending on the experimental platform at hand, it is nonetheless of interest to study active steering protocols since one can, in principle, access arbitrary target states, see Ref. [22] and our discussion below. Moreover, active steering protocols offer the potential for generalization to quantum systems with continuous degrees of freedom.

In Sec. 6.2.2, we formulate the active steering protocol in a platform-independent manner. Weak measurements and the associated quantum feedback effects have by now become standard experimental tools which are employed in various platforms, see, e.g., Refs. [43, 59, 100, 178–183]. They allow for high-precision measurements, and an application of these techniques to our protocol could be very promising. Moreover, as shown recently in Ref. [23] for one or two system qubits, by including amplitude damping and dephasing in the stochastic master equation, active steering schemes of the type considered below are expected to be robust against the presence of error channels with sufficiently weak error rate, see Sec. 5. In fact, Ref. [23] established the existence of a finite threshold error rate, and as long as the error rate stays below the threshold, errors can be corrected "on the fly" by the protocol. Albeit numerical simulations of the present version of our protocol including error channels are computationally prohibitively expensive for large N because one has to simulate the time evolution of mixed states, the fact that the error threshold rate is almost identical for $N = 1$ and $N = 2$ [23] suggests that a finite error threshold will persist at least for moderate values of N. If the system dynamics is described by a mixed state, one has to implement an unraveling procedure in practice for numerical stability. For large N, such approaches become exponentially costly in terms of computational demands. This restriction also applies when the detectors have non-ideal measurement efficiency since such effects are also captured by describing the system dynamics in terms of mixed states [31]. Furthermore, the QFI becomes more complicated for mixed states. For simplicity, we thus neglect external noise channels and non-ideal measurement efficiencies, and study the error-free case with ideal

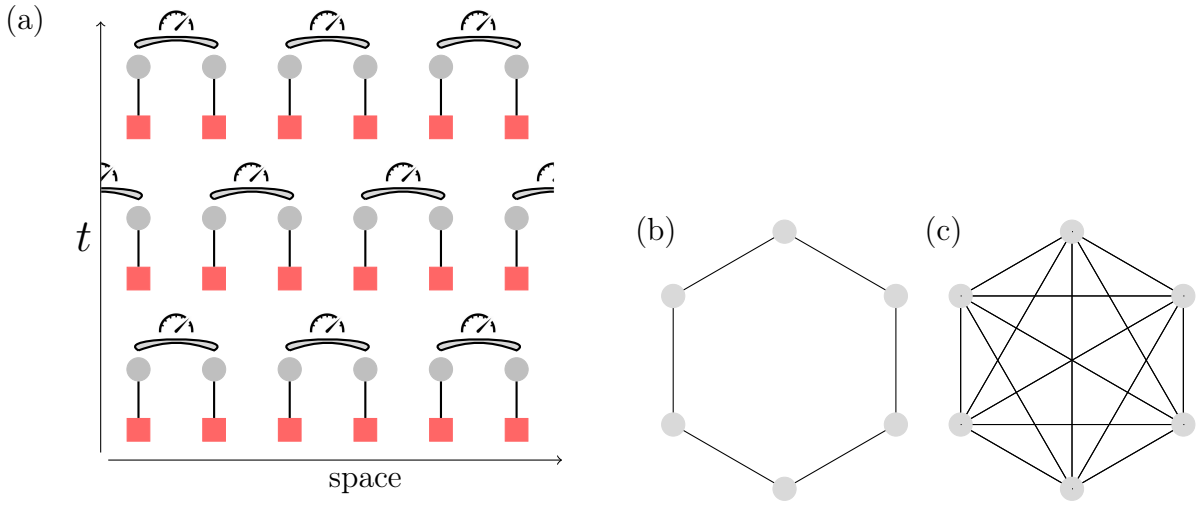

Figure 6.1: Schematic time evolution of the active steering protocol. (a) We show three time steps for $N = 6$ system qubits (red squares) coupled by steering operators H_{n,K_n} (straight vertical lines) to their own detector qubits (grey circles). The qubit chain has periodic boundary conditions. A possible scheme for the Bell measurements of neighboring detector qubit pairs in subsequent cycles is indicated. (b) We mainly consider the case of Bell measurements of nearest-neighbor detector qubit pairs. (c) In Fig. 6.5 below, we also study the case where arbitrary detector qubit pairs can be subjected to Bell measurements (full connectivity).

measurements below. However, a modified implementation of our protocol that may allow to circumvent these restrictions is discussed in Sec. 6.2.4.

Since weak measurements play a key role in our protocol, a physical realization with fast qubit readout is desirable, e.g., superconducting Andreev qubits with detector readout times of order 10 ns [17] could offer a good option [184]. We note that active steering protocols of similar type have recently been experimentally implemented [42, 185]. Our protocol assumes that the system is initialized at time $t = 0$ in a simple product state, say, $|\Psi(t = 0)\rangle = |000\cdots\rangle$, and that for a given measurement record, the state trajectory $|\Psi(t)\rangle$ can be stored and updated on a classical computer for each time step of the quantum protocol. After introducing the protocol in Sec. 6.2.2, we present numerical simulation results in Sec. 6.2.3. We primarily focus on the GHZ state, but we also show how to prepare so-called Dicke states using this approach. In Sec. 6.2.4, we discuss several open issues and directions for future research. In particular, we outline how the state tracking requirement may be avoided in modified implementations of our protocol.

6.2.2 Protocol and QFI

We schematically illustrate the protocol in Fig. 6.1 and Table 6.1. Each protocol step of time duration δt has two components, namely (i) unitary evolution of the coupled system and detector qubits under the chosen feedback Hamiltonian, followed by (ii) weak measurements of the system qubits via Bell pair measurements of the detector qubits. Depending on the measurement

choose $\|\Psi(0)\rangle = \|0\ldots0\rangle$ and $\mathcal{O}$		
Classical computer		Quantum computer
$\|\Psi(t)\rangle$		$\|\Psi(t)\rangle \to \|\Psi(t)\rangle \otimes \|00\rangle_d$
$\downarrow$		$\downarrow$
$\max_{K\in\mathcal{K}}\langle dF_Q(\|\Psi\rangle, K)\rangle_{\rm ms}$	$\xrightarrow{K\in\mathcal{K}}$	$e^{-i\delta t H_K}\|\Psi(t)\rangle \otimes \|00\rangle_d$
$\downarrow$		$\downarrow$
$\|\Psi(t+\delta t\|\xi,\eta)\rangle$	$\xleftarrow{(\xi,\eta)}$	${}_d\langle\Phi_{\xi,\eta}\|e^{-i\delta t H_K}\|00\rangle_d \times \|\Psi(t)\rangle$

Table 6.1: Active steering protocol using the QFI as cost function. A classical computation of the measurement-averaged cost function change $\langle dF_Q(|\Psi\rangle, K)\rangle_{\rm ms}$ determines the optimal coupling $K = (K_n, K_{n+1})$ out of the coupling family $\mathcal{K} = \{K_n = (\alpha_n, \beta_n)|\alpha_n \in \{x, y, z\}; \beta_n \in \{x, z\}\}$ for qubit pair $(n, n+1)$. This choice is fed into the quantum computer as system-detector coupling. After unitary time evolution of duration δt, the detector is measured in the Bell basis $|\Phi_{\xi,\eta}\rangle_d$, where ξ and η correspond to the possible measurement outcomes. These are fed back into the classical computer to update and keep track of the system state.

outcomes, the feedback Hamiltonian for the next iteration step is then determined according to the decision making scheme discussed below.

We consider N system qubits described by Pauli matrices σ_n^α (with $\alpha = x, y, z$ and $n = 1, \ldots, N$), where each system qubit couples only to its own detector qubit described by Pauli matrices τ_n^β. We neither allow for direct couplings between different system qubits nor between different detector qubits, while the Hamiltonian H_{n,K_n} ("steering operator") for the nth system-detector qubit pair can be selected from the set of Pauli gates,

$$H_{n,K_n} = J\sigma_n^{\alpha_n}\tau_n^{\beta_n}, \tag{6.8}$$

with $\alpha_n \in \{x, y, z\}$ and $\beta_n \in \{x, z\}$. For simplicity, we assume a fixed coupling J, where we put $J = +1$ in what follows, and degenerate zero-energy states for all uncoupled qubits. The steering parameters $K_n = (\alpha_n, \beta_n)$ are chosen according to a decision making scheme in every time step of the protocol as described below, with $[H_{n,K_n}, H_{n',K_{n'}}] = 0$ for arbitrary K_n and $K_{n'}$.

Table 6.1 illustrates the active steering protocol using Bell state measurements on neighboring pairs, see Fig. 6.1(b), of detector qubits. Later on, we also consider the case in Fig. 6.1(c) where Bell measurements can be performed for arbitrarily chosen pair orderings (where a given pairing order is determined from a uniform random distribution), but we focus on the nearest-neighbor case in what follows. For a given time step of the protocol, all non-overlapping pairs $(n, n+1)$ can be steered simultaneously, see Fig. 6.1(a). One can either choose an alternating sequence of pairings on subsequent time steps, as shown in Fig. 6.1(a), or simply assign the pairing order randomly. In our simulations, we found the second option to be more efficient. As explained below, the active decision making is performed on a classical computer using the knowledge about the present state of the system.

Let us now describe the protocol in detail. We start at time $t = 0$ by initializing all system

and detector qubits in $|0\rangle$ and $|0\rangle_d$ (the subscript d refers to detector qubit space), respectively, i.e., the system state is $|\Psi(t=0)\rangle = |000\cdots\rangle$. We then group the N qubits into neighboring pairs $(n, n+1)$, see Fig. 6.1, where all subsequent operations for different pairs commute and can thus be performed simultaneously. (For odd N, one "idle" qubit remains whose location is chosen from a uniform random distribution.) Given the state $|\Psi(t)\rangle$, for active steering towards the GHZ state, we select the steering couplings for this pair, (K_n, K_{n+1}), such that the measurement-averaged expectation value of the QFI after a time step of duration δt is maximized.

For a pure N-qubit state $|\Psi\rangle$, the QFI is defined as [172, 186–189]

$$F_Q = 4\left(\langle\Psi|\mathcal{O}^2|\Psi\rangle - \langle\Psi|\mathcal{O}|\Psi\rangle^2\right). \tag{6.9}$$

For collective observables $\mathcal{O} = \frac{1}{2}\sum_{n=1}^{N} O_n$, where O_n are local operators, the QFI can be used to probe the multipartite entanglement structure of the state $|\Psi\rangle$ [7, 173, 174]. If the QFI satisfies the inequality $F_Q > mN$, then at least $(m+1)$ parties of the system are entangled. Namely, $m \leq N$ represents the size of the biggest entangled block. The upper bound $F_Q \sim N^2$ corresponds to the so-called genuinely multipartite entanglement. In particular, the family of states which saturate the maximum value of the multipartite entanglement is an arbitrary superposition of the eigenvectors of $\mathcal{O}$ with largest and smallest eigenvalues. For $\mathcal{O} = \frac{1}{2}\sum_{n=1}^{N}\sigma_n^z$, these correspond to the states defined in Eq. (6.7).

In our protocol, we parametrize $O_n = \mathbf{s}_n \cdot \boldsymbol{\sigma}_n$, with $\mathbf{s}_n = (s_n^x, s_n^y, s_n^z)$ an arbitrary unit vector and $\boldsymbol{\sigma}_n = (\sigma_n^x, \sigma_n^y, \sigma_n^z)$. Using the optimal choice for (K_n, K_{n+1}), discussed below after Eq. (6.12), one time-evolves the coupled system-plus-detector system for a time step δt. Next, a projective measurement of the detector qubit pair is done in its Bell basis $\{|\Phi_{\xi,\eta}\rangle_d\}$ [29], where $|\Phi_{\xi=0,\eta=\pm}\rangle_d = (|00\rangle_d \pm |11\rangle_d)/\sqrt{2}$ and $|\Phi_{\xi=1,\eta=\pm}\rangle_d = (|01\rangle_d \pm |10\rangle_d)/\sqrt{2}$. Symmetric $(\eta=+1)$ and antisymmetric $(\eta=-1)$ Bell states have even $(\xi=0)$ or odd $(\xi=1)$ parity, where "symmetry" refers to qubit exchange while even (odd) "parity" means that states are built from the basis $\{|00\rangle_d, |11\rangle_d\}$ ($\{|01\rangle_d, |10\rangle_d\}$). Such measurements can be implemented by commuting measurements of the Pauli operators $\tau_n^z\tau_{n+1}^z = \pm 1$ and $\tau_n^x\tau_{n+1}^x = \pm 1$. Finally, one re-initializes all detector qubits in the state $|0\rangle_d$ and iterates the protocol until convergence has been achieved. Since the initial detector state $|00\rangle_d$ (for each time step and each qubit pair) has even parity, measurement outcomes with odd parity $(\xi=1)$ are referred to as quantum jumps. The above measurements realize entanglement swapping [33, 81–87] and tend to increase entanglement in the system state $|\Psi(t)\rangle \to |\Psi(t+\delta t)\rangle$, see Ref. [22] for a detailed discussion.

In the weak measurement limit $J\delta t \ll 1$ [26], the state change $|d\Psi\rangle = |\Psi(t+\delta t)\rangle - |\Psi\rangle$ with $|\Psi\rangle = |\Psi(t)\rangle$ for measurement outcome (ξ, η) is governed by a jump-type nonlinear stochastic Schrödinger equation (SSE) [25, 31, 100],

$$|d\Psi\rangle = \left[-i\delta t H_0 + \xi\left(\frac{c_\eta}{\sqrt{\langle c_\eta^\dagger c_\eta\rangle}} - 1\right) - \frac{\delta t}{2}\left(c_\eta^\dagger c_\eta - \langle c_\eta^\dagger c_\eta\rangle\right)\right]|\Psi\rangle, \tag{6.10}$$

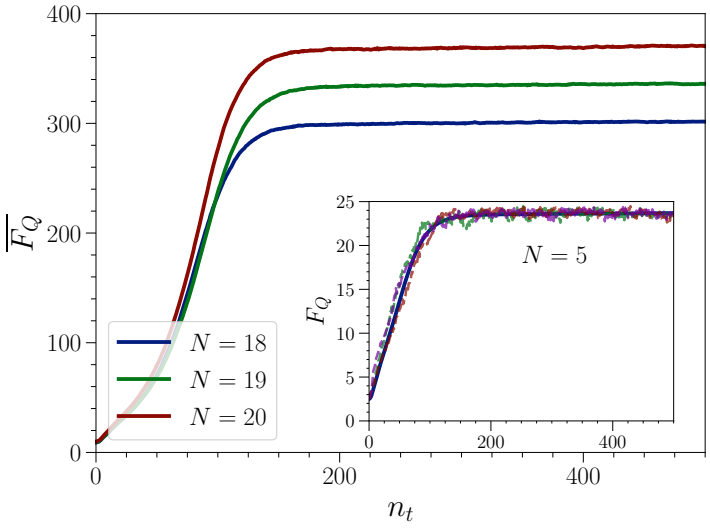

Figure 6.2: Average QFI $\overline{F_Q}$ vs number of time steps $n_t = t/\delta t$ for different N and $J\delta t = 0.2$. Note that $F_Q \leq N^2$. Averages are over 100 trajectories. The inset shows $\overline{F_Q}$ vs n_t (solid curve) for $N = 5$ (averaged over 8000 trajectories), together with three individual measurement trajectories (dashed curves).

where $H_0 = J\sum_{m=n,n+1}\delta_{\beta_m,z}\sigma_m^{\alpha_m}$ and $\langle c_\eta^\dagger c_\eta\rangle = \langle\Psi|c_\eta^\dagger c_\eta|\Psi\rangle$. The jump operators $c_{\eta=\pm}$ are given by

$$c_\eta = -iJ\sqrt{\delta t}\left(\eta\delta_{\beta_n,x}\sigma_n^{\alpha_n} + \delta_{\beta_{n+1},x}\sigma_{n+1}^{\alpha_{n+1}}\right), \tag{6.11}$$

where the outcome (ξ,η) has the *a priori* probability $P_{\xi,\eta} = \frac{1}{2}[\delta_{\xi,0}+(\delta_{\xi,1}-\delta_{\xi,0})\delta t\langle c_\eta^\dagger c_\eta\rangle]$. Averaging over the measurement outcomes after one time step, one arrives at the anticipated average change in QFI after the next time step,

$$\begin{aligned}\langle dF_Q\rangle_{\rm ms} &= \langle F_Q(t+\delta t)\rangle_{\rm ms} - F_Q(t) \\ &= 4\Big(\mathrm{Tr}\left(\mathcal{O}^2\langle d\rho\rangle_{\rm ms}\right) - 2\mathrm{Tr}\left(\mathcal{O}\langle d\rho\rangle_{\rm ms}\right)\mathrm{Tr}(\mathcal{O}\rho) - \left\langle[\mathrm{Tr}(\mathcal{O}\,d\rho)]^2\right\rangle_{\rm ms}\Big)\end{aligned} \tag{6.12}$$

with $d\rho = |d\Psi\rangle\langle\Psi| + |\Psi\rangle\langle d\Psi| + |d\Psi\rangle\langle d\Psi|$ and $\rho = |\Psi\rangle\langle\Psi|$. (Here $\langle A\rangle_{\rm ms}$ denotes a measurement average of the quantity A using the probabilities $p_{\xi,\eta}$.) We compute $\langle dF_Q\rangle_{\rm ms}$ for all possible steering parameters and then choose (K_n, K_{n+1}) such that $\langle dF_Q\rangle_{\rm ms}$ is maximized. We emphasize that (K_n, K_{n+1}) is determined separately for each qubit pair at a given time step. In our numerical simulations, the system state is propagated according to the SSE (6.10). In contrast to Ref. [22], the time evolution is not terminated once a certain threshold value for F_Q has been reached, but the quantum state trajectory continues evolving according to the above protocol.

Let us provide some details on the calculation of $\langle dF_Q\rangle_{\rm ms}$. The classical computation of $\langle dF_Q(|\Psi\rangle, K)\rangle_{\rm ms}$ for $H_K = H_{n,K_n} + H_{n+1,K_{n+1}}$ with $K = (K_n, K_{n+1})$ is performed numerically

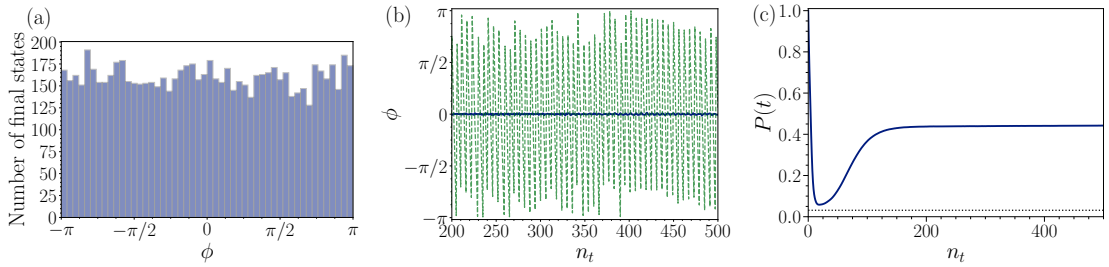

Figure 6.3: Active steering protocol for $N = 5$ and $J\delta t = 0.2$. Measurement averages are over 8000 trajectories. (a) Histogram of the phase ϕ in Eq. (6.7) found after $n_t = 500$ time steps. (b) Time evolution of the phase ϕ after convergence to the target manifold has been reached, shown for one individual measurement trajectory (dashed green curve) and for the average (solid blue curve). (c) Purity $P(t)$ vs n_t, see Eq. (6.16). The dotted line corresponds to the maximally mixed (infinite temperature) state.

in a Bloch tensor representation of the system state,

$$|\Psi\rangle\langle\Psi| = \frac{1}{2^N}\sum_{\mathcal{S}} R_{\mathcal{S}}\mathcal{S}, \quad R_{\mathcal{S}} = \langle\Psi|\mathcal{S}|\Psi\rangle, \tag{6.13}$$

with the Pauli string operator $\mathcal{S} = \sigma_1^{\mu_1}\sigma_2^{\mu_2}\cdots\sigma_N^{\mu_N}$ with $\mu_j \in \{0,1,2,3\}$. Using this representation to parametrize the observables, the average QFI change is obtained as

$$\begin{aligned}\langle dF_Q\rangle_{\rm ms} = &\sum_{n\neq m}\sum_{\alpha_i,\alpha_j} s_n^{\alpha_n} s_m^{\alpha_m}\langle dQ_{n,m}^{\alpha_n,\alpha_m}\rangle_{\rm ms} - 2\left(\sum_{n,\alpha_n} s_n^{\alpha_n}\langle dR_n^{\alpha_n}\rangle_{\rm ms}\right)\left(\sum_{n,\alpha_n} s_n^{\alpha_n} R_n^{\alpha_n}\right)\\ &- 2\delta t\sum_{\eta}\frac{1}{\langle c_\eta^\dagger c_\eta\rangle}\left(\sum_{n,\alpha_n} s_n^{\alpha_n} G_{\alpha_n}^{(\eta)}\right)^2,\end{aligned} \tag{6.14}$$

where we used the reduced single-qubit Bloch vectors $R_n^{\alpha_n} = \langle\Psi|\sigma_n^{\alpha_n}|\Psi\rangle$ and the two-qubit correlators $Q_{n,m}^{\alpha_n,\alpha_m} = \langle\Psi|\sigma_n^{\alpha_n}\sigma_m^{\alpha_m}|\Psi\rangle$. For explicit expressions for $\langle dR_n^{\alpha_n}\rangle_{\rm ms}$ and $\langle dQ_{n,m}^{\alpha_n,\alpha_m}\rangle_{\rm ms}$, see Eq. (27) in Ref. [22]. The second-order state change of the single qubit density matrices for $\xi = 1$ measurement outcomes is given by

$$\begin{aligned}G_{\mu_i}^{(\eta)} &= -\sum_{m=n,n+1}\sum_{\alpha\neq\alpha_i}\Gamma_m\delta_{\beta_m,x}\delta_{\mu_i,\alpha}R_{\mu_i} + \eta\sqrt{\Gamma_n\Gamma_{n+1}}\delta_{\beta_n,x}\delta_{\beta_{n+1},x}\left(\mathcal{F}_{\mu_i} - Q_{n,n+1}R_{\mu_i}\right),\\ \mathcal{F}_{\mathcal{S}} &= \frac{1}{2^{N+1}}\sum_{\mathcal{S}'} R_{\mathcal{S}'}\mathrm{Tr}\left((\sigma_n^{\alpha_n}\mathcal{S}'\sigma_{n+1}^{\alpha_{n+1}} + \sigma_{n+1}^{\alpha_{n+1}}\mathcal{S}'\sigma_n^{\alpha_n})\mathcal{S}\right).\end{aligned} \tag{6.15}$$

With a chosen coupling (K_n, K_{n+1}) for the following time step, the quantum system is evolved accordingly, and the detector is measured subsequently. The stochastic outcome of this measurement is recorded and used to keep track of the running state on the classical computer.

We note that for the preparation of non-GHZ state families, one may choose a specific target value of the QFI, F_Q^*, and then minimize the cost function $|F_Q - F_Q^*|$. This approach allows one to use active steering protocols targeting different classes of state manifolds associated with a specific QFI value. As an example, we show results for Dicke states in Sec. 6.2.3 below.

6.2.3 Numerical simulation results

We now show simulation results for the above protocol maximizing the QFI. For the steering operator set (6.8), it is convenient to choose $\mathbf{s}_n = \frac{1}{\sqrt{2}}(1,0,1)^T$, see Eq. (6.9), but our results are robust under small rotations of this unit vector. Correspondingly, the GHZ states (6.7) are defined with respect to rotated states $|0\rangle \to |0'\rangle$ and $|1\rangle \to |1'\rangle$. Up to a normalization factor, $|0'\rangle = |0\rangle + (\sqrt{2}-1)|1\rangle$ and $|1'\rangle = (1-\sqrt{2})|0\rangle + |1\rangle$. In Fig. 6.2, we show the evolution of the time-dependent QFI. The main panel illustrates the average QFI $\overline{F_Q(t)}$ (the overbar indicates an average over many measurement trajectories) for several values of N, where we observe that the QFI comes close to its maximum value $F_Q = N^2$ after $n_t \approx 200$ time steps. This number for n_t is basically independent of N. In the inset of Fig. 6.2, for $N = 5$, we illustrate the convergence behavior of the QFI both for individual measurement trajectories and for the average.

Next, we show that the target manifold (6.7) is reached to good accuracy. In Fig. 6.3(a), for $N = 5$, we show a histogram of the phase $\phi = \arg\left(\langle 0'0'0'\cdots|\Psi\rangle\langle\Psi|1'1'1'\cdots\rangle\right)$ measured after 500 time steps. We find that the histogram is rather flat, implying that the quantum state trajectories uniformly explore the entire manifold even though they all start from the same initial state. Alternatively, as illustrated in Fig. 6.3(b), one may take an individual measurement trajectory and follow it over time. For our choice of steering operators (6.8), almost regular oscillations are observed, where again all possible values of ϕ are reachable over the course of time. By invoking a termination policy, one can then target a specific state with a predesignated value of ϕ. Finally, in Fig. 6.3(c), we show the purity [127–129],

$$P(t) = \mathrm{Tr}\left(\overline{\rho(t)}^2\right), \tag{6.16}$$

as a function of n_t. Interestingly, the average state $\overline{\rho(t)}$ first approaches an infinite-temperature state where the purity gap (almost) closes [190], but the purity then increases again towards the asymptotic value 1/2. This value is readily explained by the fact that averaging over the phase in Eq. (6.7), one produces the asymptotic average state

$$\overline{\rho} = \frac{1}{2}\left(|000\cdots\rangle\langle 000\cdots| + |111\cdots\rangle\langle 111\cdots|\right), \tag{6.17}$$

which has purity $P = 1/2$ for all N. The difference to the numerically observed asymptotic purity in Fig. 6.3(c) is due to the finite value of $J\delta t$. We find that this difference becomes smaller by reducing $J\delta t$, see also below.

Let us now discuss the dependencies on the protocol's parameters. The scaling of the accuracy

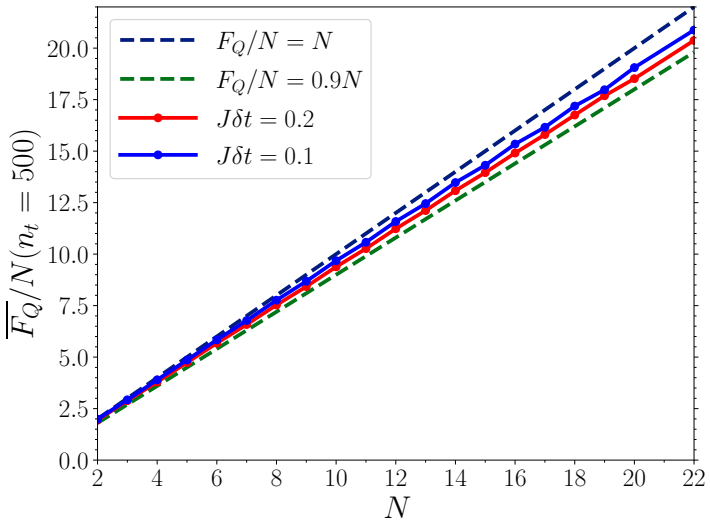

Figure 6.4: Scaling of the accuracy of the asymptotic value of the averaged QFI $\overline{F_Q}/N$ vs N for $J\delta t = 0.1$ (blue) and $J\delta t = 0.2$ (red). Results have been averaged over at least 100 measurement trajectories. (For $N \leq 10$, we used 10000 trajectories; for $N = 11$ to 15, we averaged over 5000, and for $N \in \{16, 17\}$, over 1000 trajectories.) Solid lines are guides to the eye only. The upper bound, $\overline{F_Q}/N = N$, is shown as black dashed line, the green dashed line indicates $\overline{F_Q}/N = 0.9N$.

of the value of $\overline{F_Q}$ reached after $n_t = 500$ steps with system size N is shown in Fig. 6.4 for two values of $J\delta t$. We observe that for smaller $J\delta t$, higher accuracy can be reached because of the decreased importance of quantum jumps at long protocol times, which tend to deteriorate the QFI momentarily. However, using smaller values for $J\delta t$ comes with longer physical run-times of the protocol.

In Fig. 6.5, we report the scaling of the number of steps n_t needed for reaching a QFI of $\overline{F_Q}/N^2 = 0.9$, for the same values of $J\delta t$ as in Fig. 6.4. Here, we also compare to a situation where one allows for Bell pair measurements between arbitrary detector pairs (not only nearest neighbors), see Fig. 6.1(c), which tends to accelerate the protocol. In this case, all non-overlapping pairs (n, n') with $n, n' \in \{1, \ldots, N\}$ can again be steered simultaneously, where both the pairings (and the idle qubit for odd N) are chosen from a uniform random distribution for each time step. Such a fully connected Bell measurement pairing scheme results in a faster convergence to the target state since more options for finding optimal feedback Hamiltonians can be explored.

We observe an even-odd effect in Fig. 6.5, in particular for small N, which originates from the presence of the idle qubit for odd N in our Bell pair measurement scheme. Remarkably, the required number of steps n_t increases only very slowly with N, suggesting *scalability* of the active steering protocol for large N. The fitting curves shown as thin solid lines in Fig. 6.5 indicate a scaling $n_t \sim \mathcal{O}(\ln N)$. Such favorable scaling is also corroborated by Fig. 6.2, where we show the n_t-dependence of $\overline{F_Q}$ for several (large) values of N.

In addition to targeting states with maximum QFI, our protocol also allows for the preparation

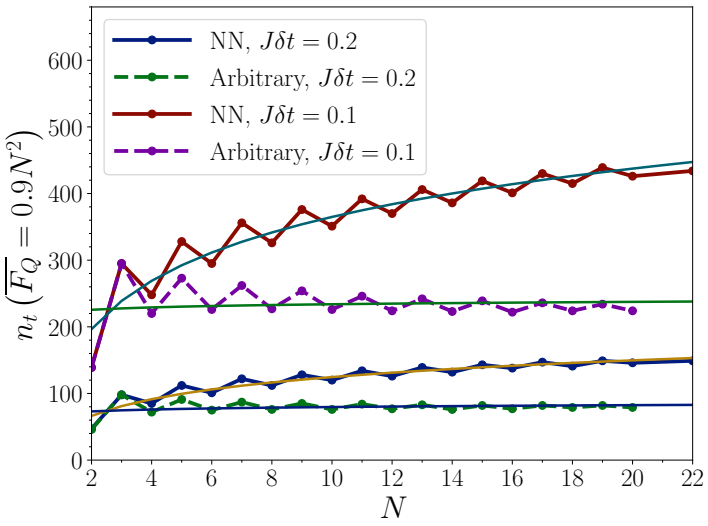

Figure 6.5: Scaling of the step number n_t vs N needed for reaching the averaged QFI value $\overline{F_Q} = 0.9N^2$, shown for $J\delta t = 0.1$ and $J\delta t = 0.2$. Averages are over at least 100 trajectories. Thick solid and dashed curves connecting data points are guides to the eye only. The thin solid lines show numerical fits to the function $n_t^*(N) = A + B\ln(N)$ to the respective data, with fitting parameters A and B. For instance, we obtain $A \simeq 104.6$ and $B \simeq 124$ for nearest-neighbor couplings with $J\delta t = 0.1$ from such a fit. We show results for nearest-neighbor detector qubit measurements (solid) as well as allowing for arbitrary detector pair measurements (dashed curves), see Fig. 6.1.

of states associated with different (non-maximal) target values F_Q^* of the QFI. In order to do so, we simply choose $|F_Q - F_Q^*|$ as cost function in the steering protocol. As an example for this approach, we here consider the case of *Dicke states* [172], which for qubits can be written as

$$|D_{k,N}\rangle = \begin{pmatrix} N \\ k \end{pmatrix}^{-\frac{1}{2}} \sum_j \mathcal{P}_j(|0\rangle^{\otimes N-k}|1\rangle^{\otimes k}). \tag{6.18}$$

In Eq. (6.18), the sum runs over all possible permutations $\mathcal{P}_j$ of distributing k excited qubits in an N-qubit system. For the state in Eq. (6.18), the QFI has the value [172]

$$F_Q^* = \frac{N^2}{2} - 2\left(\frac{N}{2} - k\right)^2 + N. \tag{6.19}$$

As for GHZ states, the Dicke states in Eq. (6.18) can, in addition, contain arbitrary phase differences between the corresponding basis states, with the same value of F_Q^*. In general, our protocol will therefore target an entire state manifold for a given QFI value.

In analogy to Fig. 6.2, Figure 6.6 shows numerical simulation results for the QFI-based preparation of Dicke states with target value F_Q^* in Eq. (6.19) for $k = N/2$ and up to $N = 18$ qubits. We observe that the target value of the QFI is reached after $n_t \approx 70$ time steps,

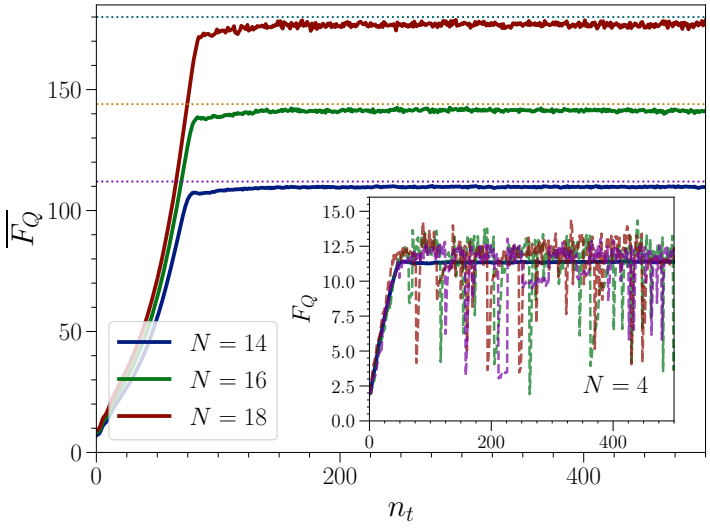

Figure 6.6: Average QFI $\overline{F_Q}$ vs number of time steps $n_t = t/\delta t$ for an active steering protocol with cost function $|F_Q - F_Q^*|$ and F_Q^* in Eq. (6.19), targeting the Dicke states $|D_{k,N}\rangle$ in Eq. (6.18) for $k = N/2$ and various N, with $J\delta t = 0.2$. Averages are over 5000 (1000, 500) trajectories for $N = 14\,(16, 18)$. Dotted lines indicate the respective F_Q^* in Eq. (6.19). The inset shows $\overline{F_Q}$ vs n_t (solid curve, averaged over 10^4 trajectories) for $N = 4$, together with three individual measurement trajectories (dashed curves).

independently of the value of N. The protocol thus converges significantly faster than for GHZ states. However, even though $\overline{F_Q}$ is close to the target value F_Q^*, individual trajectories now exhibit stronger fluctuations, see the inset of Fig. 6.6. We note in passing that by implementing a stoppage criterion in the protocol [22], i.e., by terminating the protocol once the QFI target value has approximately been reached, we expect that such fluctuations can be reduced. In any case, we conclude that the QFI-based protocol is also useful for generating other highly entangled state manifolds beyond GHZ states.

6.2.4 Discussion

We have proposed an active steering protocol targeting the one-parameter manifold of N-qubit GHZ states (6.7) with genuine multipartite entanglement by means of weak Bell pair measurements and active feedback. In contrast to fidelity-based cost functions [22], by using the QFI as a cost function, our results suggest that the active steering protocol may become scalable with increasing system size N. Although it is well known that GHZ states may be generated by projective measurements in shallow circuits [125, 176, 177], our results are relevant for at least two reasons beyond those specified in Sec. 6.2.1: (i) We clarify similarities and differences between active and passive steering protocols for the case of a target state *manifold*. In passive steering [14, 32], measurement outcomes are discarded. Such protocols are basically equivalent to driven-dissipative systems [191–195] with engineered dissipation, see Refs. [11, 12, 26, 169–171, 196–205] and

corresponding experiments [43, 206–210]. In contrast to the passive steering case, where the initial state uniquely determines the final state within the dark space forming the target manifold [119], we find that under active steering, the quantum state trajectory continues cycling through the target manifold. The initial state then plays no special role, and all phases ϕ in Eq. (6.7) are reached with equal probability as the protocol evolves. (ii) One may also target highly entangled non-stabilizer state manifolds, for which simpler routes along the lines of Ref. [125] are not available. Under quite general conditions, many highly entangled states, including Eq. (6.7), cannot be reached by driven-dissipative and/or passive steering [13]. For small N, it has been demonstrated that they remain accessible to active steering protocols [22].

In fact, one can apply a slightly modified version of the present protocol, which has favorable scaling properties with system size, in order to prepare broad classes of other states, including the so-called W, Dicke, and cluster states [29]. This task may be achieved, for instance, by stopping the protocol at a suitable value of F_Q before the convergence to the maximal QFI has been reached. Alternatively, one can select a target value F_Q^* for the QFI associated with the desired family of target states, and then choose $|F_Q - F_Q^*|$ as cost function. For instance, the Dicke states $|D_{k,N}\rangle$ in Eq. (6.18) with associated QFI F_Q^* in Eq. (6.19) have been studied for $k = N/2$ excitations above, see Fig. 6.6. Another possibility to reach non-GHZ states is to add a non-stabilizerness quantifier [211, 212] to the cost function.

For experiments, a modified implementation of our protocol where state tracking is not required would be highly beneficial. Without state tracking, one could both study larger system sizes and tolerate error channels with weak error rates. Such protocols can be formulated if weak measurements of all one- and two-body correlations present in the system state can be performed [26] since $\overline{dF_Q}$ in Eq. (6.12) depends only on those correlations. As a result, the protocol could be entirely based on the outcomes of weak measurements without any need for state tracking. In particular, our simulations only use the values of the one- and two-body correlations R_{μ_i} and $Q_{n,m}^{\alpha_n,\alpha_m}$ defined after Eq. (6.14) in order to determine the optimal couplings K entering the feedback Hamiltonian. Counting the number of one- and two-body correlators, we expect that the performance of such a protocol will scale $\sim N^2$. Noting that our numerical simulations are mainly limited by the computational demands of updating the SSE, which is not necessary anymore when switching to a protocol directly utilizing weak measurements of one- and two-body correlations, we expect that such a protocol can be applied to larger values of N. In addition, it allows for the presence of error channels and/or measurement inefficiencies. However, a detailed exploration of this interesting direction is beyond the scope of this work.

Finally, given that the state manifolds that can be targeted by our protocol could allow one to overcome classical limits in quantum phase estimation and to attain the so-called Heisenberg limit [186–189], it is a promising option to employ active steering protocols using the QFI for entanglement-enhanced metrology and sensing applications, see also Refs. [172, 213–215]. However, this remains feasible provided errors have a limited impact and if an optimal measurement, dependent on the state, can be performed. A comprehensive analysis of how errors affect state

preparation, sensing, and measurement is left for future work.

Chapter 7

Conclusion & Outlook

In this work, recent advances and results of state preparation protocols using measurements were presented. This includes a new proposal for active feedback protocols where measurement outcomes are used to keep track of the system along the course of the protocol.

Starting from a general description of the dynamics of (open) monitored quantum systems, previous *measurement steering* protocols were presented in preparation for the shown new results. In the discussed weak-measurement limit, the resulting EOM of the system takes on the form of a stochastic equation that depends on the outcomes of the detector measurements. In particular, these dynamics also depend on the measured operator, allowing for phenomena like entanglement swapping beyond *blind* measurement protocols.

These methods were used for the main result of the work, presenting a protocol of target state preparation based on the optimization of a *local* cost function. In contrast to previous works, steering is performed by measuring pairs of detector qubits in the maximally entangled Bell basis. This operation avoids direct couplings between system qubits, using only local couplings between system qubits and their respective detectors. The system is directed towards the pre-chosen target state in an active way by using a cost function-based protocol. It was shown that this cost function needs to include local terms for successful steering. Numerical results were shown, where this cost function allowed the preparation of many-qubit entangled states like the GHZ and the W state. In this way, the no-go theorem for state preparation of entangled states by local couplings for Lindbladian dynamics present in blind steering and drive-and-dissipation protocols was overcome. Additionally, no comparable blind steering protocol exists by using such a weak-measurement variant of entanglement swapping.

As an extension of the presented protocol, which was formulated in an idealized system, next, environmental effects were included. Both amplitude damping and dephasing were considered using Lindbladian dynamics. Here, a threshold transition was reported, akin to the known phase transition appearing in QEC systems as a function of the error rate. The transition was shown numerically for both single-qubit and two-qubit systems by a closure of the purity gap. Numerical cost hindered the analysis of bigger systems, which will be necessary to verify the nature of the

transition. This motivates the development of new numerical tools for the simulation of such systems in the future.

In order to overcome limitations in terms of scalability to multi-qubit systems, the previous cost function was replaced in the next work in Chapter 6 by the *Quantum Fisher Information*. Discarding possible environmentally induced errors, this entanglement witness allows the preparation of genuinely entangled multi-qubit states in a scalable way, underlined by simulations up to 22 qubits. It is maximized by GHZ-like states known as genuinely entangled states. In contrast to the previous results, however, these states span a manifold, leading to a cyclic motion of the final states in this manifold. Numerical results up to $N = 22$ qubits were presented, showing a favorable scaling of the steering time with system size, especially when improving the qubit connectivity of the detectors.

The descriptions used here are still restricted by only considering environmental errors for a few qubits due to numerical costs. First experimental results for blind measurement steering have been reported [42], however, these are still limited in terms of system size and target fidelity. In order to scale the presented active steering results to bigger systems including different error sources, numerical advances will be necessary, possibly using many-body physics methods like tensor networks or neural networks [121]. Nonetheless, already for small systems, comparing the shown numerical results with measurement steering on an actual quantum chip might be of interest for future work. In particular, measurement steering protocols might be optimized when considering a specific platform, by using specifically available couplings, in contrast to the general formulation in this work.

The presented errors are still quite limited by only examining one- and two-qubit systems with one-qubit error channels. A more in-depth analysis might include correlated errors of multiple qubits in bigger systems and additional environmentally induced errors. Also, the investigation of inefficient measurements and errors in detector reinitialization will play an important role on the way to a protocol implementation [26, 31]. In particular, devices with short measurement times are necessary for running measurement steering in an experiment.

With the advent of NISQ devices, the need for a better understanding of the general dynamics in such systems will increase, especially with respect to their control. These devices will allow for testing different possible effects predicted by theory, like the previously reported measurement-induced phase transitions [2–4]. Recent advances in the field of machine learning might play an important role in this field, with clear connections to cost function-based measurement steering protocols as discussed. In particular, neural networks have been recently proposed for measurement-based feedback for state preparation in variational quantum circuits [216]. While each approach has its advantages and limitations, a hybrid protocol combining previous works might prove useful for measurement-based state preparation in the future. In summary, these recent advances make this research field a highly interesting playground for future developments, both for new theoretical protocols and their experimental implementations.

Appendix A

General qubit basis measurement

This appendix contains the generalization of the stochastic equations presented in Chapter 2.2. There, only the measurement in the computational z-basis and the x-basis was considered, giving jump and diffusion equations, respectively. Here, we extend these results by examining the measurement in a general qubit basis.

As in the main text, we consider a single detector qubit initialized in the state $|0\rangle_d$ and coupled to an arbitrary system by the coupling Hamiltonian H_{sd} for time δt. Now, we want to consider a detector measurement in an arbitrary basis

$$|\tilde{0}\rangle_d = \cos(\theta)|0\rangle_d + \sin(\theta)e^{i\phi}|1\rangle_d, \quad |\tilde{1}\rangle_d = \sin(\theta)|0\rangle_d - \cos(\theta)e^{i\phi}|1\rangle_d, \tag{A.1}$$

with arbitrary rotation angles $\phi \in [0, 2\pi[$ and $\theta \in [0, \frac{\pi}{4}]$.[1] This measurement process then corresponds to measuring the operator $\tilde{\tau}^z = {}_d|\tilde{0}\rangle\langle\tilde{0}|_d - {}_d|\tilde{1}\rangle\langle\tilde{1}|_d$ projectively on the detector.

As mentioned, the resulting new Kraus operators $A_{\tilde{0}} = {}_d\langle\tilde{0}|e^{-i\delta t H_{sd}}|0\rangle_d = {}_d\langle 0|U^\dagger e^{-i\delta t H_{sd}}|0\rangle_d$ and $A_{\tilde{1}} = {}_d\langle\tilde{1}|e^{-i\delta t H_{sd}}|0\rangle_d$ can be obtained from the operators A_ξ in Eq. (2.16) through the unitary basis transformation U as

$$\begin{pmatrix} A_{\tilde{0}} \\ A_{\tilde{1}} \end{pmatrix} = \begin{pmatrix} \cos(\theta) & \sin(\theta)e^{-i\phi} \\ \sin(\theta) & -\cos(\theta)e^{-i\phi} \end{pmatrix} \begin{pmatrix} A_0 \\ A_1 \end{pmatrix}, \tag{A.2}$$

where the matrix corresponds to the complex conjugate U^*.[2] For $\theta = 0$, the same results as for the jump-type evolution will be recovered, while for $\theta = \pi/4$ the measurements of τ^x and τ^y are obtained upon appropriate choice of the phase ϕ.

We see that the phase shift induced by ϕ only acts on A_1 and can therefore be removed from the matrix and absorbed into $\tilde{A}_1 = e^{-i\phi}A_1$. Correspondingly, in the weak-measurement limit, the phase can be used to rotate the definition of the jump operator by setting $\tilde{c} = e^{-i\phi}c$. This is

[1] It is enough to restrict ourselves to this interval since any other values of θ are equivalent to a corresponding transformation of ϕ or to exchanging $\tilde{0} \leftrightarrow \tilde{1}$.

[2] Note, that this description is equivalent to the detector being measured in the computational basis after having been initialized in the new basis state $U^\dagger|0\rangle$ and coupled to the system by the rotated Hamiltonian $\tilde{H}_{sd} = U^\dagger H_{sd} U$.

reminiscent of the phase appearing in the stochastic equations describing Heterodyne detection in quantum optics [30, 38], which can be obtained by using a time-dependent phase $\phi = \phi(t)$ and $\theta = \pi/4$, effectively rotating the measurement basis around the $x-y$-equator on the Bloch sphere.

The probability for measurement outcome $\tilde{1}$ is now given as

$$P_{\tilde{1}} = \sin^2(\theta)\left(1 - \cot(\theta)\sqrt{\delta t}\langle\tilde{c} + \tilde{c}^\dagger\rangle - \delta t\langle\tilde{c}^\dagger\tilde{c}\rangle\left(1 - \cot^2(\theta)\right)\right), \tag{A.3}$$

with $P_{\tilde{0}} = 1 - P_{\tilde{1}}$. We note that this equation is defined for all values of θ.

As for the special cases discussed in the main text, we can now obtain the normalized system state after the measurement by a suitable expansion. However, the expansion for $\rho_s\left(\tilde{1}\right)$ here depends on the value of θ.

Firstly, we assume that $\theta > 0$ and $\cot(\theta)\sqrt{\delta t}\|\tilde{c}\| \ll 1$, so that we can expand the denominator such that

$$\begin{aligned}\delta\rho_s\left(\tilde{1}\right) = \delta t\mathcal{L}\rho_s &+ \left(\cot^2(\theta)\delta t\langle\tilde{c}^\dagger\tilde{c}\rangle - \delta t\langle\tilde{c}^\dagger\tilde{c}\rangle\right)\left(\frac{\tilde{c}\rho_s\tilde{c}^\dagger}{\langle\tilde{c}^\dagger\tilde{c}\rangle} - \rho_s\right) \\ &+ \left(-\cot(\theta)\sqrt{\delta t} - \cot^2(\theta)\delta t\langle\tilde{c} + \tilde{c}^\dagger\rangle\right)\left(\tilde{c}\rho_s + \rho_s\tilde{c}^\dagger - \langle\tilde{c} + \tilde{c}^\dagger\rangle\rho_s\right).\end{aligned} \tag{A.4}$$

An analogous expansion can be done for $\rho_s\left(\tilde{0}\right)$ by replacing $\cot \to -\tan$. In particular, that result is always defined in the aforementioned interval of θ.

We can now define a stochastic variable $\tilde{\eta}$ which takes the value $-\cot(\theta)\sqrt{\delta t}$ for measurement outcome $\tilde{1}$ and $\tan(\theta)\sqrt{\delta t}$ for $\tilde{0}$. The average over measurement outcomes is then given for this new variable as

$$\langle\tilde{\eta}\rangle_{\mathrm{ms}} = \tan(\theta)\sqrt{\delta t}P_{\tilde{0}} - \cot(\theta)\sqrt{\delta t}P_{\tilde{1}} = \delta t\langle\tilde{c} + \tilde{c}^\dagger\rangle. \tag{A.5}$$

A difference to the diffusive variable used in the main text arises from the fact that $\tilde{\eta}^2 \neq \delta t$, but rather its value again depends on the measurement outcome. In particular, it holds that

$$\tilde{\eta}^2 - \delta t = -2\cot(2\theta)\sqrt{\delta t}\tilde{\eta}, \quad \langle\tilde{\eta}^2\rangle_{\mathrm{ms}} = \delta t, \tag{A.6}$$

recovering the correct order after averaging over measurement outcomes and removing higher-order terms.

This relation allows us to replace $\tilde{\eta}^2$ to again write a general SME, given as

$$\begin{aligned}\delta\rho_s(\tilde{\eta}) = \delta t\mathcal{L}\rho_s &- 2\cot(2\theta)\sqrt{\delta t}\tilde{\eta}\langle\tilde{c}^\dagger\tilde{c}\rangle\left(\frac{\tilde{c}\rho_s\tilde{c}^\dagger}{\langle\tilde{c}^\dagger\tilde{c}\rangle} - \rho_s\right) \\ &+ \left(\tilde{\eta}(1 + 2\cot(2\theta)\sqrt{\delta t}\langle\tilde{c} + \tilde{c}^\dagger\rangle) - \delta t\langle\tilde{c} + \tilde{c}^\dagger\rangle\right)\left(\tilde{c}\rho_s + \rho_s\tilde{c}^\dagger - \langle\tilde{c} + \tilde{c}^\dagger\rangle\rho_s\right).\end{aligned} \tag{A.7}$$

We easily see that for $\theta = \pi/4$ the results from the main text are recovered. However, for $\theta \neq \pi/4$ a new stochastic contribution appears at order $\sqrt{\delta t}$ which vanishes when taking the average over

measurement outcomes since $\langle\tilde{\eta}\rangle_{\mathrm{ms}} \propto \delta t$. Therefore, as expected, the usual Lindblad EOM (2.21) is obtained when measurement outcomes are discarded.

As in the main text, when considering pure states, the evolution can be equivalently expressed in terms of an SSE, which for this measurement direction is given as

$$\begin{aligned}\delta|\Psi_s(\tilde{\eta})\rangle = &\left(-i\delta t H_L - \frac{1}{2}\delta t\tilde{c}^\dagger\tilde{c} - \delta t\frac{\langle\tilde{c}+\tilde{c}^\dagger\rangle}{2}\tilde{c} + \frac{3}{8}\delta t\langle\tilde{c}+\tilde{c}^\dagger\rangle^2\right)|\Psi_s\rangle \\ &+ \tilde{\eta}\left(\tilde{c} - \frac{\langle\tilde{c}+\tilde{c}^\dagger\rangle}{2}\right)|\Psi_s\rangle \\ &+ 2\cot(2\theta)\sqrt{\delta t}\tilde{\eta}\left(\frac{\langle\tilde{c}+\tilde{c}^\dagger\rangle}{2}\tilde{c} - \frac{3}{8}\langle\tilde{c}+\tilde{c}^\dagger\rangle^2 + \frac{1}{2}\langle\tilde{c}^\dagger\tilde{c}\rangle\right)|\Psi_s\rangle. \end{aligned} \tag{A.8}$$

We saw that the stochastic variable $\tilde{\eta}$ has fundamentally different properties than the diffusive and jump-type stochastic variables η and ξ presented in the main text. This choice of the stochastic variable, however, is not unique and can be changed. To avoid the measurement dependence of the squared stochastic variable, one can alternatively do a recentering and rescaling by defining $\delta\tilde{W} = \sin(2\theta)\left(\tilde{\eta} + \cot(2\theta)\sqrt{\delta t}\right)$ which takes the value $+\sqrt{\delta t}$ for outcome $\tilde{0}$ and $-\sqrt{\delta t}$ for $\tilde{1}$ so that $\delta\tilde{W}^2 = \delta t$. In the limit $\theta = \pi/4$ it follows that $\delta\tilde{W} = \tilde{\eta}$. However, in contrast to the diffusive case, the average over measurement outcomes is

$$\langle\delta\tilde{W}\rangle_{\mathrm{ms}} = \sin(2\theta)\delta t\langle\tilde{c}+\tilde{c}^\dagger\rangle + \cos(2\theta)\sqrt{\delta t} \tag{A.9}$$

as follows from Eq. (A.5). We therefore do not recover a vanishing average as usually expected for Wiener increments.

Alternatively, one could also use a Poissonian variable with outcomes 0 and 1 according to the outcomes $\tilde{0}$ and $\tilde{1}$.

Away from the limit above, for small θ on the other hand, we again obtain a jump-type stochastic equation defined as

$$\delta\rho_s\left(\tilde{\xi}\right) = \delta t\mathcal{L}\rho_s + \left(\tilde{\xi} - \left\langle\left(\sqrt{\delta t}\tilde{c}^\dagger - \theta\right)\left(\sqrt{\delta t}\tilde{c} - \theta\right)\right\rangle\right)\left(\frac{\left(\sqrt{\delta t}\tilde{c} - \theta\right)\rho_s\left(\sqrt{\delta t}\tilde{c}^\dagger - \theta\right)}{\left\langle\left(\sqrt{\delta t}\tilde{c}^\dagger - \theta\right)\left(\sqrt{\delta t}\tilde{c} - \theta\right)\right\rangle} - \rho_s\right), \tag{A.10}$$

where we see that the jump operator gets a correction of order θ after expanding sin and cos. Here, terms of order $\theta^2\sqrt{\delta t}$ were neglected, effectively treating θ as being of the same order as $\sqrt{\delta t}$. The outcome $\tilde{\xi} = 1$ appears with probability $\left\langle\left(\sqrt{\delta t}\tilde{c}^\dagger - \theta\right)\left(\sqrt{\delta t}\tilde{c} - \theta\right)\right\rangle$, therefore scaling with $\delta t \approx \theta^2 \approx \sqrt{\delta t}\theta$ as for the jump-type SME in the main text, see Eq. (2.19).

These equations bear similarities with the derivation of diffusive equations from the jump-type evolutions, see Ref. [26, 217] for details. It remains to be examined if it is possible to unify both limits into a single stochastic equation that naturally recovers both limits presented in this appendix and the main text.

Appendix B

Steering by entanglement swapping

In this appendix, additional results and explanations complementing Chapter 4 are presented. Firstly, a summary of possible coupling sets used for the steering Hamiltonian is given. Then, Appendix C from Ref. [22] is reproduced, showing explicit results and formulae used for the numerical calculations presented in the main text. Finally, going beyond the results of Ref. [22], the exact form of the Kraus operators and the corresponding time-evolution of the system state together with the consequences for the cost-function calculation are derived. In this way, it is possible to go away from the restriction of the weak measurement limit used in Ref. [22]. We also show the QSM corresponding to a few of the used steering couplings for $N = 2$ qubits as an illustration of the present dynamics.

B.1 Coupling sets

Throughout this thesis, the coupling Hamiltonian $H_{n,K_n} = s_n J_n \sigma_n^{\alpha_n} \tau_n^{\beta_n}$ is considered with $s_n = \pm$ and $\alpha_n, \beta_n = 0, x, y, z$. However, not all of these possible values give different evolutions, and not all are necessary to allow for the preparation of certain target states.

For the steering process, the coupling set plays a significant role since it determines what kind of dynamics are allowed for the system state. In our simulations, we considered different coupling sets which can be classified as follows:

$$\begin{aligned}
\mathcal{K}_3 &= \{s_n = +,\, \alpha_n = x, y, z,\, \beta_n = x\}, & \mathcal{K}_4 &= \{s_n = +,\, \alpha_n = 0, x, y, z,\, \beta_n = x\},\\
\mathcal{K}_6 &= \{s_n = +,\, \alpha_n = x, y, z,\, \beta_n = x, z\}, & \mathcal{K}_7 &= \{s_n = +,\, \alpha_n = 0, x, y, z,\, \beta_n = x, z\},\\
\mathcal{K}_8 &= \{s_n = +,\, \alpha_n = 0, x, y, z,\, \beta_n = x, y\}, & \mathcal{K}_9 &= \{s_n = \pm,\, \alpha_n = x, y, z,\, \beta_n = x, z\},\\
\mathcal{K}_{10} &= \{s_n = \pm,\, \alpha_n = 0, x, y, z,\, \beta_n = x, z\}, & \mathcal{K}_{11} &= \{s_n = +,\, \alpha_n = 0, x, y, z,\, \beta_n = x, y, z\},\\
\mathcal{K}_{12} &= \{s_n = \pm,\, \alpha_n = x, y, z,\, \beta_n = x, y, z\}, & \mathcal{K}_{14} &= \{s_n = \pm,\, \alpha_n = 0, x, y, z,\, \beta_n = x, y, z\}
\end{aligned} \tag{B.1}$$

Note that $(+, \alpha_n, x/y)$ and $(-, \alpha_n, x/y)$ always give the same Kraus operators up to global phases

and suitable transformations $\eta \to -\eta$, so that only one of these choices needs to be considered. Also, the coupling $(\pm, 0, z)$ can be dropped altogether since it does not contribute to the dynamics in any way. Therefore, the subscript of the coupling families in fact corresponds to the number of couplings per system detector qubit pair.

Additionally, coupling sets with $\beta = x$ or $\beta = x, z$ give the same dynamics as when allowing $\beta = y$ or $\beta = y, z$ instead.

In Ref. [22] shown in Chapter 4 we used $\mathcal{K}_9$ for the preparation of GHZ states and $\mathcal{K}_{12}$ for the W state, since they showed the best numerical performance. In particular, increasing the size of the coupling set increases the numerical cost of the decision-making process.

Ref. [24] and Chapter 6 used $\mathcal{K}_6$ to reduce possible *frustration* by having an unnecessarily large coupling set, i.e., when the decision making has too many possible options to make a correct directed decision, therefore getting stuck.

The code used to run the simulations presented in this work can be found on GitHub and includes all the presented coupling sets. See the list of publications.

B.2 Bloch tensor changes

We here provide explicit expressions for $\langle dR_{\mathcal{S}}^2 \rangle_{\mathrm{ms}}$, where the string operator $\mathcal{S}$ in Eq. (4.19) is parametrized in terms of the N indices $\mu_j \in \{0, 1, 2, 3\}$. The corresponding expressions for RDMs needed in Eq. (4.37) follow by setting $\mu_j = 0$ for all traced-out qubits, cf. Sec. 4.2.2.

Assuming that steering operators and measurements are applied to the qubit pair $(n, n+1)$, we first specify the measurement-conditioned change $dR_{\mathcal{S}}$ of the rank-N Bloch tensor in one step, see Eq. (4.23). From Eq. (4.17) with $\alpha, \alpha' \in \{1, 2, 3\}$, we find

$$\begin{aligned} dR_{\mathcal{S}} &= -2 \sum_{m=n,n+1} \sum_{\alpha \neq \alpha_m} \left(s_m J_m \delta t \, \delta_{\beta_m, z} \sum_{\alpha'} \varepsilon_{\alpha_m \alpha \alpha'} + \Gamma_m \frac{\xi}{\langle c_\eta^\dagger c_\eta \rangle} \delta_{\beta_m, \perp} \right) \delta_{\mu_m, \alpha} \, R_{\mathcal{S}} \\ &+ 2\eta \sqrt{\Gamma_n \Gamma_{n+1}} \delta_{\beta_n, x} \delta_{\beta_{n+1}, x} \left(\frac{\xi}{\langle c_\eta^\dagger c_\eta \rangle} \left(\mathcal{F}_{\mathcal{S}} - Q_{n,n+1} R_{\mathcal{S}} \right) - \delta t \left(H_{\mathcal{S}} - Q_{n,n+1} R_{\mathcal{S}} \right) \right), \end{aligned} \tag{B.2}$$

with $\langle c_\eta^\dagger c_\eta \rangle$ in Eq. (4.13). For simplicity, Eq. (B.2) assumes only steering operators with $\beta_m \neq y$. However, the final results, Eqs. (4.24) and (B.6), are specified for the general case. The correlator (4.14) is encoded by

$$Q_{n,n+1} = Q_{n,n+1}^{\alpha_1, \alpha_2} = R_{0,\ldots,0,\alpha_n,\alpha_{n+1},0,\ldots,0}, \tag{B.3}$$

and the rank-N tensors $\mathcal{F}_{\mathcal{S}}$ and $H_{\mathcal{S}}$ in Eq. (B.2) are given by

$$\begin{aligned} \mathcal{F}_{\mathcal{S}} &= \frac{1}{2^{N+1}} \sum_{\mathcal{S}'} R_{\mathcal{S}'} \mathrm{Tr} \left((\sigma_n^{\alpha_n} \mathcal{S}' \sigma_{n+1}^{\alpha_{n+1}} + \sigma_{n+1}^{\alpha_{n+1}} \mathcal{S}' \sigma_n^{\alpha_n}) \mathcal{S} \right), \\ H_{\mathcal{S}} &= \frac{1}{2^{N+1}} \sum_{\mathcal{S}'} R_{\mathcal{S}'} \mathrm{Tr} \left(\{ \sigma_n^{\alpha_n} \sigma_{n+1}^{\alpha_{n+1}}, \mathcal{S}' \} \mathcal{S} \right). \end{aligned} \tag{B.4}$$

Since only tensor components involving the indices μ_n or μ_{n+1} are affected, we write $\mathcal{F}_{\mu_n,\mu_{n+1}}$ as shorthand for $\mathcal{F}_\mathcal{S}$, and similarly for $R_\mathcal{S}$ and $H_\mathcal{S}$, that is, unchanged indices $\mu_1,\ldots,\mu_{n-1}$ and $\mu_{n+2},\ldots,\mu_N$ are kept implicit. The non-vanishing matrix elements of $\mathcal{F}_\mathcal{S}$ are given by

$$\begin{aligned} \mathcal{F}_{0,0} &= R_{\alpha_n,\alpha_{n+1}}, \quad \mathcal{F}_{\alpha_n,\alpha_{n+1}} = R_{0,0}, \\ \mathcal{F}_{\alpha_n,0} &= R_{0,\alpha_{n+1}}, \quad \mathcal{F}_{0,\alpha_{n+1}} = R_{\alpha_n,0}, \\ \mathcal{F}_{\alpha\neq\alpha_n,\alpha'\neq\alpha_{n+1}} &= \sum_{\tilde\alpha,\tilde\alpha'} \varepsilon_{\alpha_n,\alpha,\tilde\alpha}\,\varepsilon_{\alpha_{n+1},\alpha',\tilde\alpha'}\,R_{\tilde\alpha,\tilde\alpha'}. \end{aligned} \tag{B.5}$$

Similarly, $H_\mathcal{S} = \mathcal{F}_\mathcal{S}$ except for a sign change in the last line of Eq. (B.5), $H_{\alpha,\alpha'} = -\mathcal{F}_{\alpha,\alpha'}$.

Taking the average over measurement outcomes in Eq. (B.2), we arrive at Eq. (4.24). Next we compute $\langle dR_\mathcal{S}^2\rangle_\mathrm{ms}$ from Eq. (B.2). Recalling that $\xi^2 = \xi$, only the contribution $\propto \xi$ can generate a contribution to leading order in δt. We therefore obtain

$$\frac{1}{2}\langle dR_\mathcal{S}^2\rangle_\mathrm{ms} = \delta t \sum_{\eta=\pm} \frac{G_\mathcal{S}^{(\eta)2}}{\langle c_\eta^\dagger c_\eta\rangle}, \tag{B.6}$$

with

$$\begin{aligned} G_\mathcal{S}^{(\eta=\pm)} &= -\sum_{m=n,n+1}\sum_{\alpha\neq\alpha_m} \Gamma_m \delta_{\beta_m,\perp}\delta_{\mu_m,\alpha} R_\mathcal{S} + \\ &+ \eta\sqrt{\Gamma_n\Gamma_{n+1}}(\delta_{\beta_n,x}\delta_{\beta_{n+1},x} + \delta_{\beta_n,y}\delta_{\beta_{n+1},y})\left(\mathcal{F}_\mathcal{S} - Q_{n,n+1}R_\mathcal{S}\right). \end{aligned}$$

We note that the denominator in Eq. (B.6) may vanish in special cases (for instance, if $\beta_n = \beta_{n+1} = z$), but then the numerator will also vanish and $G_\mathcal{S}^{(\eta)} = 0$. Similarly, for $\Gamma_n = \Gamma_{n+1}$ and $|Q_{n,n+1}| = 1$, one of the two ratios in Eq. (B.6) is of "0/0" type. However, the final result is well-defined and finite.

To give an example, let us consider the case $N = 3$, with qubits $(1, 2)$ being steered. Here, a contribution from qubit 3 to the expected single-qubit RDM cost function change can be present. We call this term $\langle dC_1^{(3)}(K)\rangle_\mathrm{ms}$, which is due to the subset $\mathcal{M} = \{3\}$ and comes exclusively from Eq. (B.6). We note that Eq. (B.7), together with $\mathcal{F}_{0,0,\mu} = R_{\alpha_1,\alpha_2,\mu}$, see Eq. (B.4), yields

$$\begin{aligned} \langle dC_1^{(3)}(K)\rangle_\mathrm{ms} &= \sum_{\mu=0}^{3} \frac{\langle dR_{0,0,\mu}^2\rangle_\mathrm{ms}}{4} \\ &= (\delta_{\beta_1,x}\delta_{\beta_2,x} + \delta_{\beta_1,y}\delta_{\beta_2,y})\frac{\Gamma_1\Gamma_2(\Gamma_1+\Gamma_2)\delta t}{(\Gamma_1+\Gamma_2)^2 - 4\Gamma_1\Gamma_2 Q_{1,2}^2}\sum_\alpha (R_{\alpha_1,\alpha_2,\alpha} - Q_{1,2}R_{0,0,\alpha})^2 \end{aligned}$$

where the $\mu = 0$ term does not contribute because of $\mathcal{F}_{0,0,0} - Q_{1,2}R_{0,0,0} = Q_{1,2} - Q_{1,2} = 0$. Note that $R_{0,0,\alpha}$ is the respective component of the Bloch vector for qubit 3, while $R_{\alpha_1,\alpha_2,\alpha}$ encodes the entanglement between qubit 3 and the other qubits. We conclude that the expected changes $\overline{dC_r(K)}$ of local cost functions ($r < N$) are capable of detecting entanglement features outside

the reach of fidelity-based cost functions.

B.3 Exact calculations

We now want to compute the exact form of the Kraus operators (4.8) used in Chapter 4, going beyond the previously used weak measurement limit.

Firstly, we note that since $H_{n,K_n} = s_n J_n \sigma_n^{\alpha_n} \tau_n^{\beta_n}$ we can write the time evolution operator in exact form as

$$e^{-i\delta t H_{n,K_n}} = \cos(J_n \delta t) - i s_n \sin(J_n \delta t) \sigma_n^{\alpha_n} \tau_n^{\beta_n}. \tag{B.7}$$

With this expression, we can introduce the single qubit Kraus operators $A_\xi^{(n)} = {}_d\langle \xi | e^{-i\delta t H_{n,K_n}} |0\rangle_d$ which are given as

$$A_0^{(n)} = \cos(J_n \delta t) - i s_n \sin(J_n \delta t) \sigma_n^{\alpha_n} \delta_{\beta_n, z}, \quad A_1^{(n)} = -i s_n \sin(J_n \delta t) \sigma_n^{\alpha_n} \delta^{(c)}_{\beta_n, \perp}, \tag{B.8}$$

with $\delta^{(c)}_{\beta_n,\perp}$ from Eq. (4.10), so that the two-qubit Kraus operators are obtained to be $A_{\xi,\eta} = {}_d\langle \Phi_{\xi,\eta} | e^{-i\delta t H_{n,K_n}} e^{-i\delta t H_{n+1,K_{n+1}}} |00\rangle_d = \frac{1}{\sqrt{2}} \left(A_0^{(n)} A_\xi^{(n+1)} + \eta A_1^{(n)} A_{1-\xi}^{(n+1)} \right)$.

We want to give the explicit expressions for two different coupling cases. First, for $\beta_n = z$ and arbitrary β_{n+1} we have

$$A_{\xi,\pm} = \frac{1}{\sqrt{2}} A_0^{(n)} \left(\delta_{\xi,0} A_0^{(n+1)} + \delta_{\xi,1} A_1^{(n+1)} \right), \quad P_{\xi,\pm} = \frac{1}{2} \left(\delta_{\xi,0} + (\delta_{\xi,1} - \delta_{\xi,0}) \sin^2(J_{n+1}\delta t) \delta_{\beta_{n+1},\perp} \right). \tag{B.9}$$

The Kraus operators for $\beta_{n+1} = z$ and arbitrary β_n follow by interchanging $n \leftrightarrow n+1$.

For $\beta_n, \beta_{n+1} \in \{x, y\}$ the Kraus operators take fundamentally different forms, since they can now induce entanglement due to the entanglement swapping measurements. They are given as

$$A_{0,\eta} = \frac{1}{\sqrt{2}} \left(\cos(J_n \delta t) \cos(J_{n+1} \delta t) - \eta s_n s_{n+1} \sin(J_n \delta t) \sin(J_{n+1} \delta t) \delta^{(c)}_{\beta_n,\perp} \delta^{(c)}_{\beta_{n+1},\perp} \sigma_n^{\alpha_n} \sigma_{n+1}^{\alpha_{n+1}} \right), \tag{B.10}$$

$$A_{1,\eta} = -\frac{i}{\sqrt{2}} \left(\eta s_n \sin(J_n \delta t) \cos(J_{n+1} \delta t) \delta^{(c)}_{\beta_n,\perp} \sigma_n^{\alpha_n} + s_{n+1} \cos(J_n \delta t) \sin(J_{n+1} \delta t) \delta^{(c)}_{\beta_{n+1},\perp} \sigma_{n+1}^{\alpha_{n+1}} \right), \tag{B.11}$$

with corresponding probabilities

$$\begin{aligned} P_{0,\eta} = \frac{1}{2} \Big(& 1 - \sin^2(J_n \delta t) \cos^2(J_{n+1} \delta t) - \cos^2(J_n \delta t) \sin^2(J_{n+1} \delta t) \\ & - \frac{\eta}{2} s_n s_{n+1} \sin(2 J_n \delta t) \sin(2 J_{n+1} \delta t) \left(\delta_{\beta_n, x} \delta_{\beta_{n+1}, x} - \delta_{\beta_n, y} \delta_{\beta_{n+1}, y} \right) Q_{n,n+1}^{\alpha_n, \alpha_{n+1}} \Big), \end{aligned} \tag{B.12}$$

$$\begin{aligned} P_{1,\eta} = \frac{1}{2} \Big(& \sin^2(J_n \delta t) \cos^2(J_{n+1} \delta t) + \cos^2(J_n \delta t) \sin^2(J_{n+1} \delta t) \\ & + \frac{\eta}{2} s_n s_{n+1} \sin(2 J_n \delta t) \sin(2 J_{n+1} \delta t) \left(\delta_{\beta_n, x} \delta_{\beta_{n+1}, x} + \delta_{\beta_n, y} \delta_{\beta_{n+1}, y} \right) Q_{n,n+1}^{\alpha_n, \alpha_{n+1}} \Big). \end{aligned} \tag{B.13}$$

Note, that for $\beta_n = \beta_{n+1} = y$ we obtain an effective transformation of the "no-click" Kraus operators $A_{0,+} \leftrightarrow A_{0,-}$. This detail was omitted in Ref. [22] and correspondingly in Chapter 4 for clarity since it does not change the evolution as long as the correct probabilities are applied to the corresponding Kraus operators.

For the decision making, the cost-function change needs to be computed in the exact form. For this, we note that the average over measurement outcomes yields

$$\langle \rho(t+\delta t)\rangle_{\mathrm{ms}} = \sum_{\xi,\xi'=0,1} A_{\xi'}^{(n+1)} A_{\xi}^{(n)} \rho(t) A_{\xi}^{(n)\dagger} A_{\xi'}^{(n+1)\dagger} \tag{B.14}$$

with the single qubit Kraus operators from Eq. (B.8).

In the Bloch tensor representation we obtain $\langle \Delta R_{\mathcal{S}}\rangle_{\mathrm{ms}} = \mathrm{Tr}\Big(\left(\langle \rho(t+\delta t)\rangle_{\mathrm{ms}} - \rho(t)\right) \mathcal{S}\Big)$ as

$$\begin{aligned}
\langle \Delta R_{\mathcal{S}}\rangle_{\mathrm{ms}} = -2 \sum_{m=n,n+1} \sum_{\alpha\neq\alpha_m} \Big(& s_m \sin(J_m\delta t)\cos(J_m\delta t)\,\delta_{\beta_m,z} \\
& \sum_{\alpha'} \varepsilon_{\alpha_m\alpha\alpha'}\delta_{\mu_m,\alpha} R_{\mathcal{S}} \left(1 - 2\sin^2(J_{\overline{m}}\delta t)(1-\delta_{\mu_{\overline{m}},0} - \delta_{\mu_{\overline{m}},\alpha_{\overline{m}}})\right) + \\
& + \sin^2(J_m\delta t)\delta_{\mu_m,\alpha} R_{\mathcal{S}} \left(1 - \sin^2(J_{\overline{m}}\delta t)(1-\delta_{\mu_{\overline{m}},0} - \delta_{\mu_{\overline{m}},\alpha_{\overline{m}}})\right)\Big) \\
& + s_n s_{n+1} \sin(2J_n\delta t)\sin(2J_{n+1}\delta t)\delta_{\beta_n,z}\delta_{\beta_{n+1},z} \sum_{\alpha',\alpha''} \varepsilon_{\alpha_n\alpha\alpha'}\delta_{\mu_n,\alpha}\varepsilon_{\alpha_{n+1}\tilde{\alpha}\alpha''}\delta_{\mu_{n+1},\tilde{\alpha}} R_{\mathcal{S}}
\end{aligned} \tag{B.15}$$

where $\overline{m}$ is equal to $n+1$ (n) for $m = n$ ($m = n+1$). This equation gives the generalization of Eq. (4.24), where we note that here the term containing $\sin^2(J_m\delta t)$ is now also present for $\beta = z$.

The second-order term in Eq. (4.37) is not relevant for $\beta_n = z$ or $\beta_{n+1} = z$ since in this case, as seen above, the Kraus operators are decoupled for both steered qubits and do not induce entanglement. In this case it holds that $\sum_{\mathcal{S}} \Delta R_{\mathcal{S}}^2 = -2\sum_{\mathcal{S}} \Delta R_{\mathcal{S}} \times R_{\mathcal{S}}$, canceling the term without dependence on $R_{\mathcal{S}}^f$ for both the local and global terms in the cost function. For other couplings, this term can be obtained by an analogous calculation as in the weak-measurement limit.

B.4 Quantum state machine

Here we show the QSM encoding the steering transitions acting on system qubits as introduced in Chapter 3. It can be used as a navigation tool for active steering decisions instead of the cost-function approach, see Ref. [18] and Chapter 3.2.1, and can also be used to visualize the dynamics corresponding to different couplings and measurement outcomes.

We consider the coupling set $\mathcal{K}_3$ and restrict the diagram to $\alpha_1 = \alpha_2$ for simplicity. The "click" transitions corresponding to the Kraus operators $A_{1,\eta}$ are visualized in Fig. B.1. The "no click" transitions can then be constructed directly from this diagram, see Chapter 3.2.1.

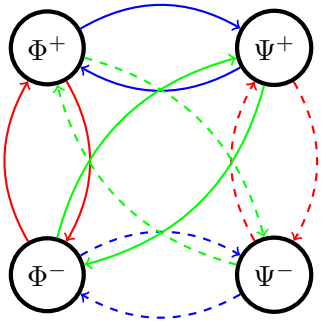

Figure B.1: QSM representing the transitions between the four Bell states of the system. "Click" measurements for $\beta_1 = \beta_2 = x$ corresponding to Kraus operators A_{Ψ^+} (solid) and A_{Ψ^-} (dotted) for the three possibilities of choosing $\alpha_i = x$ (blue), y (green) and z (red). The corresponding "no click" diagram follows in the usual way, see [18], and only contains self-loops. However, for each choice of α_i two self-loops have a bigger transition amplitude, leading to an effective *leakage* from one subspace into the other under renormalization.

We see that once the state is in one of the Bell states, each coupling gives exactly one possible transition to one of the other possible Bell states. However, if the system is in a product state and therefore a perfect superposition of two even or odd Bell states, a transition into the opposing parity sector is necessary in order to remove this superposition, preparing an entangled state. This is in fact also illustrated by the numerical results in Chapter 4, showing that when starting in the state $|00\rangle$, initially an opposing Bell state is prepared, before another "click" takes the system into the target state $|\text{Bell}\rangle$, see Fig. 4.3.

This illustrates the possibilities of using QSMs for active decision making as well as aiding in the analysis of system dynamics.

List of publications

Here, the publications that have been used as the basis for this thesis will be listed, explaining the author's contribution to each.

Engineering unsteerable quantum states with active feedback

Contribution: Main author, main preliminary scientific work, calculation of time evolution, checks and corrections for all other calculations, identification of trapped state problem, data acquisition through numerical simulations and data management, contribution to the writing of the manuscript, preparation of all figures, preparation of a Python version of the original Fortran code.

The data used to create the figures can be found on Zenodo at https://zenodo.org/records/10605186. The code that reproduces the shown results can be found on GitHub at https://github.com/Sammor13/Act_Ent_Swap_steering.

Reference: S. Morales, Y. Gefen, I. Gornyi, A. Zazunov, and R. Egger, *Engineering unsteerable quantum states with active feedback*, Phys. Rev. Research **6**, 013244 (2024)

Error threshold in active steering protocols for few-qubit systems

Contribution: Second main author, assisting in scientific work through discussions, calculations and programming, partly data acquisition through numerical simulations and data management, preparation of Fig. 5.2 and modification of Fig. 1 in the published version, identification of a scaling mistake in Γ_C, contribution to the writing of the manuscript.

The data used to create the figures can be found on Zenodo at https://zenodo.org/records/11581356.

Reference: N. Ackermann, S. Morales, A. Levy Yeyati, S. Diehl, and R. Egger, *Error threshold in active steering protocols for few-qubit systems*, Phys. Rev. Research **7**, 013045 (2025)

Towards scalable active steering protocols for genuinely entangled state manifolds

Contribution: Main author, main scientific work, calculating all analytical results, programming, data acquisition through numerical simulations and data management, contribution to the writing

of the manuscript, preparation of all figures.

The data used to create the figures can be found on Zenodo at https://zenodo.org/records/14277545. The code can be found on GitHub at https://github.com/Sammor13/QFI_steering.

Reference: S. Morales, S. Pappalardi, and R. Egger, *Towards scalable active steering protocols for genuinely entangled state manifolds*, arXiv:2412.04168

Bibliography

[1] M. Fisher, V. Khemani, A. Nahum, and S. Vijay, "Random Quantum Circuits," *Annual Review of Condensed Matter Physics*, vol. 14, no. 1, pp. 335–379, 2023.

[2] J. M. Koh, S.-N. Sun, M. Motta, and A. J. Minnich, "Measurement-induced entanglement phase transition on a superconducting quantum processor with mid-circuit readout," *Nature Physics*, vol. 19, p. 1314, 2023.

[3] Google Quantum AI and Collaborators, "Measurement-induced entanglement and teleportation on a noisy quantum processor," *Nature*, vol. 622, p. 481, 2023.

[4] C. Noel et al., "Measurement-induced quantum phases realized in a trapped-ion quantum computer," *Nature Physics*, vol. 18, p. 760, 2022.

[5] T. Müller, S. Diehl, and M. Buchhold, "Measurement-induced dark state phase transitions in long-ranged fermion systems," *Physical Review Letters*, vol. 128, no. 1, Jan. 2022.

[6] M. Cerezo et al., "Variational quantum algorithms," *Nature Reviews Physics*, vol. 3, no. 9, pp. 625–644, Aug. 2021.

[7] V. Giovannetti, S. Lloyd, and L. Maccone, "Advances in quantum metrology," *Nature Photonics*, vol. 5, no. 4, pp. 222–229, Mar. 2011.

[8] B. M. Terhal, "Quantum error correction for quantum memories," *Rev. Mod. Phys.*, vol. 87, pp. 307–346, 2 Apr. 2015.

[9] R. Acharya et al., "Quantum error correction below the surface code threshold," *Nature*, vol. 638, no. 8052, pp. 920–926, Dec. 2024.

[10] A. Matthies, M. Rudner, A. Rosch, and E. Berg, "Programmable adiabatic demagnetization for systems with trivial and topological excitations," *Quantum*, vol. 8, p. 1505, Oct. 2024.

[11] M. Gau, R. Egger, A. Zazunov, and Y. Gefen, "Driven Dissipative Majorana Dark Spaces," *Phys. Rev. Lett.*, vol. 125, p. 147 701, 14 Oct. 2020.

[12] M. Gau, R. Egger, A. Zazunov, and Y. Gefen, "Towards dark space stabilization and manipulation in driven dissipative Majorana platforms," *Phys. Rev. B*, vol. 102, p. 134 501, 13 Oct. 2020.

[13] F. Ticozzi and L. Viola, "Stabilizing entangled states with quasi-local quantum dynamical semigroups," *Philosophical Transactions of the Royal Society A: Mathematical, Physical and Engineering Sciences*, vol. 370, no. 1979, pp. 5259–5269, 2012.

[14] S. Roy, J. T. Chalker, I. V. Gornyi, and Y. Gefen, "Measurement-induced steering of quantum systems," *Phys. Rev. Res.*, vol. 2, p. 033 347, 3 Sep. 2020.

[15] A. Bermudez et al., "Assessing the Progress of Trapped-Ion Processors Towards Fault-Tolerant Quantum Computation," *Phys. Rev. X*, vol. 7, p. 041 061, 4 Dec. 2017.

[16] F. Arute et al., "Quantum supremacy using a programmable superconducting processor," *Nature*, vol. 574, p. 505, 2019.

[17] C. Janvier et al., "Coherent manipulation of Andreev states in superconducting atomic contacts," *Science*, vol. 349, no. 6253, pp. 1199–1202, 2015.

[18] Y. Herasymenko, I. Gornyi, and Y. Gefen, "Measurement-Driven Navigation in Many-Body Hilbert Space: Active-Decision Steering," *PRX Quantum*, vol. 4, p. 020 347, 2 Jun. 2023.

[19] J. Biamonte, P. Wittek, N. Pancotti, P. Rebentrost, N. Wiebe, and S. Lloyd, "Quantum machine learning," *Nature*, vol. 549, p. 195, 2017.

[20] V. V. Sivak, A. Eickbusch, H. Liu, B. Royer, I. Tsioutsios, and M. H. Devoret, "Model-Free Quantum Control with Reinforcement Learning," *Phys. Rev. X*, vol. 12, p. 011 059, 1 Mar. 2022.

[21] T. A. Brun, "A simple model of quantum trajectories," *American Journal of Physics*, vol. 70, no. 7, pp. 719–737, Jun. 2002.

[22] S. Morales, Y. Gefen, I. Gornyi, A. Zazunov, and R. Egger, "Engineering unsteerable quantum states with active feedback," *Phys. Rev. Res.*, vol. 6, p. 013 244, 1 Mar. 2024.

[23] N. Ackermann, S. Morales, A. L. Yeyati, S. Diehl, and R. Egger, "Error threshold in active steering protocols for few-qubit systems," *Phys. Rev. Res.*, vol. 7, p. 013 045, 1 Jan. 2025.

[24] S. Morales, S. Pappalardi, and R. Egger, *Towards scalable active steering protocols for genuinely entangled state manifolds*, 2024. arXiv: `2412.04168 [quant-ph]`.

[25] H. P. Breuer and F. Petruccione, *The theory of open quantum systems*. Oxford University Press, Oxford, UK, 2002.

[26] H. M. Wiseman and G. J. Milburn, *Quantum measurements and control*. Cambridge University Press, Cambridge, UK, 2010.

[27] U. Weiss, *Quantum Dissipative Systems (Fourth Edition)*. World Scientific Publishing Company, 2012.

[28] V. V. Albert and L. Jiang, "Symmetries and conserved quantities in lindblad master equations," *Physical Review A*, vol. 89, no. 2, Feb. 2014.

[29] M. A. Nielsen and I. L. Chuang, *Quantum Computation and Quantum Information*. Cambridge University Press, Cambridge, UK, 2000.

[30] H. J. Carmichael, "Stochastic schrödinger equations: What they mean and what they can do," in *Coherence and Quantum Optics VII*, J. H. Eberly, L. Mandel, and E. Wolf, Eds., Boston, MA: Springer US, 1996, pp. 177–192.

[31] K. Jacobs and D. A. Steck, "A straightforward introduction to continuous quantum measurement," *Contemporary Physics*, vol. 47, no. 5, pp. 279–303, 2006.

[32] E. Medina-Guerra, P. Kumar, I. V. Gornyi, and Y. Gefen, "Quantum state engineering by steering in the presence of errors," *Phys. Rev. Res.*, vol. 6, p. 023 159, 2 May 2024.

[33] R. Horodecki, P. Horodecki, M. Horodecki, and K. Horodecki, "Quantum entanglement," *Rev. Mod. Phys.*, vol. 81, pp. 865–942, 2 Jun. 2009.

[34] Y. Aharonov, D. Z. Albert, and L. Vaidman, "How the result of a measurement of a component of the spin of a spin-1/2 particle can turn out to be 100," *Phys. Rev. Lett.*, vol. 60, pp. 1351–1354, 14 Apr. 1988.

[35] A. Romito, Y. Gefen, and Y. M. Blanter, "Weak values of electron spin in a double quantum dot," *Physical Review Letters*, vol. 100, no. 5, Feb. 2008.

[36] E. Schrödinger, "Discussion of probability relations between separated systems," *Mathematical Proceedings of the Cambridge Philosophical Society*, vol. 31, no. 4, pp. 555–563, 1935.

[37] R. Uola, A. C. S. Costa, H. C. Nguyen, and O. Gühne, "Quantum steering," *Rev. Mod. Phys.*, vol. 92, p. 015 001, 1 Mar. 2020.

[38] H. M. Wiseman, S. J. Jones, and A. C. Doherty, "Steering, entanglement, nonlocality, and the Einstein-Podolsky-Rosen paradox," *Phys. Rev. Lett.*, vol. 98, p. 140 402, 14 Apr. 2007.

[39] D. P. DiVincenzo, *Topics in quantum computers*, 1996. arXiv: `cond-mat/9612126 [cond-mat.mes-hall]`.

[40] J. Langbehn, K. Snizhko, I. Gornyi, G. Morigi, Y. Gefen, and C. P. Koch, "Dilute measurement-induced cooling into many-body ground states," *PRX Quantum*, vol. 5, no. 3, Jul. 2024.

[41] P. Kumar, K. Snizhko, and Y. Gefen, "Engineering two-qubit mixed states with weak measurements," *Phys. Rev. Res.*, vol. 2, p. 042 014, 4 Oct. 2020.

[42] D. Volya and P. Mishra, "FL state preparation on quantum computers via quantum steering," *IEEE Transactions on Quantum Engineering*, pp. 1–14, 2024.

[43] Z. K. Minev et al., "To catch and reverse a quantum jump mid-flight," *Nature*, vol. 570, p. 200, 2019.

[44] K. J. Satzinger et al., "Realizing topologically ordered states on a quantum processor," *Science*, vol. 374, no. 6572, pp. 1237–1241, 2021.

[45] X. Mi et al., "Information scrambling in quantum circuits," *Science*, vol. 374, no. 6574, pp. 1479–1483, 2021.

[46] C. Monroe et al., "Programmable quantum simulations of spin systems with trapped ions," *Rev. Mod. Phys.*, vol. 93, p. 025 001, 2 Apr. 2021.

[47] Y. Wang, K. Snizhko, A. Romito, Y. Gefen, and K. Murch, "Observing a topological transition in weak-measurement-induced geometric phases," *Phys. Rev. Res.*, vol. 4, p. 023 179, 2 Jun. 2022.

[48] M. F. Ferrer-Garcia, K. Snizhko, A. D'Errico, A. Romito, Y. Gefen, and E. Karimi, "Topological transitions of the generalized pancharatnam-berry phase," *Science Advances*, vol. 9, no. 47, Nov. 2023.

[49] Y. Wang, K. Snizhko, A. Romito, Y. Gefen, and K. Murch, "Dissipative preparation and stabilization of many-body quantum states in a superconducting qutrit array," *Physical Review A*, vol. 108, no. 1, p. 013 712, Jul. 2023.

[50] X.-M. Zhang, T. Li, and X. Yuan, "Quantum State Preparation with Optimal Circuit Depth: Implementations and Applications," *Phys. Rev. Lett.*, vol. 129, p. 230 504, 23 Nov. 2022.

[51] I. M. Georgescu, S. Ashhab, and F. Nori, "Quantum simulation," *Rev. Mod. Phys.*, vol. 86, pp. 153–185, 1 Mar. 2014.

[52] W. Dür, G. Vidal, and J. I. Cirac, "Three qubits can be entangled in two inequivalent ways," *Phys. Rev. A*, vol. 62, p. 062 314, 6 Nov. 2000.

[53] C. P. Koch, "Controlling open quantum systems: Tools, achievements, and limitations," *Journal of Physics: Condensed Matter*, vol. 28, no. 21, p. 213 001, May 2016.

[54] X. Turkeshi, A. Biella, R. Fazio, M. Dalmonte, and M. Schiró, "Measurement-induced entanglement transitions in the quantum Ising chain: From infinite to zero clicks," *Phys. Rev. B*, vol. 103, p. 224 210, 22 Jun. 2021.

[55] P. M. Harrington, E. J. Mueller, and K. W. Murch, "Engineered dissipation for quantum information science," *Nature Reviews Physics*, vol. 4, p. 260, 2022.

[56] E. Chitambar and G. Gour, "Quantum resource theories," *Rev. Mod. Phys.*, vol. 91, p. 025 001, 2 Apr. 2019.

[57] C. L. Degen, F. Reinhard, and P. Cappellaro, "Quantum sensing," *Rev. Mod. Phys.*, vol. 89, p. 035 002, 3 Jul. 2017.

[58] S. Pirandola, B. R. Bardhan, T. Gehring, C. Weedbrook, and S. Lloyd, "Advances in photonic quantum sensing," *Nature Photonics*, vol. 12, p. 724, 2018.

[59] D. Riste et al., "Deterministic entanglement of superconducting qubits by parity measurement and feedback," *Nature*, vol. 502, p. 359, 2013.

[60] N. Roch et al., "Observation of Measurement-Induced Entanglement and Quantum Trajectories of Remote Superconducting Qubits," *Phys. Rev. Lett.*, vol. 112, p. 170 501, 17 Apr. 2014.

[61] A. Chantasri, M. E. Kimchi-Schwartz, N. Roch, I. Siddiqi, and A. N. Jordan, "Quantum Trajectories and Their Statistics for Remotely Entangled Quantum Bits," *Phys. Rev. X*, vol. 6, p. 041 052, 4 Dec. 2016.

[62] P. Blasiak, E. Borsuk, and M. Markiewicz, "Arbitrary entanglement of three qubits via linear optics," *Scientific Reports*, vol. 12, p. 21 596, 2022.

[63] H. J. Briegel and R. Raussendorf, "Persistent Entanglement in Arrays of Interacting Particles," *Phys. Rev. Lett.*, vol. 86, pp. 910–913, 5 Jan. 2001.

[64] B. Zeng, X. Chen, D.-L. Zhou, and X.-G. Wen, *Quantum information meets quantum matter*. Springer Verlag, New York, 2019.

[65] T.-C. Lu, L. A. Lessa, I. H. Kim, and T. H. Hsieh, "Measurement as a Shortcut to Long-Range Entangled Quantum Matter," *PRX Quantum*, vol. 3, p. 040 337, 4 Dec. 2022.

[66] N. Tantivasadakarn, R. Thorngren, A. Vishwanath, and R. Verresen, "Long-range entanglement from measuring symmetry-protected topological phases," *Physical Review X*, vol. 14, no. 2, Jun. 2024.

[67] R. Verresen, N. Tantivasadakarn, and A. Vishwanath, *Efficiently preparing Schrödinger's cat, fractons and non-Abelian topological order in quantum devices*, 2021. arXiv: 2112.03061.

[68] S. Bravyi, I. Kim, A. Kliesch, and R. Koenig, *Adaptive constant-depth circuits for manipulating non-abelian anyons*, 2022. arXiv: 2205.01933.

[69] A. Lavasani, Z.-X. Luo, and S. Vijay, "Monitored quantum dynamics and the Kitaev spin liquid," *Phys. Rev. B*, vol. 108, p. 115 135, 11 Sep. 2023.

[70] G.-Y. Zhu, N. Tantivasadakarn, A. Vishwanath, S. Trebst, and R. Verresen, "Nishimori's Cat: Stable Long-Range Entanglement from Finite-Depth Unitaries and Weak Measurements," *Phys. Rev. Lett.*, vol. 131, p. 200 201, 20 Nov. 2023.

[71] J. Y. Lee, W. Ji, Z. Bi, and M. P. A. Fisher, *Decoding Measurement-Prepared Quantum Phases and Transitions: from Ising model to gauge theory, and beyond*, 2022. arXiv: 2208.11699.

[72] N. Tantivasadakarn, A. Vishwanath, and R. Verresen, "Hierarchy of Topological Order From Finite-Depth Unitaries, Measurement, and Feedforward," *PRX Quantum*, vol. 4, p. 020 339, 2 Jun. 2023.

[73] K. C. Smith, E. Crane, N. Wiebe, and S. Girvin, "Deterministic Constant-Depth Preparation of the AKLT State on a Quantum Processor Using Fusion Measurements," *PRX Quantum*, vol. 4, p. 020 315, 2 Apr. 2023.

[74] Q. Liu, K. Ziegler, D. A. Kessler, and E. Barkai, "Driving quantum systems with periodic conditional measurements," *Phys. Rev. Res.*, vol. 4, p. 023 129, 2 May 2022.

[75] M. Buchhold, T. Müller, and S. Diehl, *Revealing measurement-induced phase transitions by pre-selection*, 2022. arXiv: 2208.10506.

[76] A. J. Friedman, O. Hart, and R. Nandkishore, "Measurement-Induced Phases of Matter Require Feedback," *PRX Quantum*, vol. 4, p. 040 309, 4 Oct. 2023.

[77] V. Ravindranath, Y. Han, Z.-C. Yang, and X. Chen, "Entanglement steering in adaptive circuits with feedback," *Phys. Rev. B*, vol. 108, p. L041103, 4 Jul. 2023.

[78] Y. Wu, J. Yao, and P. Zhang, "Preparing quantum states by measurement-feedback control with Bayesian optimization," *Frontiers of Physics*, vol. 18, no. 6, p. 61 301, Jul. 2023.

[79] J. Hauser, Y. Li, S. Vijay, and M. P. A. Fisher, "Continuous symmetry breaking in adaptive quantum dynamics," *Phys. Rev. B*, vol. 109, p. 214 305, 21 Jun. 2024.

[80] V. Ravindranath, Z.-C. Yang, and X. Chen, *Free fermions under adaptive quantum dynamics*, 2023. arXiv: 2306.16595 [quant-ph].

[81] D. Boschi, S. Branca, F. De Martini, L. Hardy, and S. Popescu, "Experimental Realization of Teleporting an Unknown Pure Quantum State via Dual Classical and Einstein-Podolsky-Rosen Channels," *Phys. Rev. Lett.*, vol. 80, pp. 1121–1125, 6 Feb. 1998.

[82] J.-W. Pan, D. Bouwmeester, H. Weinfurter, and A. Zeilinger, "Experimental Entanglement Swapping: Entangling Photons That Never Interacted," *Phys. Rev. Lett.*, vol. 80, pp. 3891–3894, 18 May 1998.

[83] T. Jennewein, G. Weihs, J.-W. Pan, and A. Zeilinger, "Experimental Nonlocality Proof of Quantum Teleportation and Entanglement Swapping," *Phys. Rev. Lett.*, vol. 88, p. 017 903, 1 Dec. 2001.

[84] H. de Riedmatten, I. Marcikic, J. A. W. van Houwelingen, W. Tittel, H. Zbinden, and N. Gisin, "Long-distance entanglement swapping with photons from separated sources," *Phys. Rev. A*, vol. 71, p. 050 302, 5 May 2005.

[85] M. Riebe et al., "Deterministic entanglement swapping with an ion-trap quantum computer," *Nature Physics*, vol. 4, p. 839, 2008.

[86] R. Kaltenbaek, R. Prevedel, M. Aspelmeyer, and A. Zeilinger, "High-fidelity entanglement swapping with fully independent sources," *Phys. Rev. A*, vol. 79, p. 040 302, 4 Apr. 2009.

[87] C.-X. Huang et al., "Entanglement Swapping and Quantum Correlations via Symmetric Joint Measurements," *Phys. Rev. Lett.*, vol. 129, p. 030 502, 3 Jul. 2022.

[88] C. K. Andersen et al., "Repeated quantum error detection in a surface code," *Nature Physics*, vol. 16, p. 875, 2020.

[89] R. Stricker et al., "Experimental deterministic correction of qubit loss," *Nature*, vol. 585, p. 207, 2020.

[90] L. Egan et al., "Fault-tolerant control of an error-corrected qubit," *Nature*, vol. 598, p. 281, 2021.

[91] C. Ryan-Anderson et al., "Realization of Real-Time Fault-Tolerant Quantum Error Correction," *Phys. Rev. X*, vol. 11, p. 041 058, 4 Dec. 2021.

[92] S. Krinner et al., "Realizing repeated quantum error correction in a distance-three surface code," *Nature*, vol. 605, p. 669, 2022.

[93] M. H. Abobeih et al., "Fault-tolerant operation of a logical qubit in a diamond quantum processor," *Nature*, vol. 606, p. 884, 2022.

[94] Y. Zhao et al., "Realization of an Error-Correcting Surface Code with Superconducting Qubits," *Phys. Rev. Lett.*, vol. 129, p. 030 501, 3 Jul. 2022.

[95] R. Acharya *et al.* and Google Quantum AI, "Suppressing quantum errors by scaling a surface code logical qubit," *Nature*, vol. 614, no. 7949, pp. 676–681, Feb. 2023.

[96] V. V. Sivak et al., "Real-time quantum error correction beyond break-even," *Nature*, vol. 616, p. 50, 2023.

[97] Z. Ni et al., "Beating the break-even point with a discrete-variable-encoded logical qubit," *Nature*, vol. 616, p. 56, 2023.

[98] P. W. Anderson, "Ground State of a Magnetic Impurity in a Metal," *Phys. Rev.*, vol. 164, pp. 352–359, 2 Dec. 1967.

[99] M. Cerezo, A. Sone, T. Volkoff, L. Cincio, and P. J. Coles, "Cost function dependent barren plateaus in shallow parametrized quantum circuits," *Nature Communications*, vol. 12, p. 1791, 2021.

[100] J. Zhang, Y. Liu, R.-B. Wu, K. Jacobs, and F. Nori, "Quantum feedback: Theory, experiments, and applications," *Physics Reports*, vol. 679, pp. 1–60, 2017.

[101] D. P. DiVincenzo, "Two-bit gates are universal for quantum computation," *Phys. Rev. A*, vol. 51, pp. 1015–1022, 2 Feb. 1995.

[102] S. Lloyd, "Almost any quantum logic gate is universal," *Phys. Rev. Lett.*, vol. 75, pp. 346–349, 2 Jul. 1995.

[103] I. Marvian, "Restrictions on realizable unitary operations imposed by symmetry and locality," *Nature Physics*, vol. 18, p. 283, 2022.

[104] O. Gamel, "Entangled Bloch spheres: Bloch matrix and two-qubit state space," *Phys. Rev. A*, vol. 93, p. 062 320, 6 Jun. 2016.

[105] J. Weidmann, *Linear operators in Hilbert spaces*. Springer Verlag, New York, 1980.

[106] M. Ehrgott, *Multicriteria Optimization*. Springer Verlag, Heidelberg, 2005.

[107] C. H. Bennett, H. J. Bernstein, S. Popescu, and B. Schumacher, "Concentrating partial entanglement by local operations," *Phys. Rev. A*, vol. 53, pp. 2046–2052, 4 Apr. 1996.

[108] S. Sang, Z. Li, T. H. Hsieh, and B. Yoshida, "Ultrafast entanglement dynamics in monitored quantum circuits," *PRX Quantum*, vol. 4, p. 040 332, 4 Nov. 2023.

[109] T. Nitsche et al., "Probing measurement-induced effects in quantum walks via recurrence," *Science Advances*, vol. 4, no. 6, Jun. 2018.

[110] Y. Guryanova, N. Friis, and M. Huber, "Ideal Projective Measurements Have Infinite Resource Costs," *Quantum*, vol. 4, p. 222, Jan. 2020.

[111] P. Magnard et al., "Fast and Unconditional All-Microwave Reset of a Superconducting Qubit," *Phys. Rev. Lett.*, vol. 121, p. 060 502, 6 Aug. 2018.

[112] A. Gyenis et al., "Experimental Realization of a Protected Superconducting Circuit Derived from the 0–π Qubit," *PRX Quantum*, vol. 2, p. 010 339, 1 Mar. 2021.

[113] A. Gyenis, A. Di Paolo, J. Koch, A. Blais, A. A. Houck, and D. I. Schuster, "Moving beyond the Transmon: Noise-Protected Superconducting Quantum Circuits," *PRX Quantum*, vol. 2, p. 030 101, 3 Sep. 2021.

[114] S. Plugge, A. Rasmussen, R. Egger, and K. Flensberg, "Majorana box qubits," *New Journal of Physics*, vol. 19, no. 1, p. 012 001, Jan. 2017.

[115] T. Karzig et al., "Scalable designs for quasiparticle-poisoning-protected topological quantum computation with Majorana zero modes," *Phys. Rev. B*, vol. 95, p. 235 305, 23 Jun. 2017.

[116] H.-Y. Huang, R. Kueng, and J. Preskill, "Predicting many properties of a quantum system from very few measurements," *Nature Physics*, vol. 16, p. 1050, 2020.

[117] M. Kliesch and I. Roth, "Theory of Quantum System Certification," *PRX Quantum*, vol. 2, p. 010 201, 1 Jan. 2021.

[118] H. C. Nguyen, J. L. Bönsel, J. Steinberg, and O. Gühne, "Optimizing Shadow Tomography with Generalized Measurements," *Phys. Rev. Lett.*, vol. 129, p. 220 502, 22 Nov. 2022.

[119] P. Zanardi and L. Campos Venuti, "Coherent Quantum Dynamics in Steady-State Manifolds of Strongly Dissipative Systems," *Phys. Rev. Lett.*, vol. 113, p. 240 406, 24 Dec. 2014.

[120] E. V. H. Doggen, Y. Gefen, I. V. Gornyi, A. D. Mirlin, and D. G. Polyakov, "Evolution of many-body systems under ancilla quantum measurements," *Phys. Rev. B*, vol. 107, p. 214 203, 21 Jun. 2023.

[121] J. Carrasquilla and G. Torlai, "How To Use Neural Networks To Investigate Quantum Many-Body Physics," *PRX Quantum*, vol. 2, p. 040 201, 4 Nov. 2021.

[122] T. Neupert, M. H. Fischer, E. Greplova, K. Choo, and M. M. Denner, *Introduction to Machine Learning for the Sciences*, 2022. arXiv: `2102.04883 [physics.comp-ph]`.

[123] D. A. Puente, F. Motzoi, T. Calarco, G. Morigi, and M. Rizzi, "Quantum state preparation via engineered ancilla resetting," *Quantum*, vol. 8, p. 1299, Mar. 2024.

[124] A. Blais, A. L. Grimsmo, S. M. Girvin, and A. Wallraff, "Circuit quantum electrodynamics," *Rev. Mod. Phys.*, vol. 93, p. 025 005, 2 May 2021.

[125] J. F. Kam, H. Kang, C. D. Hill, G. J. Mooney, and L. C. L. Hollenberg, "Characterization of entanglement on superconducting quantum computers of up to 414 qubits," *Physical Review Research*, vol. 6, no. 3, Aug. 2024.

[126] E. H. Chen et al., "Nishimori transition across the error threshold for constant-depth quantum circuits," *Nature Physics*, vol. 21, no. 1, pp. 161–167, Dec. 2024.

[127] B. Schumacher and M. A. Nielsen, "Quantum data processing and error correction," *Physical Review A*, vol. 54, no. 4, p. 2629, 1996.

[128] S. Lloyd, "Capacity of the noisy quantum channel," *Physical Review A*, vol. 55, no. 3, p. 1613, 1997.

[129] R. Fan, Y. Bao, E. Altman, and A. Vishwanath, "Diagnostics of Mixed-State Topological Order and Breakdown of Quantum Memory," *PRX Quantum*, vol. 5, p. 020 343, 2 May 2024.

[130] C.-E. Bardyn, L. Wawer, A. Altland, M. Fleischhauer, and S. Diehl, "Probing the Topology of Density Matrices," *Phys. Rev. X*, vol. 8, p. 011 035, 1 Feb. 2018.

[131] L. M. Sieberer, M. Buchhold, J. Marino, and S. Diehl, *Universality in driven open quantum matter*, 2023. arXiv: 2312.03073 [cond-mat.stat-mech].

[132] M. A. Despósito and A. Levy Yeyati, "Controlled dephasing of Andreev states in superconducting quantum point contacts," *Phys. Rev. B*, vol. 64, p. 140 511, 14 Sep. 2001.

[133] N. M. Chtchelkatchev and Y. V. Nazarov, "Andreev Quantum Dots for Spin Manipulation," *Phys. Rev. Lett.*, vol. 90, p. 226 806, 22 Jun. 2003.

[134] C. Padurariu and Y. V. Nazarov, "Theoretical proposal for superconducting spin qubits," *Phys. Rev. B*, vol. 81, p. 144 519, 14 Apr. 2010.

[135] S. Rasmussen et al., "Superconducting Circuit Companion—an Introduction with Worked Examples," *PRX Quantum*, vol. 2, p. 040 204, 4 Dec. 2021.

[136] A. Martín-Rodero and A. L. Yeyati, "Josephson and Andreev transport through quantum dots," *Advances in Physics*, vol. 60, no. 6, pp. 899–958, 2011.

[137] A. Zazunov, A. Brunetti, A. L. Yeyati, and R. Egger, "Quasiparticle trapping, Andreev level population dynamics, and charge imbalance in superconducting weak links," *Phys. Rev. B*, vol. 90, p. 104 508, 10 Sep. 2014.

[138] D. G. Olivares, A. L. Yeyati, L. Bretheau, Ç. Ö. Girit, H. Pothier, and C. Urbina, "Dynamics of quasiparticle trapping in andreev levels," *Phys. Rev. B*, vol. 89, p. 104 504, 10 Mar. 2014.

[139] P. D. Kurilovich, V. D. Kurilovich, V. Fatemi, M. H. Devoret, and L. I. Glazman, "Microwave response of an Andreev bound state," *Phys. Rev. B*, vol. 104, p. 174 517, 17 Nov. 2021.

[140] S. Park and A. L. Yeyati, "Andreev spin qubits in multichannel Rashba nanowires," *Phys. Rev. B*, vol. 96, p. 125 416, 12 Sep. 2017.

[141] N. Ackermann, A. Zazunov, S. Park, R. Egger, and A. L. Yeyati, "Dynamical parity selection in superconducting weak links," *Phys. Rev. B*, vol. 107, p. 214 515, 21 Jun. 2023.

[142] K. Zatsarynna, A. Nava, A. Zazunov, and R. Egger, "Many-body quantum dynamics of spin-orbit coupled Andreev states in a Zeeman field," *Phys. Rev. B*, vol. 109, p. 214 505, 21 Jun. 2024.

[143] D. J. van Woerkom et al., "Microwave spectroscopy of spinful Andreev bound states in ballistic semiconductor Josephson junctions," *Nature Physics*, vol. 13, p. 876, 2017.

[144] S. Park et al., "From Adiabatic to Dispersive Readout of Quantum Circuits," *Phys. Rev. Lett.*, vol. 125, p. 077 701, 7 Aug. 2020.

[145] M. Hays et al., "Continuous monitoring of a trapped superconducting spin," *Nature Physics*, vol. 16, p. 1103, 2020.

[146] M. Hays et al., "Coherent manipulation of an Andreev spin qubit," *Science*, vol. 373, no. 6553, pp. 430–433, 2021.

[147] A. Pöschl et al., "Nonlocal conductance spectroscopy of Andreev bound states in gate-defined InAs/Al nanowires," *Phys. Rev. B*, vol. 106, p. L241301, 24 Dec. 2022.

[148] V. Fatemi et al., "Microwave Susceptibility Observation of Interacting Many-Body Andreev States," *Phys. Rev. Lett.*, vol. 129, p. 227 701, 22 Nov. 2022.

[149] F. J. Matute-Cañadas et al., "Signatures of Interactions in the Andreev Spectrum of Nanowire Josephson Junctions," *Phys. Rev. Lett.*, vol. 128, p. 197 702, 19 May 2022.

[150] J. J. Wesdorp et al., "Dynamical Polarization of the Fermion Parity in a Nanowire Josephson Junction," *Phys. Rev. Lett.*, vol. 131, p. 117 001, 11 Sep. 2023.

[151] M. Pita-Vidal et al., "Direct manipulation of a superconducting spin qubit strongly coupled to a transmon qubit," *Nature Physics*, vol. 19, p. 1110, 2023.

[152] J. J. Wesdorp et al., "Microwave spectroscopy of interacting Andreev spins," *Phys. Rev. B*, vol. 109, p. 045 302, 4 Jan. 2024.

[153] L. Y. Cheung et al., "Photon-mediated long range coupling of two Andreev level qubits," *Nature Physics*, 2024.

[154] C. W. J. Beenakker and H. van Houten, "Josephson current through a superconducting quantum point contact shorter than the coherence length," *Phys. Rev. Lett.*, vol. 66, pp. 3056–3059, 23 Jun. 1991.

[155] A. Furusaki and M. Tsukada, "Current-carrying states in Josephson junctions," *Phys. Rev. B*, vol. 43, pp. 10 164–10 169, 13 May 1991.

[156] Y. V. Nazarov and Y. M. Blanter, *Quantum transport: Introduction to Nanoscience*. Cambridge University Press, Cambridge, 2009.

[157] C. Metzger et al., "Circuit-QED with phase-biased Josephson weak links," *Phys. Rev. Res.*, vol. 3, p. 013 036, 1 Jan. 2021.

[158] A. Zazunov, V. S. Shumeiko, E. N. Bratus', J. Lantz, and G. Wendin, "Andreev Level Qubit," *Phys. Rev. Lett.*, vol. 90, p. 087 003, 8 Feb. 2003.

[159] F.-E. von Horstig et al., "Multimodule microwave assembly for fast readout and charge-noise characterization of silicon quantum dots," *Phys. Rev. Appl.*, vol. 21, p. 044 016, 4 Apr. 2024.

[160] H.-P. Breuer, U. Dorner, and F. Petruccione, "Numerical integration methods for stochastic wave function equations," *Computer Physics Communications*, vol. 132, no. 1, pp. 30–43, 2000.

[161] V. Semin, I. Semina, and F. Petruccione, "Stochastic wave-function unravelling of the generalized Lindblad equation," *Phys. Rev. E*, vol. 96, p. 063 313, 6 Dec. 2017.

[162] N. Gisin and I. C. Percival, "The quantum-state diffusion model applied to open systems," *Journal of Physics A: Mathematical and General*, vol. 25, no. 21, p. 5677, Nov. 1992.

[163] S. M. Iacus, *Simulation and Inference for Stochastic Differential Equations: With R Examples (Springer Series in Statistics)*, 1st ed. Springer Publishing Company, Incorporated, 2008.

[164] F. Campaioli, J. H. Cole, and H. Hapuarachchi, "Quantum Master Equations: Tips and Tricks for Quantum Optics, Quantum Computing, and Beyond," *PRX Quantum*, vol. 5, p. 020 202, 2 Jun. 2024.

[165] G. T. Landi, M. J. Kewming, M. T. Mitchison, and P. P. Potts, "Current Fluctuations in Open Quantum Systems: Bridging the Gap Between Quantum Continuous Measurements and Full Counting Statistics," *PRX Quantum*, vol. 5, p. 020 201, 2 Apr. 2024.

[166] J. Audretsch, L. Diósi, and T. Konrad, "Evolution of a qubit under the influence of a succession of weak measurements with unitary feedback," *Physical Review A*, vol. 66, no. 2, Aug. 2002.

[167] H. Uys, H. Bassa, P. du Toit, S. Ghosh, and T. Konrad, "Quantum control through measurement feedback," *Phys. Rev. A*, vol. 97, p. 060 102, 6 Jun. 2018.

[168] J. K. Stockton, R. van Handel, and H. Mabuchi, "Deterministic dicke-state preparation with continuous measurement and control," *Physical Review A*, vol. 70, no. 2, Aug. 2004.

[169] S. Lieu, R. Belyansky, J. T. Young, R. Lundgren, V. V. Albert, and A. V. Gorshkov, "Symmetry Breaking and Error Correction in Open Quantum Systems," *Phys. Rev. Lett.*, vol. 125, p. 240 405, 24 Dec. 2020.

[170] O. Shtanko, Y.-J. Liu, S. Lieu, A. V. Gorshkov, and V. V. Albert, *Bounds on Autonomous Quantum Error Correction*, 2023. arXiv: 2308.16233 [quant-ph].

[171] L. B. Kristensen, M. Kjaergaard, C. K. Andersen, and N. T. Zinner, "Hybrid quantum error correction in qubit architectures," *Phys. Rev. A*, vol. 108, p. 022 403, 2 Aug. 2023.

[172] L. Pezzè, A. Smerzi, M. K. Oberthaler, R. Schmied, and P. Treutlein, "Quantum metrology with nonclassical states of atomic ensembles," *Rev. Mod. Phys.*, vol. 90, p. 035 005, 3 Sep. 2018.

[173] P. Hyllus et al., "Fisher information and multiparticle entanglement," *Phys. Rev. A*, vol. 85, p. 022 321, 2 Feb. 2012.

[174] G. Tóth, "Multipartite entanglement and high-precision metrology," *Phys. Rev. A*, vol. 85, p. 022 322, 2 Feb. 2012.

[175] C. W. Helstrom, "Quantum detection and estimation theory," *Journal of Statistical Physics*, p. 231, 1969.

[176] R. Sahay and R. Verresen, "Classifying One-Dimensional Quantum States Prepared by a Single Round of Measurements," *PRX Quantum*, vol. 6, p. 010 329, 1 Feb. 2025.

[177] R. Sahay and R. Verresen, *Finite-Depth Preparation of Tensor Network States from Measurement*, 2024. arXiv: 2404.17087 [quant-ph].

[178] O. Hosten and P. Kwiat, "Observation of the Spin Hall Effect of Light via Weak Measurements," *Science*, vol. 319, no. 5864, pp. 787–790, 2008.

[179] P. B. Dixon, D. J. Starling, A. N. Jordan, and J. C. Howell, "Ultrasensitive Beam Deflection Measurement via Interferometric Weak Value Amplification," *Phys. Rev. Lett.*, vol. 102, p. 173 601, 17 Apr. 2009.

[180] A. Palacios-Laloy et al., " Experimental violation of a Bell's inequality in time with weak measurement," *Nature Physics*, vol. 6, p. 442, 2010.

[181] J. P. Groen et al., "Partial-Measurement Backaction and Nonclassical Weak Values in a Superconducting Circuit," *Phys. Rev. Lett.*, vol. 111, p. 090 506, 9 Aug. 2013.

[182] K. S. Cujia, J. M. Boss, K. Herb, J. Zopes, and C. L. Degen, "Tracking the precession of single nuclear spins by weak measurements," *Nature*, vol. 571, p. 230, 2019.

[183] Y. Kim et al., "Observing the quantum Cheshire cat effect with noninvasive weak measurement," *npj Quantum Information*, vol. 7, p. 13, 2021.

[184] M. Pita-Vidal, J. J. Wesdorp, and C. K. Andersen, "Blueprint for All-to-All-Connected Superconducting Spin Qubits," *PRX Quantum*, vol. 6, p. 010 308, 1 Jan. 2025.

[185] D. Volya and P. Mishra, "Quantum steering of surface error correcting codes," in *2023 IEEE International Conference on Quantum Computing and Engineering (QCE)*, vol. 01, 2023, p. 1394.

[186] M. G. Paris, "Quantum estimation for quantum technology", *International Journal of Quantum Information*, vol. 7, no. supp01, pp. 125–137, 2009.

[187] L. Pezzé and A. Smerzi, "Entanglement, nonlinear dynamics, and the heisenberg limit," *Phys. Rev. Lett.*, vol. 102, p. 100 401, 10 Mar. 2009.

[188] G. Tóth and I. Apellaniz, "Quantum metrology from a quantum information science perspective," *Journal of Physics A: Mathematical and Theoretical*, vol. 47, no. 42, p. 424 006, Oct. 2014.

[189] J. Liu, H. Yuan, X.-M. Lu, and X. Wang, "Quantum Fisher information matrix and multiparameter estimation," *Journal of Physics A: Mathematical and Theoretical*, vol. 53, no. 2, p. 023 001, Dec. 2019.

[190] M. Buchhold, Y. Minoguchi, A. Altland, and S. Diehl, "Effective Theory for the Measurement-Induced Phase Transition of Dirac Fermions," *Phys. Rev. X*, vol. 11, p. 041 004, 4 Oct. 2021.

[191] J. F. Poyatos, J. I. Cirac, and P. Zoller, "Quantum Reservoir Engineering with Laser Cooled Trapped Ions," *Phys. Rev. Lett.*, vol. 77, pp. 4728–4731, 23 Dec. 1996.

[192] S. Diehl, A. Micheli, A. Kantian, B. Kraus, H. P. Büchler, and P. Zoller, "Quantum states and phases in driven open quantum systems with cold atoms," *Nat. Phys.*, vol. 4, no. 11, pp. 878–883, Nov. 2008.

[193] F. Verstraete, M. Wolf, and J. Ignacio Cirac, "Quantum computation and quantum-state engineering driven by dissipation," *Nature Physics*, vol. 5, no. 11, pp. 633–636, Jun. 2009.

[194] J. T. Barreiro et al., "An open-system quantum simulator with trapped ions," *Nature*, vol. 470, no. 7335, pp. 486–491, Feb. 2011.

[195] H. Krauter et al., "Entanglement generated by dissipation and steady state entanglement of two macroscopic objects," *Phys. Rev. Lett.*, vol. 107, p. 080 503, 8 Aug. 2011.

[196] J. P. Paz and W. H. Zurek, "Continuous error correction," *Proceedings of the Royal Society of London. Series A: Mathematical, Physical and Engineering Sciences*, vol. 454, no. 1969, pp. 355–364, 1998.

[197] J. P. Barnes and W. S. Warren, "Automatic Quantum Error Correction," *Phys. Rev. Lett.*, vol. 85, pp. 856–859, 4 Jul. 2000.

[198] C. Ahn, A. C. Doherty, and A. J. Landahl, "Continuous quantum error correction via quantum feedback control," *Phys. Rev. A*, vol. 65, p. 042 301, 4 Mar. 2002.

[199] C. Ahn, H. M. Wiseman, and G. J. Milburn, "Quantum error correction for continuously detected errors," *Phys. Rev. A*, vol. 67, p. 052 310, 5 May 2003.

[200] M. Sarovar, C. Ahn, K. Jacobs, and G. J. Milburn, "Practical scheme for error control using feedback," *Phys. Rev. A*, vol. 69, p. 052 324, 5 May 2004.

[201] O. Oreshkov and T. A. Brun, "Continuous quantum error correction for non-markovian decoherence," *Phys. Rev. A*, vol. 76, p. 022 318, 2 Aug. 2007.

[202] J. Kerckhoff, H. I. Nurdin, D. S. Pavlichin, and H. Mabuchi, "Designing Quantum Memories with Embedded Control: Photonic Circuits for Autonomous Quantum Error Correction," *Phys. Rev. Lett.*, vol. 105, p. 040 502, 4 Jul. 2010.

[203] E. Kapit, "Hardware-Efficient and Fully Autonomous Quantum Error Correction in Superconducting Circuits," *Phys. Rev. Lett.*, vol. 116, p. 150 501, 15 Apr. 2016.

[204] E. Kapit, "Error-Transparent Quantum Gates for Small Logical Qubit Architectures," *Phys. Rev. Lett.*, vol. 120, p. 050 503, 5 Feb. 2018.

[205] S. Lieu, Y.-J. Liu, and A. V. Gorshkov, "Candidate for a Passively Protected Quantum Memory in Two Dimensions," *Phys. Rev. Lett.*, vol. 133, p. 030 601, 3 Jul. 2024.

[206] Z. Leghtas et al., "Stabilizing a Bell state of two superconducting qubits by dissipation engineering," *Phys. Rev. A*, vol. 88, p. 023 849, 2 Aug. 2013.

[207] P. Campagne-Ibarcq et al., "Quantum error correction of a qubit encoded in grid states of an oscillator," *Nature*, vol. 584, p. 368, 2020.

[208] J. M. Gertler, B. Baker, J. Li, S. Shirol, J. Koch, and C. Wang, "Protecting a bosonic qubit with autonomous quantum error correction," *Nature*, vol. 590, p. 243, 2021.

[209] W. P. Livingston, M. S. Blok, E. Flurin, J. Dressel, A. N. Jordan, and I. Siddiqi, "Experimental demonstration of continuous quantum error correction," *Nature Communications*, vol. 13, p. 2307, 2022.

[210] D. Lachance-Quirion et al., "Autonomous Quantum Error Correction of Gottesman-Kitaev-Preskill States," *Phys. Rev. Lett.*, vol. 132, p. 150 607, 15 Apr. 2024.

[211] A. Ahmadi and E. Greplova, "Quantifying non-stabilizerness via information scrambling," *SciPost Phys.*, vol. 16, p. 043, 2024.

[212] P. S. Tarabunga, M. Frau, T. Haug, E. Tirrito, and L. Piroli, *A nonstabilizerness monotone from stabilizerness asymmetry*, 2024. arXiv: 2411.05766 [quant-ph].

[213] E. Davis, G. Bentsen, and M. Schleier-Smith, "Approaching the Heisenberg Limit without Single-Particle Detection," *Phys. Rev. Lett.*, vol. 116, p. 053 601, 5 Feb. 2016.

[214] T. Macrì, A. Smerzi, and L. Pezzè, "Loschmidt echo for quantum metrology," *Phys. Rev. A*, vol. 94, p. 010 102, 1 Jul. 2016.

[215] S. Dooley, S. Pappalardi, and J. Goold, "Entanglement enhanced metrology with quantum many-body scars," *Phys. Rev. B*, vol. 107, p. 035 123, 3 Jan. 2023.

[216] D. A. Puente and M. Rizzi, *Learning feedback mechanisms for measurement-based variational quantum state preparation*, 2025. arXiv: 2411.19914 [quant-ph].

[217] A. Barchielli and V. P. Belavkin, "Measurements continuous in time and a posteriori states in quantum mechanics," *Journal of Physics A: Mathematical and General*, vol. 24, no. 7, pp. 1495–1514, Apr. 1991.

Acknowledgements

Firstly, I would like to thank my supervisor, Prof. Dr. Reinhold Egger, for guiding me through my academic career ever since my Bachelor's thesis in 2018 and giving me the opportunity to do my PhD and to develop my academic career, especially for the quick and hands-on supervision during all projects. I also want to thank him for giving me the possibility to connect with the scientific community at various international conferences and especially for the extended stay at the Weizmann Institute in Israel.

I would also like to thank PD Dr. Hermann Kampermann for taking up the role as second advisor and corrector of this thesis. Also, for all the useful insights on quantum information and quantum error correction in the lectures throughout the years.

I would like to thank all my collaborators, in particular Prof. Dr. Yuval Gefen, for allowing me to visit the Weizmann Institute of Science for an extended period of time and all the research ideas and interesting questions during our many discussions, always reminding me to see the big picture of the topic at hand. I would also like to thank Prof. Dr. Igor Gornyi, Prof. Dr. Alfredo Levy Yeyati, Prof. Dr. Sebastian Diehl and Jun.-Prof. Dr. Silvia Pappalardi for all the useful discussions during our research projects and the work in completing the publications.

Additionally, I would like to thank all past and present members of TP4 for providing a nice and fruitful work environment. I had a great time being a part of this group, and I hope that we can keep in touch as best as possible. In particular, I want to thank our secretary, Claudia Stader, for always helping with any problem at hand, especially with travel organizations and when dealing with the university administration. I would also like to thank Dr. Alex Zazunov for the research collaboration and for always asking many insightful questions.

Also, I want to thank the members of the excellence cluster *ML4Q* and the *Collaborative Research Center 183* for organizing all types of conferences and retreats and allowing me to take part in the organization of events myself. It has been a pleasure to work alongside so many talented people and to get to know such a great network.

A special thanks goes out to Edward Medina Guerra and Dr. Nico Ackermann for all the discussions on scientific and non-scientific matters, helping me to cope with the ups and downs of research. It was always great to not be alone on this part of the academic journey, keeping up the motivation, especially when progress was slower than expected. To Nico, also for all the work on our publication. Also, thanks to Dr. Parveen Kumar for the guidance, especially when staying at the Weizmann Institute, and for the encouragement to pursue different research directions.

Another particular thanks goes out to Dr. Tim Bauer and Alexander Gresch for all these years of friendship at university and for the help with correcting this thesis. Even though we won't be working on the same floor anymore, I hope that we can keep in touch as much as possible.

I would also like to thank my family and friend(o)s which are not named here personally

for all the support and encouragement throughout the years. Without you, I would not have had the energy and courage to complete this work, and also the incredible support of all science communication events has been greatly appreciated.

Lastly, I would like to thank my girlfriend, Luise Schuba, for always being there for me and supporting me throughout any part of my academic endeavors. Thank you for motivating me when necessary, but also for taking my mind off physics in order not to get lost in this work. I love you.

Selbstständigkeitserklärung

Ich versichere an Eides Statt, dass die Dissertation von mir selbständig und ohne unzulässige fremde Hilfe unter Beachtung der „Grundsätze zur Sicherung guter wissenschaftlicher Praxis an der Heinrich-Heine-Universität Düsseldorf“ erstellt worden ist.
Weiterhin erkläre ich, dass ich die Dissertation keiner anderen Fakultät bereits vorgelegt habe und keinerlei vorherige erfolglose oder erfolgreiche Promotionsversuche vorliegen. Darüber hinaus ist mir bekannt, dass jedweder Betrugsversuch zum Nichtbestehen oder zur Aberkennung der Prüfungsleistung führen kann.

Düsseldorf, 10. April 2025 Samuel Morales